Spectroscopy Schemes for Improved Optical Clock Stability

Filip Butuc-Mayer

Submitted in partial fulfillment of the requirement for
the degree of
Doctor of Philosophy
in
Atomic and Laser Physics

University of Oxford
St. Peter's College

March 2026

To my best friend

and the most wonderful way the cosmos ever spoke to me.

Acknowledgements

The work presented in this thesis is the result of close collaboration within my research team and the wider research group. First and foremost, this work would not have been possible without the resources and facilities at the National Physical Laboratory, which I was fortunate enough to access throughout my studies. I am deeply grateful to my colleagues for the work that they put in the experiments conducted in our lab. In particular, I thank Chen-Hao Feng for sharing the long hours in the lab with me to bring Sr2 back to life, and for her patience in tackling challenging technical tasks. I also thank Matthew Johnson for generously sharing his knowledge of the lab with me at lightning speed, which was invaluable during my early days. I owe special thanks to our team supervisor, Ian Hill, for his unwavering encouragement and guidance, his insistence on systematic problem-solving, and for helpful comments on this manuscript. The many discussions that we had on conceptual problems were instrumental in shaping the theoretical developments presented in this thesis. The broader Optical Frequency Group at the National Physical Laboratory, which hosts the strontium lattice clocks, supplied critical infrastructure for our experiments. I am grateful to the ultrastable cavities team, Marco Schioppo and Adam Parke, for servicing our lab with excellent frequency stability, to the optical frequency combs team, Jacob Tunesi and Xi Zhang, for their cooperation and, together with the fibre links team—Jaques-Olivier Gaudron, Wei Huan, and Namneet Kaur—for enabling measurements with other laboratories. I would also like to acknowledge other members of the group whose discussions and advice have supported me and the team: Ben Allen, Thomas Easton, Maxime Favier, Max Tamussino, Alexandra Tofful, and Adam Parsons. I thank my DPhil supervisor, Professor Christopher Foot, for welcoming me into the programme and assisting with departmental matters. My research was funded by the EPSRC with contributions from the National Physical Laboratory, and I am sincerely thankful for their support.

I am forever grateful to my wife, Patricia, whose unending love and support has carried me through these four years. Her impact on the completion of this work through burdening of many familial duties and responsibilities as well as through her excellent strategic advice and words of encouragement cannot be overstated.

Table of Contents

List of Tables

List of Figures

List of Abbreviations

ADEV	Allan Deviation.
AOM	Acousto-Optic Modulator.
AVAR	Allan Variance.
BBR	Blackbody radiation.
BIPM	Bureau of Weights and Measures.
CGPM	General Conference on Weights and Measures.
CTL	Coherence Time Limit.
DD	Dynamical Decoupling.
DE	Dick Effect.
ECDL	Extended Cavity Diode Laser.
EOM	Electro-Optic Modulator.
GNSS	Global Navigation Satellite System.
INRIM	Instituto Nazionale di ricerca metrologica.
LO	Local Oscillator.
LZS	Linear Zeeman Shift.
MOT	Magneto-Optical Trap.
NMIJ	National Metrology Institute of Japan.
NPL	National Physical Laboratory.
OADEV	Overlapping Allan Deviation.
PBS	Polarising Beam Splitter.
PDH	Pound-Drever-Hall.
PLL	Phase-Locked Loop.
PLS	Path Length Stabilisation.
PSD	Power Spectral Density.
PTB	Physikalisch-Technische Bundesanstalt.
QPN	Quantum Projection Noise.
RF	Radio Frequency.
SB	Slowing Beam.
SHG	Second Harmonic Generation.
SI	Système international d'unitès.
SQL	Standard Quantum Limit.
SYRTE	Sytèmes de Référence Temps Espace.
TA	Tapered Amplifier.
TAI	Temps atomique international.

ULE	Ultra-low expansion.
VCO	Voltage-Controlled Oscillator.
ZDT	Zero Dead Time.

Abstract

Frequency metrology underpins precise measurements. At the forefront of this field are optical clocks which can perform measurements that are accurate to more digits than those in the number representing seconds elapsed from the beginning of the universe. Frequency estimation errors in the operation of optical clocks lead to frequency instability, prohibiting them from reaching high accuracies on short to medium time scales, and limiting access to interesting measurements of the atomic environment and exotic external perturbations such as gravity fields or fields of fundamentally new physical origins. Optical lattice traps are typically employed in state-of-the-art optical clocks to suppress Doppler effects. By carefully tuning the optical lattice to the magic wavelength, unwanted Stark shifts can be suppressed significantly, allowing operation with thousands of atoms and minimising the fundamental source of frequency estimation errors, namely the quantum projection noise, to around 3×10^{-17} at 1 s.

In this thesis, the status of the two Strontium optical lattice clocks at NPL, Sr1 and Sr2, is presented going over a few interesting measurement campaigns from the past years involving Sr1 and the latest experimental efforts to re-enable operation of Sr2. A model of clock stability is developed by incorporating known and new frameworks to characterise the relation between the operating parameters of optical clocks and their performance, with relevance to the NPL lattice clocks and beyond. In particular, a method is identified for addressing the main technical noise for optical lattice clocks, the Dick effect, which typically has a magnitude of 10^{-16} at 1 s and prevents optical lattice clocks from reaching the quantum projection noise level. By taking advantage of dynamical decoupling we can engineer an optimised duty cycle with benefits in general for systems limited by the optical coherence of the clock laser. Moreover, a study of other noise sources in the NPL lattice clocks is conducted using synchronous measurements between Sr1 and Sr2, revealing a large contribution from linear Zeeman shifts, also at the 10^{-16} level, and a plan to tackle them is detailed. A hybrid clock architecture is discussed showing how optical lattice clocks can improve the optical coherence of ion clocks thanks to their higher servo rate, and a preliminary experimental demonstration is reported.

Finally, a new type of spectroscopy is presented which completely avoids aliasing of linear Zeeman shifts by simultaneously driving transitions with opposite Zeeman sensitivities. Such a technique also enables the continuous interrogation of atoms, a crucial missing component in the Dick-free conveyor belt lattice clock concept heralded as the next standard of stable optical clocks.

Chapter 1

Introduction to optical lattice clocks

1.1 Time measurements and the SI second

Clocks are unassuming devices. They sit on walls, on wrists or in smartphones and quietly keep time, constantly ticking second by second. However, even without going into the intricate technical details of how they work, there is more going on at a conceptual level than first meets the eye. The core of a clock is an oscillator. It performs periodic oscillations at a steady frequency, allowing the keeping of time through counting the number of oscillations elapsed during a measurement. So, a clock needs both an oscillator to perform the oscillations and a counter to count them. The performance of the clock rests to a large degree on how stable the oscillation frequency is, since it means that the oscillation lasts the same period each time, so it can be used as a unit of time. But no oscillator is perfectly stable and, if left unchecked, there will always be changes in its frequency creeping up even if only at the attosecond level. So, a third key component for a clock is a stable frequency reference against which the oscillator is compared to determine if its frequency evolves from the nominal value. The frequency reference can be simply a more stable clock, but often it is a system which has a sharp response at a resonance frequency.

The stability of a clock is important for making reliable time interval measurements, but if we want the clock to be reproducible or comparable to other clocks it also needs to be accurate. An accurate clock has a fourth component, namely a definition for the time unit which can be realised to ensure that measurements made with one clock are equivalent to measurements made with another clock following the same definition.

For a large part of our recent history, the unit of time was defined through the second as the fraction 1/86,400 of a day. The rotation of the Earth about its axis provided the reference against which mechanical oscillators, such as swinging pendulums, could be calibrated with the help of astronomers detecting when the planet completed a full rotation with respect to stars in outer space. As oscillators improved, it was apparent that variations in the rotation period of the Earth made it an unsuitable standard.

In 1960, the "ephemeris second" provided a new definition for the time unit through its international adoption initiated by the General Conference on Weights and Measures

(CGPM), as part of the *Système international d'unités* (SI). It was a definition based on the Newtonian prediction for the motion of the planets and the Moon. The position of the planets at any given moment indicated the elapsed time from a reference point, which was selected as the start of the year 1900. The second was then derived as the fraction 1/31,556,925.9747 of the tropical year (the time between two vernal equinoxes) of 1900, as calculated from the models of the planetary motions.

This definition only had a brief lifetime, however, before the atomic definition was adopted in 1967 due to the success of the atomic clocks demonstrating superior stability and at the same time ease of realisation. In the atomic clock, the frequency reference is a microwave transition between specific hyperfine energy levels of the Caesium-133 atom. Since all atoms of a given species and isotope are identical [1], they are a universal standard. The atomic transition provides a narrow resonance, which is excited by the oscillator in the form of electromagnetic radiation of microwave frequency. The oscillator has a frequency near the atomic resonance, and it can be steered towards that resonance by a servo mechanism based on the response of the atoms to that radiation.

Currently, the international timescale, the well-known Universal Coordinated Time (UTC), follows the international atomic time (TAI) with a static offset of exactly 37 seconds. The offset bridges between the precise atomic time and the long-term variations of the earth-bound UTC, and was gradually built up by adding so-called "leap seconds" to maintain a regular 24 hour day similarly to how leap days are added to maintain 12 calendar months per one revolution around the Sun. TAI is based on a large ensemble of atomic clocks around the world whose timestamps are broadcast via satellite to the Bureau of Weights and Measures (BIPM). After adjusting for the gravitational effects based on the location of each clock, a weighted average of all the clocks is computed with higher weighting given to the better performing clocks.

Caesium fountain clocks, which serve as the primary frequency standards, have reached fractional frequency uncertainties on the order of 10^{-16} [1, 2]. Their excellent accuracy has proved useful beyond timekeeping, with applications in network synchronisation [3], underpinning satellite-based global navigation systems [4], and more recently providing a spectroscopic reference for antihydrogen experiments [5]. Further improvements are limited by systematic effects inherent to the microwave architecture, including blackbody radiation shifts, atomic collisions, magnetic field sensitivities, and particularly distributed cavity phase shifts, which arise from spatial inhomogeneities in the microwave field and are difficult to suppress below current levels. These effects define a practical accuracy ceiling for caesium clocks that has proven resistant to further development.

Over the last couple of decades, improvements to clock performance were achieved through optical clocks instead. With the invention of the optical frequency comb [6, 7], it was possible to take advantage of high frequency optical transitions interrogated with narrow linewidth lasers [8]. As optical signals cannot be counted electronically, optical frequency combs can be used to generate optically derived microwave signals which maintain the fractional stability of the original signals. The first optical clocks used single ions which can be trapped very efficiently to avoid Doppler shifts from the ion's motion. Neutral

[1] Unless perturbed by external fields.

atoms required a different approach, making use of the dipole force to confine the atoms in an optical lattice. The proposal of the magic wavelength [9] provided the missing piece needed to use them as a frequency reference by tuning the wavelength of the lattice such that the unavoidable Stark shifts of the ground and excited states are equal and therefore the transition frequency is the same as that of a free atom. A key characteristic of a good frequency standard is that it has a narrow linewidth. Alkaline-earth atoms have the narrow intercombination line corresponding to the $^1S_0 \rightarrow {}^3P_0$ transition which is doubly forbidden by spin and total angular momentum selection rules. Among alkaline-earth species, Strontium and Ytterbium are the best candidates thanks to having easily achievable cooling, trapping, and spectroscopy wavelengths, and large atomic masses which reduces the recoil motion from laser cooling resulting in lower temperatures.

Optical clocks now significantly outperform traditional atomic clocks with best reported uncertainties reaching below the 10^{-18} level in both ion clocks based on Aluminium or Ytterbium atoms [10–12] and lattice clocks using Strontium atoms [13], with lattice clocks using Ytterbium atoms also performing well at the low 10^{-18} level [14]. Furthermore, several compact and transportable optical clock systems have been built and characterised to uncertainties at the low 10^{-18} level [15–17] preparing the way for geodesy and space-based applications and facilitating clock comparisons. In direct comparisons between clocks, the uncertainties are larger because both clocks contribute and there are also statistical effects due to clock instability or link noise. However, uncertainties at the 10^{-17} level and below have been demonstrated [18–20] with best results from local measurements or comparisons over optical fibre links. Despite these advancements, the uncertainty of any absolute frequency measurement remains limited by the accuracy with which the caesium frequency can be realised, since every absolute measurement has to be traced back to it. This practical limitation of the current SI second definition has prompted the case for a new definition based on an optical transition.

For a new definition in terms of more precise references to be adopted, it is necessary to ensure reproducible measurements with significantly higher accuracy. Reasonable criteria have been proposed [21] for the characterisation of environmental perturbations that can shift the clock transition, for demonstrated uncertainties through comparisons of different clocks, and for the robustness of the operation of the clocks. The first point refers to systematic evaluations of clock frequency shifts summarised in uncertainty budgets and is requiring values $< 2 \times 10^{-18}$. The second point refers to measurements of the offsets between different clocks performed in remote comparison campaigns through optical fibre or satellite links between laboratories and requires values $< 5 \times 10^{-18}$. The last one refers to operation with high uptime leading to regular contributions to TAI with uncertainties at the limit set by the primary standards, which is at $< 3 \times 10^{-16}$. Additionally, there are requirements on the optical network on which the remote comparisons are made as well as requirements on the knowledge of the geopotential at the locations of the clocks.

For now, as an intermediate step towards the redefinition in terms of an optical frequency, several optical transitions have been adopted as secondary representations of the second. By making measurements of optical clocks against primary Caesium standards, their absolute frequencies have been determined, such that they can be used to contribute to steering of TAI. Furthermore, such optical frequency standards can be used to generate

a timescale as was demonstrated in [22] with SI accuracy.

Any definition in terms of atomic transitions is conceptually based on the premise that the transition frequencies are unchanging across time and space. However, when considering other applications, one can make use of possible variations in the transition frequencies as tests of exotic effects, guiding the development of new fundamental Physics theories [23]. This will be the topic of the next section.

1.2 Fundamental Physics and geodesy

Useful measurements beyond timekeeping can be derived from the unprecedented accuracy of atomic clocks. The high sensitivity of clock transition frequencies to changes in the environment to which atoms are subjected makes them sensors to external electric, magnetic and even gravitational fields. Furthermore, they can be used as probes in fundamental tests such as variations in the value of the fine structure constant and dark matter effects. Possible variations in the fine structure constant are part of ultralight dark matter models where scalar fields can affect the value of the fine structure constant by coupling to the electromagnetic field [24].

The fine structure constant, which determines the strength of the electromagnetic field, the dominant interaction between the nucleus and electrons, affects the electron energy levels directly through the Coulomb potential as well as indirectly through relativistic corrections due to the modified electron orbit velocities. Any variations in the electromagnetic coupling strength would affect the frequency of the transition between those energy levels, so a very precise measurement of an optical clock's frequency can simultaneously be a measurement of changes in the fine structure constant [24], if all other effects are prevented or accounted for. Measuring the frequency of an atomic clock requires a similarly good reference, which could be another atomic clock. If the other clock is of the same species, though, the effect would not be observable as the reference would change by the same amount. So, for this to work, it is necessary to use atomic clocks based on transitions that have different sensitivities to the fine structure constant. The resulting change in frequency for a given change in α is a simple relation which holds if the fractional change is small.

$$\frac{\delta\omega}{\omega_0} = K_\alpha \frac{\delta\alpha}{\alpha} \tag{1.1}$$

Here, K_α is known as the enhancement factor and it is different for different atomic transitions, as shown in Table 1.1. Of particular utility for this type of measurement are highly charged ions, which, although pose additional practical and theoretical challenges, can have significantly larger enhancement factors [25].

A recent publication used data from optical clocks at NPL to infer the stability of the fine structure constant, α [27]. The analysis was based on the comparison between the Sr optical lattice clock, Sr1, and the Yb^+ ion clock. The absence of significant variations in the frequency ratio rules out α variations at the corresponding level including the enhancement factor. An upper limit of the magnitude of the variations was thus inferred at $2.3 \times$

Atomic transition	$\boldsymbol{K_\alpha}$
Yb^+ ($^2S_{1/2} \rightarrow {}^2F_{7/2}$, E3)	-6
Cs ($6s\,^2S_{1/2}$ hyperfine)	~ 2
Sr^+ ($^2S_{1/2} \rightarrow {}^2D_{5/2}$)	0.4
Yb ($^1S_0 \rightarrow {}^3P_0$)	0.3
Sr ($^1S_0 \rightarrow {}^3P_0$)	0.06
Al^+ ($^1S_0 \rightarrow {}^3P_0$)	0.008

Table 1.1: **Enhancement factors K_α of selected atomic transitions for variations of the fine-structure constant α.** Values from [26].

$10^{-16}/\sqrt{\tau/s}$, valid for timescales on the order of a minute to a few hours. In this expression, τ represents the time factor used for averaging the frequency to reduce white noise from each clock, and it can be seen that the limit improves for longer averaging times. In other words, the measurement is more sensitive to slower oscillations because the random fluctuations in each clock average out. This highlights the importance of clock frequency stability, since if we want to be able to detect phenomena that affect α on short timescales we cannot afford to take long measurements as those would wash out the effect.

As a last example of the use of high performing optical clocks, we consider their gravitational detection potential based on gravitational redshift. Clock comparisons between clocks at different gravitational potentials are sensitive to this effect and have been used to demonstrate uncertainties at the centimetre level [15, 28–30] corresponding to fractional frequency uncertainties at the 10^{-18} level. Such measurements could prove useful for measuring the geoid and detecting time variations marking seismic activity. Other interesting time-sensitive measurements are gravitational wave detection with satellite-based clocks [31] and topological dark mater detection [32].

1.3 State of the art for optical clocks

Optical lattice clocks possess a fundamental advantage over ion clocks: their large atom numbers yield a significantly lower standard quantum limit. However, technical limitations in the local oscillator and duty cycle prevent them from reaching this quantum-limited stability. This thesis addresses these barriers to unlock the lattice clock's full potential. Moreover, stabilizing the local oscillator against the lattice clock creates a pathway to enhance ion clock stability as well, leveraging the lattice's advantages to benefit both technologies.

Frequency instability constitutes one of two classes of uncertainty in the clock frequency, namely statistical uncertainty, which, as mentioned before, is due to white frequency noise in the clock laser, and is a measure of the extent to which the frequency fluctuates about its mean. The second class is systematic uncertainty, and it represents our limited knowledge of the environment of the atoms shifting their energy levels and therefore of the extent to which the transition frequency is different from its unperturbed value. In this section, the

main sources of systematic uncertainty are discussed briefly before moving on to the topic of frequency instability.

The leading source of systematic uncertainty in optical lattice clocks is the blackbody radiation (BBR) from the vacuum chamber. Radiation from the chamber walls leads to Stark shifts in the energy levels which, due to differential polarisability between the ground and excited states, causes a frequency shift in the clock transition. Because the dominant contributions to the differential polarisability come from transitions at optical frequencies, well above the peak of the room-temperature BBR spectrum, the frequency shift to the clock transition is typically approximated as a static DC Stark shift with smaller dynamic corrections accounting for the BBR profile of the emissions. The static component for Strontium at room temperature is at the 10^{-15} level, so it needs to be measured accurately and corrected.

Good knowledge of the static BBR shift component can be obtained by accurately measuring the temperature of the chamber with in-situ sensors. The frequency-dependent dynamic corrections of the BBR shift pose more challenges, being sensitive to the different emissivities of the chamber and view ports respectively when there are temperature inhomogeneities throughout the chamber, and requiring extensive knowledge of the polarisabilities for the two clock states. Careful control of the thermal distribution has been shown to reduce the uncertainty to a few parts in 10^{18} [33] as did temperature characterisation with an array of external sensors paired with a complex model of the science chamber [34]. More recently [13], a BBR uncertainty below 10^{-18} was attained by improving the uncertainty in the dynamical BBR coefficient further through a measurement of the $^3D_1$ state lifetime.

After BBR, the other dominant source of uncertainty is the AC Stark shift caused by the optical lattice trap. The shift can be minimised by using low intensities for the trapping light, provided that tunnelling effects are suppressed by removing the degeneracy between lattice sites through gravitational potential gradients [35]. The electric dipole polarisability can be reduced to the 10^{-19} level by careful consideration of the scalar, vector and tensor components [36]. Higher order polarisability effects have also been shown to be significant at this level [37] though reduction is possible with operational magic wavelengths [38]. Typically, lattice shifts are estimated by alternating between low and high lattice intensity values and comparing the frequency corrections generated from the two configurations. This type of measurement will be subject to other measurement noise sources which set the stability of the clock, highlighting again the importance of clock stability helping, in this case, to obtain a measurement of the lattice shift with higher stability in a shorter time.

The fundamental limit to the stability of optical clocks is quantum projection noise (QPN) [39], stemming from the randomness of the wavefunction collapse when an atomic excitation fraction is measured to estimate the excitation amplitude. Its scaling of $1/\sqrt{N}$ for a number N of atoms means that the effect is significantly larger for single ion clocks, compared to optical lattice clocks with their ability to probe thousands of atoms simultaneously. Density shifts from atomic collisions restrict the usefulness of having more atoms in the trap, though larger ensembles can be accommodated by using 3-dimensional

lattice configurations [40] or by loading the atoms in the trap with a more uniform distribution [41]. Moreover, entanglement of the atoms can be used to implement useful spin-squeezing increasing the atom number dependent suppression factor [42]. However, it has been suggested [43] that this effect can only provide an advantage for clocks based on small ensembles of atoms, as beyond that limitations imposed by the local oscillator start to dominate. In addition to increasing the number of atoms, the contribution of QPN on frequency instability can also be controlled by increasing the spectroscopy time. Longer times lead to narrower spectroscopic lines which reduces the impact of the errors on the frequency corrections. However, the finite coherence of the atom-light interaction imposes a limit on the interaction time.

Although atomic coherence is on the order of minutes [44], the best optical coherence times that can be achieved with the help of ultrastable optical cavities are on the order of seconds, with measurements limited to even shorter times since errors starts to grow as atomic interrogation times approach the laser coherence time. The optical phase coherence is intrinsically linked to frequency noise. Thermal noise in the spacers and mirror coatings of optical cavities sets a flicker noise floor for their frequency stability [45, 46]. Silicon cavities operated at cryogenic temperatures have shown leading stability [8, 47, 48] benefiting from crystalline coatings on the mirrors [49], while similar performance has also been demonstrated by long ULE glass cavities with flicker limits below 10^{-16} provided adequate measures are used to minimise thermal noise and vibrational effects [50] as well as residual amplitude modulation effects [51].

The potential stability of optical lattice clocks attributed to their high number of atoms is currently not realised due to technical limitations in the form of the Dick effect [39]. Errors in the frequency offset estimation of the laser in the atom servo arise due to uneven sensitivity, especially from the preparation and detection stages, referred to as dead time, when atoms cannot be used as a reference for the laser. Good optical coherence not only improves the stability by directly reducing laser noise, but also allows longer atomic measurements of the laser noise thus leading to more effective compensation through the atomic servo. The Dick effect therefore sets the stability of lattice clocks typically at the low 10^{-16} level [33, 52, 53], with state-of-the-art silicon cavities helping to push that down to the mid-to-high 10^{-17} level [54]. Although this is significantly better than the QPN-limited ion clocks, which are typically at the low 10^{-15} level [55, 56], it is still far from their potential QPN level of low 10^{-17} [57, 58].

Significant advantages can be gained by combining optical clocks in so-called composite schemes. Zero dead time systems have been demonstrated to improve the stability of optical lattice clocks through interleaved measurements in two atomic ensembles [59]. Moreover, faster loading of atoms into the lattice by "draining" from the broadband MOT [60] can help reduce the dead time, while non-demolition detection can be used to extend the duty cycle by keeping atoms in the trap for multiple interrogations [61]. Other composite setups include sharing phase information from one clock with another clock to extend the coherence time of the laser. One such scheme is the differential spectroscopy method [62], where two clocks are probed synchronously by the same local oscillator (with the frequency difference bridged by a frequency comb) and the phase estimated by the first clock is applied as a correction on the second clock. The resulting measurement of the

second clock thus represents the differential phase between the two clocks. Non-demolition measurements repeated in fast succession can be used to implement atom phase locks where the local oscillator phase noise is either corrected or tracked in the measurements of the other clock [63, 64]. Similarly, instead of short repeated measurements, extended measurements making use of dynamical decoupling can be employed [65].

It is also possible to improve the measurement precision without improving the clocks themselves but rather the measurements. Correlation spectroscopy of two clocks with synchronised measurements and with a shared local oscillator can yield frequency comparisons that are insensitive to laser noise [66, 67]. Therefore, this can circumvent both the dead time errors and the phase projection errors allowing probes beyond the optical coherence and improved stability. It does not improve the stability of the individual clocks it but can allow enhanced measurements of their frequency ratios.

1.4 Thesis outline

The particular avenues selected for investigation in this thesis concern spectroscopy techniques for single and composite clocks with the aim of improving their frequency stability. In Chapter 2, the latest status of the Strontium optical lattice clocks at NPL is presented noting relevant measurement campaigns performed with Sr1 and describing the journey of bringing Sr2 back into operation. Following this, Chapter 3 contains a broader discussion on optical clock stability with reference to the NPL systems. A suite of numerical simulations are used to inform analytical models to understand the relations between different clock operating regimes and the resulting instabilities. In Chapter 4, solutions are proposed for addressing technical noise in optical lattice clocks through engineering of the duty cycle, and the solutions are evaluated on the basis of the instability models. Chapter 5 outlines a study of the stability of the Strontium optical lattice clocks at NPL through synchronous measurements. The implementation of a differential spectroscopy measurement in a hybrid clock setup is summarised in Chapter 6. In Chapter 7, another type of spectroscopy is investigated for addressing noise from external magnetic fields and as an important missing piece of the continuous clock concept. Chapter 8 is reserved for reflections on the themes covered.

Chapter 2

Strontium optical lattice clocks at NPL

The Strontium optical lattice clock experiment at NPL comprises two cold Strontium frequency reference systems. The first generation system, Sr1, which was mentioned in the first chapter already, has been talked about extensively in previous works [68–74]. It is a state-of-the-art optical lattice clock with a recently evaluated uncertainty budget of 4×10^{-18} fractional frequency uncertainty and making contributions to International Atomic Time. The second generation system, Sr2, features a compact pyramid MOT, in-vacuum cavities for 2D enhanced optical lattice configuration, and the possibility of non-demolition detection of the atomic state [64, 72, 74]. This chapter covers the experimental status of the two clocks focusing on recent measurements with Sr1 and on developments in Sr2 towards an operational clock.

Before turning to the NPL systems in particular, it is useful to review the generic operating cycle of an optical lattice clock. Figure 2.1 highlights the most relevant electronic fine-structure energy levels and optical transitions of ^{87}Sr. The ultra-narrow $^1S_0 \rightarrow {}^3P_0$ transition at $698\,\mathrm{nm}$ provides the clock reference for interrogating the atoms with a highly stable laser while the atoms are confined in an optical lattice.

Laser cooling relies on repeated photon scattering to exert radiation pressure on the atoms. Each absorption event transfers momentum $\hbar k$ (with $k = 2\pi/\lambda$) in the direction of the laser beam, giving an average scattering force of order $F \simeq \hbar k R_{\mathrm{sc}}$. By tuning the light slightly red of resonance (detuning $\Delta < 0$), the Doppler shift makes an atom moving towards a beam preferentially absorb from the counter-propagating direction, leading to a velocity-dependent damping force and cooling towards the Doppler limit.

Atoms are produced from a thermal source and are first decelerated in a Zeeman slower operating on the strong $^1S_0 \rightarrow {}^1P_1$ transition at $461\,\mathrm{nm}$. In a Zeeman slower, a spatially varying magnetic field compensates the changing Doppler shift as atoms decelerate, keeping them near resonance with a counter-propagating laser and enabling large velocity reductions. The slowed atoms are captured in a first-stage "blue" magneto-optical trap (MOT) on the same $461\,\mathrm{nm}$ transition, providing high capture velocity and large atom number. In a MOT, three orthogonal pairs of red-detuned, circularly polarised beams are

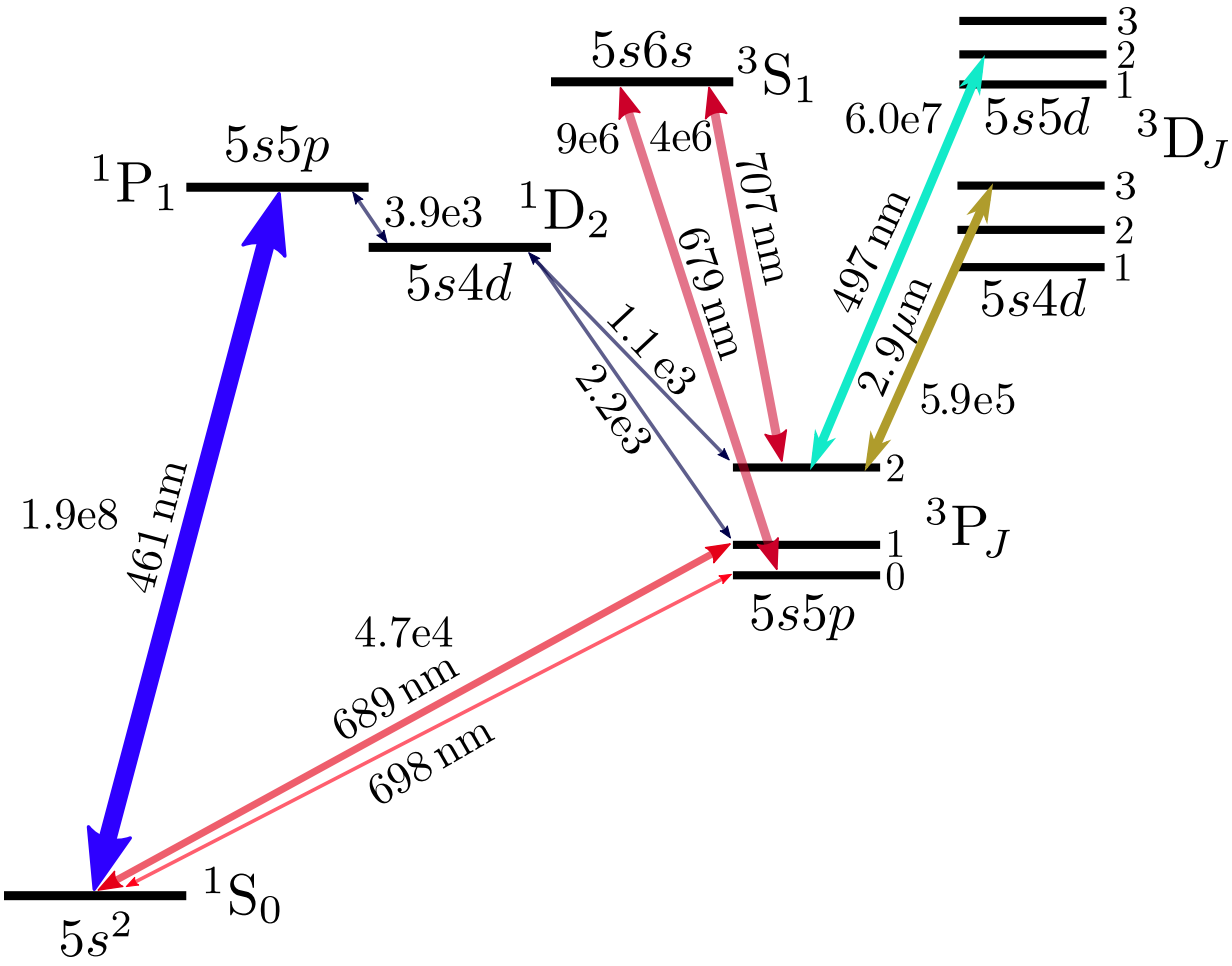

Figure 2.1: **Energy levels and transitions in ^{87}Sr atoms**.

combined with an anti-Helmholtz magnetic field gradient; the resulting position-dependent Zeeman shift makes the light closer to resonance for atoms displaced from the trap centre, producing a net restoring force in addition to Doppler cooling. In this way, a MOT can achieve temperatures as low as its Doppler limit of

$$T_\mathrm{D} = \frac{\hbar\Gamma}{2k_\mathrm{B}} = \frac{\hbar R_\mathrm{sc,max}}{k_\mathrm{B}}, \tag{2.1}$$

which for the 461, nm transition (with $\Gamma/2\pi \approx 32, \mathrm{MHz}$) is $T_\mathrm{D} \approx 0.77, \mathrm{mK}$. In practice, the achieved temperature is often higher due to power broadening and other technical effects, but this broad transition is essential for robust capture.

Because the $^1P_1$ state can decay via $^1D_2$ into the metastable ^3P_J manifold, the 461, nm cooling cycle is not perfectly closed and atoms can be optically pumped into long-lived dark states. Repumping lasers are therefore required to return this leaked population to the cooling cycle. Depending on the chosen scheme, these states are commonly addressed using 679, nm driving $^3P_0 \to {}^3S_1$ and 707, nm driving $^3P_2 \to {}^3S_1$ or 497, nm driving $^3P_2 \to {}^3D_2$, with subsequent spontaneous decay returning population to $^3P_1$ and then to $^1S_0$.

After the blue MOT, the atoms are transferred to a second-stage "red" MOT operating on the narrow intercombination line ${}^1S_0 \rightarrow {}^3P_1$ at $689,\mathrm{nm}$. Owing to its small linewidth, this stage enables much lower final temperatures of $T_\mathrm{D} \approx 180,\mathrm{nK}$, enabling efficient loading into conservative traps, typically using frequency-broadened light and/or a two-phase sequence to improve capture and compression. An alternative approach is to implement a MOT on the $2.9,\mu\mathrm{m}$ transition trapping atoms that decay to ${}^3P_2$ [74]. This can provide a route to directly re-capture atoms in the metastable manifold and can be attractive for certain loading schemes; however, it typically offers a weaker restoring/scattering force (and hence reduced capture velocity) than the blue MOT and has a higher Doppler limit than the $689,\mathrm{nm}$ intercombination line, in addition to the practical challenges associated with mid-infrared laser technology and optics. For these reasons it is an uncommon choice in optical lattice clocks.

The atoms are then loaded into an optical lattice operated near the "magic" wavelength $\lambda_\mathrm{m} \approx 813,\mathrm{nm}$ (not shown in Fig. 2.1). This light is far detuned from strong resonances so that confinement arises from the AC Stark shift (dipole force) rather than photon scattering, and λ_m is chosen to (approximately) cancel the differential lattice light shift between the ${}^1S_0$ and ${}^3P_0$ clock states. Finally, high-resolution spectroscopy is performed on the $698,\mathrm{nm}$ clock transition while the atoms are tightly confined in the lattice (Lamb–Dicke regime), suppressing Doppler and recoil effects and enabling long interrogation times and narrow observed linewidths.

2.1 Sr1 operation

During my time at NPL, I have had the benefit of a working state-of-the art optical lattice clock. One of my main tasks as a new member of the lab was to map out and understand the complex RF electronics systems in Sr1 for implementing frequency and intensity stabilisation loops. This was an opportunity to see how an optical lattice works in very fine detail and proved useful later, when Sr1 was used in several measurements, which will be discussed next.

2.1.1 Towards an optical primary frequency standard

As an exercise in the use of optical standards for timekeeping, optical clocks have started to contribute to TAI steering in recent years. By correcting a Hydrogen maser with optical clocks linked through an optical frequency comb, a stable timescale can be produced and used to inform TAI. Thanks to the help of robust locking algorithms and data processing, we have been able to make a number of on-time TAI submissions with NPL-Sr1, starting from March 2023, as recognised in the BIPM diamond chart, shown in Figure 2.2. The uncertainties of these submissions were mostly close to the uncertainty of the recommended frequency for the Sr clock transition, with the main contributions above this being due to interruptions in the operation time of the clock, during which the unsteered maser frequency accumulates a large uncertainty.

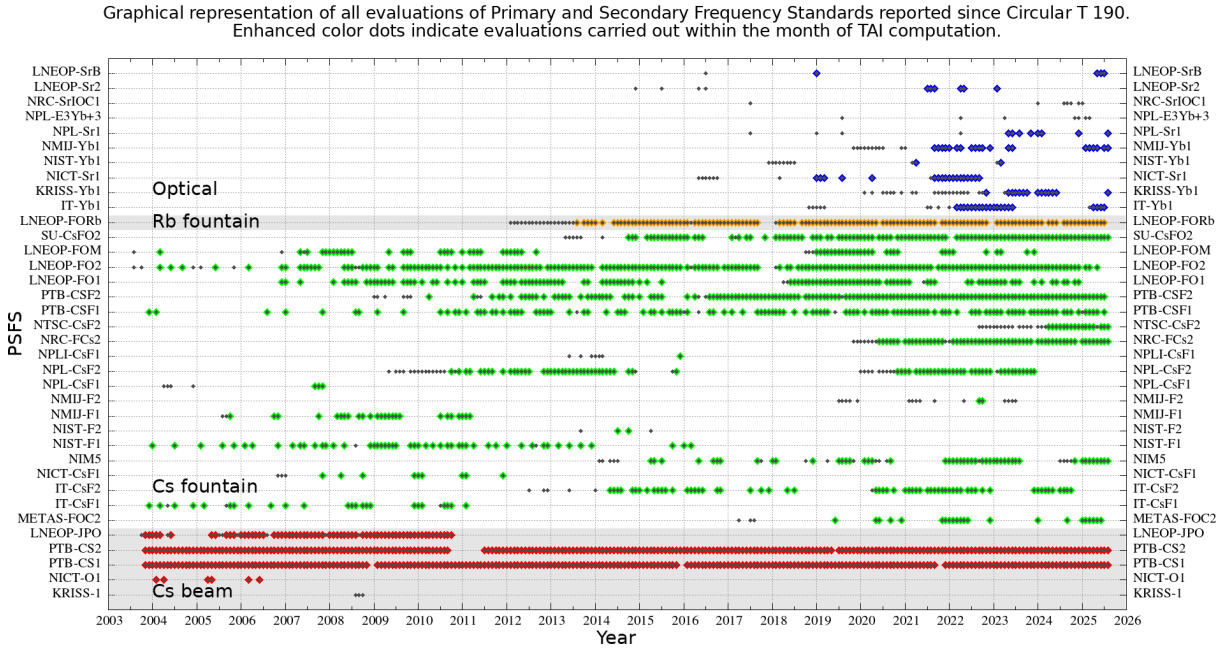

Figure 2.2: **TAI contributions**.Graphical representation of contributions from all atomic clocks steering TAI for every month since 2003. The coloured diamonds indicate on-time submission where the uncertainty evaluations have been made within the month of TAI computation and are colour coded for Cs beam clocks (red) Cs fountain clocks (green), Rb fountain clocks (orange) and optical clocks (blue). Figure obtained from the BIPM website (`https://webtai.bipm.org/database/show_psfs.html`)

As regards the accuracy of the Sr lattice clock frequency itself, the leading source of systematic uncertainty is typically from the BBR shift characterisation, due to the uncertainty in the temperature estimation. For this purpose, an array of 11 temperature sensors around the chamber are used modelling the temperature with a rectangular probability distribution between the minimum and maximum values, as described in [73], which leads to an uncertainty that is significantly larger than the uncertainty in the calibration of the individual sensors. The resulting BBR uncertainty is usually at the low 10^{-17} level. Since the next highest contribution is the lattice light shift at low 10^{-18}, it would be beneficial to increase the confidence of the temperature evaluation.

A more precise determination of the correlation factors between the readings from the sensor array and the temperature sampled by the atoms at the centre of the atomic chamber was recently obtained. Using measurements with an *in-situ* sensor at the location of the atoms, coefficients were found for each of the external sensors, such that all the readings can be used to estimate the temperature instead of only the minimum and maximum values. Although this is yet to be used in a measurement campaign, the calculated uncertainty in the temperature estimation is at the level of 47 mK, limited by the immersion error of the *in-situ* sensor and corresponding to 3×10^{-18} static BBR uncertainty. Additional uncertainty from the dynamic BBR shift components contributes at $< 2 \times 10^{-18}$. Although this improvement would not be noticeable in absolute frequency measurements relevant for

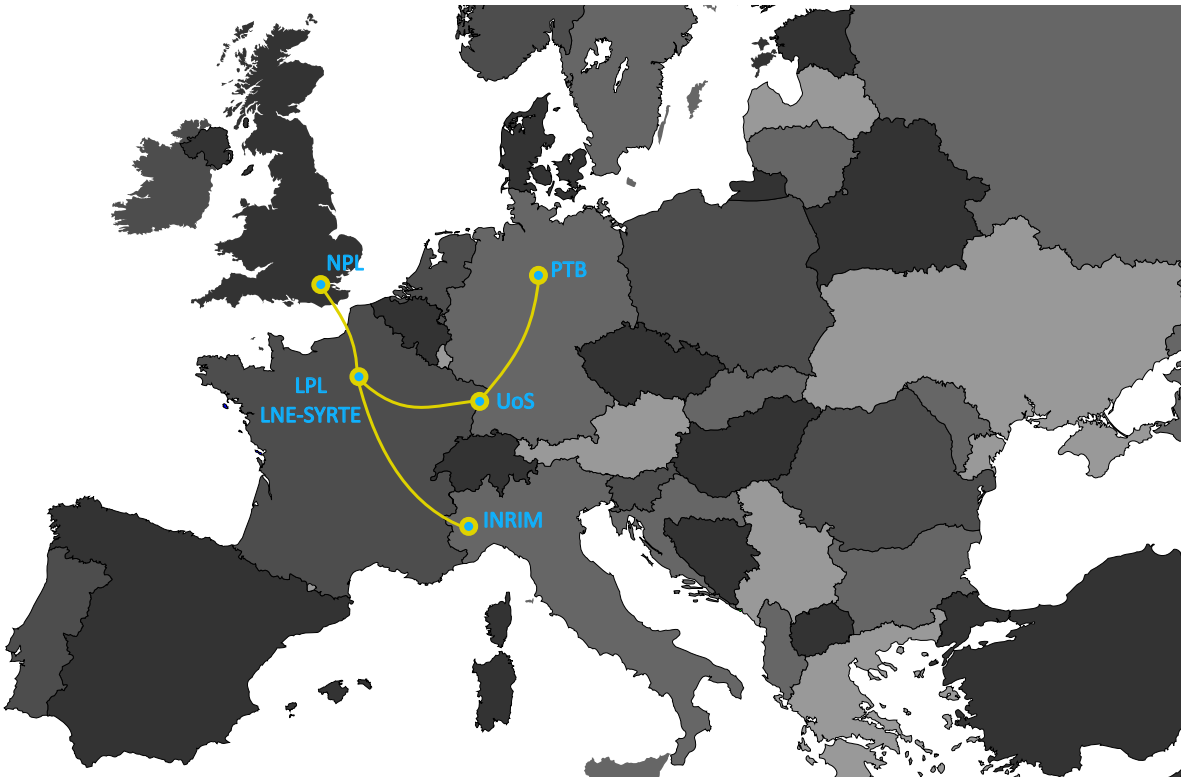

Figure 2.3: **Optical fibre links**. Map indicating the main optical fibre connections linking optical clocks at NPL to other optical clocks in Europe.

TAI submission, it is relevant for comparisons with other optical frequency references.

2.1.2 International clock comparison campaigns

Optical fibre links have been identified as a superior medium for frequency transfer over free space transmission using satellites, with dedicated "dark fibers" the most convenient albeit expensive option [75, 76]. Moreover, sharing data fibres from the internet fibre network using "dark channels" in the telecoms band has been shown to produce similar performance [77, 78]. Using repeater laser stations and Brillouin amplification can support phase coherent transfers over distances as long as a few thousand kilometers [79]. This enables linking optical lattice clocks for international comparisons [80] with no significant degradation of the accuracy due to link noise thanks to its $1/\tau$ averaging.

Sr1 took part in an international clock comparison campaign in 2022 [10] where 10 optical clocks across 6 countries were compared using fibre and GNSS links. This provided an opportunity to verify the frequency of Sr1 against other Sr lattice clocks at SYRTE and PTB, as well as against Yb lattice clocks at INRIM and NMIJ, and Yb^+ ion clocks at NPL and PTB. The frequency ratios that were measured had relatively high uncertainties of $> 10^{-16}$ as attributed to the satellite link noise which was used due to a temporary suspension of the optical fibre link between London and Paris, but nevertheless showed good agreement with the reference values for each frequency ratio.

A more recent campaign involving transportable Strontium optical lattice clocks was conducted during 2023 [20]. The use of transportable clocks removes the need for optical fibre or satellite links, thus avoiding an additional source of noise in the measurement. Although fibre links were still used for the comparison of the stationary clocks, the campaign demonstrated state of the art agreement between all clocks at the 9×10^{-17} level, with precision approaching 10^{-18} in individual ratios for a period of two weeks. Another advantage of the transportable clocks is that they can serve as intermediaries between remote stationary clocks. By using the same transportable system to make frequency ratio measurements at the two locations, the measurement becomes insensitive to the differential gravitational red shift, which otherwise needs to be accounted for through other methods that are accurate at similar levels to current clock uncertainties.

Conversely, due to the high accuracy of optical clocks, frequency comparisons could be used as a tool of geopotential estimation through chronometric means. The Earth is subject to solid earth tides originating from the same gravitational sources as the ocean tides, namely the gravitational pull of the Moon and Sun. The magnitude of the total effect is responsible for deformations in the crust resulting in height changes on the order of 30 cm. Such height differences correspond to gravitational redshifts at the 10^{-17} level, which is resolvable with of state-of-the-art optical clock accuracy, allowing the possibility of detection which ultimately could be used as predictors for earthquakes [81]. However, since these are time varying phenomena, resolving the shifts depends on the stability of the clocks involved.

There are three main types of tidal effects. Semidiurnal effects are related to Earth's rotation causing a particular location on the planet to experience a pair of bulges in a span of 24 hours, with a corresponding effect at the antipode. Diurnal effects have a similar origin but are experienced only once due to the Moon's declination. Besides these, there are other effects which occur on longer timescales and modulate the amplitude of the tides, with peaks twice monthly during new and full Moons when the Earth, Sun and Moon are collinear and further monthly and yearly effects respectively from the elliptical orbits of the Moon around the Earth and of the Earth around the Sun.

An attempt was made during the summer of 2025 to measure tidal effects between Sr1 and the Strontium optical lattice clocks at PTB and at SYRTE. The geographical separation between the institutes results in a time offset between their respective tidal effects resulting in time-varying differential geopotentials. Although the measurement was performed around the aphelion when the Solar contribution is reduced, the amplitude of the variations still reached peak-to-peak amplitudes of 2×10^{-17} for the semidiurnal component, as shown in Figure 2.4 for the last 10 days of June, 2025. Although the measurements could not resolve the oscillations on this occasion, this remains a promising endeavor in the future, as motivated by the simulation presented in Figure 2.4 for the NPL and PTB clocks. The time domain signal contains significant noise, but the Fourier spectrum clearly reveals two peaks around the 24 and 12 hours periods. Additional white phase noise due to the optical link was included in the simulation based on the value inferred from the measurements of optical cavities across the same link [82] and shown to not contribute significantly on relevant timescales.

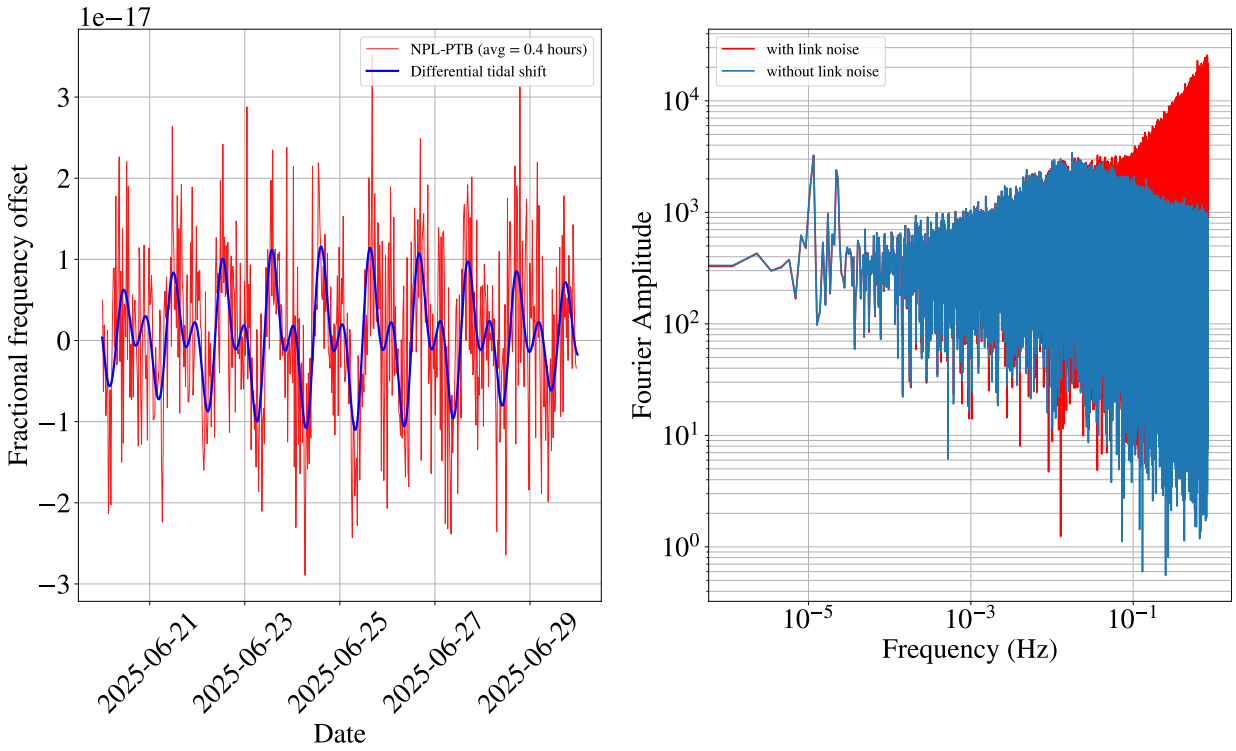

Figure 2.4: **Tidal shift simulation**. *Left*: Time domain fractional frequency difference from simulated operation of the NPL and PTB Sr optical lattice clocks (red solid line) based on clock stability of a few parts in 10^{16} and the expected differential tidal shifts (blue solid line) based on the ETERNA software from the International Geodynamics and Earth Tide Service. *Right*: Fourier transform of the simulation with and without optical fibre link white phase noise. The two peaks at low frequency correspond to periods of 24 hours and 12 hours respectively.

2.2 Experimental upgrades: the revival of Sr2

At the point when I joined the Sr lattice clock team at NPL, although Sr2 had a record of high stability operation [64] and had participated in local comparison campaigns with Sr1 (data published later in 2024 [83]), it was in a sub-optimal state making conducting experiments challenging. This section reviews the changes that were implemented during my placement to address the experimental limitations of operating Sr2.

2.2.1 Shared systems: clock laser and transfer cavity

Although the two Strontium standards are distinct systems, they are able to share some of the optics because of their physical proximity and their spectroscopic similarities. For this reason, the 698, nm clock probe light for Sr2 is derived from that generated for Sr1. The same stable clock light is also used to stabilise the transfer cavity which in turn is used to lock the 922 nm master ECDL, the 689 nm master laser, and the 813 nm SolsTiS laser. From these, the cooling and trapping light for each system is derived. For the first

stage MOT, we have a master laser at 922 nm to which we lock separate lasers for Sr1 and Sr2. For the second stage MOT, we have a 689 nm master laser which we amplify using three injected diodes to generate all the necessary beams for both clocks. Finally, for the optical lattice trap, we use a high power SolsTiS laser which we can simply distribute to both clocks with dedicated modulators for independent frequency tuning and lattice cavity locking.

The clock probe light is stabilised to drive the mHz-level doubly forbidden clock transition with coherence times approaching a second. To be able to perform coherent atomic interrogations, the clock laser needs to have a linewidth that is narrower than the Fourier limited width of the spectroscopic line. For interrogation times > 100 ms, the linewidth is at the level of a few Hz or lower. This is achieved through a few stages of frequency stabilisation. First, a laser diode placed in a Littrow configuration ECDL produces around 30 mW of 698 nm light with MHz level linewidths. Then, a 420,000 finesse cavity with 4.5 kHz linewidth [68] is used as a reference to lock the ECDL using a PDH [84] setup with high bandwidth servo corrections via the diode current and low bandwidth corrections using a piezo stage on the ECDL grating mirror. A second diode is injected with the stabilised ECDL light to generate the light used to probe the atoms. Before that happens, we implement a final stabilisation stage involving an ultra-stable cavity. To transfer the stability of the cavity to the laser, we steer its output using an AOM based on the beat note with an optical frequency comb that is itself locked to an ultra-stable cavity which has been characterised to fractional frequency uncertainties as low as 7×10^{-17} [82]. The frequency comb can also be used to measure the Strontium lattice clock laser against Hydrogen masers steered by primary Caesium standards at NPL thus providing absolute frequency measurements.

The stable 698 nm light is an excellent source of frequency stability for other lasers in the lab. By locking another optical cavity to the clock laser, we obtain a transfer cavity with great long-term stability which we use as a reference for the main laser systems in the lab. To implement PDH locking of all the lasers to the same cavity, we need to bridge the gap between the lasers and the cavity modes. We shift the 922 nm master laser using an AOM, while for the 689 nm laser and the 813 nm laser we generate frequency sidebands with a modulated drive frequency in an EOM. This way we can bridge the frequency gap using the offset sidebands and at the same time add PDH sidebands for locking through the modulation.

The 922 nm master ECDL distribution is depicted in Figure 2.5. A small pick-off is sent to the transfer cavity to perform PDH locking lending it good long-term stability, and then the stabilised light is distributed to various channels. A significant part is sent to the BoosTA tapered amplifier to produce the quantum non-demolition probe and the input light for the old frequency doubling module in Sr2. These are currently not in use but the amplifier has been retained for the possibility of reintroducing the non-demolition probe in the future. The rest of the light is frequency shifted by 85 MHz through an AOM and distributed to the wavelength meter for monitoring and to Sr1 and Sr2 for phase locking of their respective individual 922 nm lasers from which the frequency doubled 461 nm light is derived for the Zeeman slower, magneto-optical cooling and for imaging of atoms. The branch for Sr2 has been recently added to lock a new laser to the 922 nm master and will

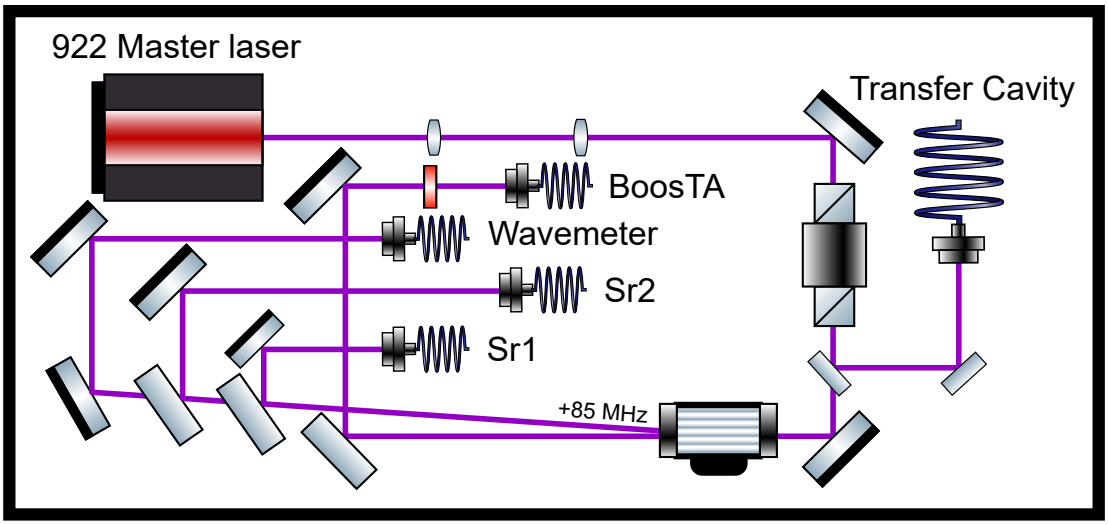

Figure 2.5: **922 nm master laser**. Optical setup for the distribution of **922 nm** radiation from the master 922 ECDL to the wavelength meter, to Sr1 and Sr2 for phase locked loops, and to seeding the BoosTA amplifier for generation of the non-demolition probe. The ECDL is locked to the Transfer Cavity using the PDH technique. The AOM is driven by an **85 MHz** RF signal and the first positive diffraction order is divided between the Sr1 reference, Sr2 reference, and wavemeter.

be discussed in the next section.

The laser systems for generating and distributing the 689 nm light for the second stage magneto-optical cooling has largely remained unchanged from the previous publication [71], with the exception of the extension added for Sr2, which will be presented in section 2.2.3. The locking method for the lattice laser has also been updated to accommodate the operation of Sr2. Due to the higher finesse of the in-vacuum build-up lattice cavity, the sensitivity to frequency and intensity noise is higher, and because of limitations in the piezo at high frequencies, it can more easily lead to parametric heating [72]. Although the intensity stabilisation setup has remained unchanged from [72], the frequency lock to the transfer cavity has been improved by making it resilient against long term drifts.

As seen in Figure 2.6, we form 157.5 MHz sidebands on the laser to bridge the frequency to the transfer cavity mode using an EOM, adding 20 MHz electronic sidebands for PDH locking. The offset frequency is generated using a voltage-controlled oscillator (VCO). Instead of providing a DC voltage to the VCO, which would be susceptible to long-term drifts, we use a phase-locked loop (PLL) to centre the output of the VCO to the 157.5 MHz signal from a synthesizer. We combine the regulated voltage which drives the VCO with a 20 MHz signal to produce the required electronic sidebands. We actuate the PDH corrections in two ways distinguished by their bandwidth. The low bandwidth corrections are applied to tune the resonator of the SolsTiS laser, which provides sufficient stability for locking the lower-finesse lattice cavity in Sr1. For Sr2, we also feedforward the high bandwidth corrections by injecting them into the PLL signal using a summing amplifier and then using the PLL signal to drive an AOM in the Sr2 path.

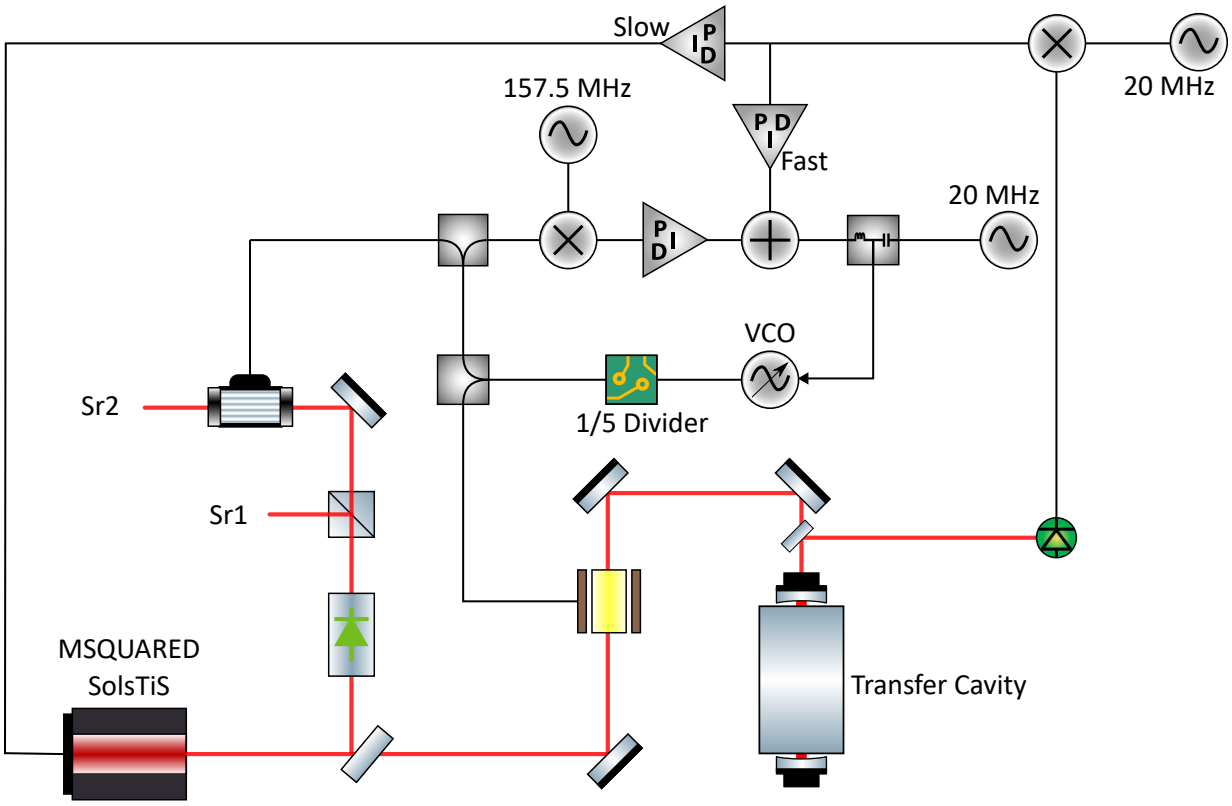

Figure 2.6: **813 nm lattice laser frequency stabilisation**. Optics and RF electronics for the 813 nm lattice light showing the PDH lock to the transfer cavity and the PLL for stabilising the VCO-generated electronic sidebands.

2.2.2 First stage MOT and atom source

The original setup for the first stage cooling on the broad ${}^1S_0$ to ${}^1P_1$ transition involved light from the 922 nm master extended cavity diode laser (ECDL) seeding a tapered amplifier and frequency doubled by a second-harmonic generation (SHG) crystal to obtain light at 461 nm. Most of the light would be used for the MOT beam and the fluorescence probe beam which shared the light since they operate at different times in the cooling sequence. A small amount of light was used to seed an injection-locked diode to produce the high intensity slowing beam. However, degradation of the SHG module led to gradual loss of optical power, so using 500 mW of power at 922 nm we were generating only 80 mW at 461 nm, leaving around 20–25 mW of power in the MOT beam.

We have upgraded the setup using a system with integrated ECDL + TA/SHG components purchased from Toptica, similar to that of Sr1. The laser is phase locked to the 922 nm master laser then amplified through a tapered amplifier and frequency doubled through an SHG crystal sitting in a bow tie cavity. This can produce close to 1 W optical power at 461 nm which gives us a maximum optical power of around 600 mW after delivery via a high power fibre. It thus removes the dependence on using an injected diode for the slowing beam, making the system more robust, and produces more optical power than the previous setup.

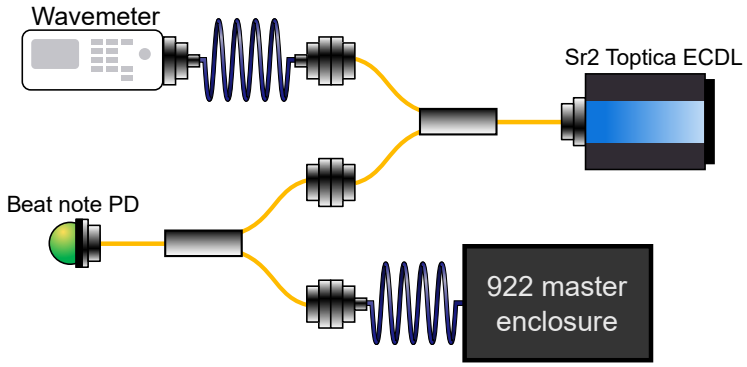

Figure 2.7: **922 nm master PLL**. Optical setup for the in-fibre phase locked loop of the Sr2 922 nm diode to the master 922 nm diode.

For the Sr2 offset locking, we implement a phase locked loop (PLL) by creating a beat note between the 922 nm master light and the Sr2 922 nm diode. The beat note is compared to a reference frequency in a phase/frequency discriminator generating an error signal based on which we steer the Sr2 frequency actuating on the laser diode piezo. We have elected to use fibre splitters/couplers to create the beat note (see Figure 2.7). Because of availability, we use fibre couplers with a calibration wavelength of 850 nm which have a nominal split ratio of 50:50. At our wavelength, this becomes an 85:15 ratio. We can use this to our advantage to only sample the smaller fraction in the first coupler for light used in the wavelength meter and to balance the powers out of the second coupler since the Sr2 laser diode provides significantly more power than the 922 nm master pick-off. We select the reference frequency and polarity in the feedback loop such that we end up with a -10 MHz negative offset in Sr2 with respect to the pick-off light from the master ECDL. This frequency has been chosen to ensure that the 461 nm light generated will have the same frequency as the SHG light in the old setup. We achieve a very robust lock with up to 2 MHz bandwidth that routinely stays locked for weeks. A similar setup is implemented in Sr1 to produce the beat note but using free space optics and is set such that it locks the Sr1 922 nm ECDL to the pick-off light from the master ECDL with a frequency offset of -85 MHz.

The stabilised 922 nm diode in Sr2 is amplified by a tapered amplifier reaching powers of up to 3 W. This can produce up to 1 W of power at 461 nm through the cavity SHG crystal, which we send via a high power fibre to the experiment, ending with a maximum of 600 mW of power. On the clock side, we split the light into two branches using a PBS cube, as shown in Figure 2.8. The reflected light is used to produce the MOT beam and the fluorescence probe beam, whereas the transmitted light is used in the Zeeman slower. A half waveplate before the cube is used to adjust the split ratio. We normally operate with a 3:1 (T:R) ratio in the cube, giving more power to the slowing beam arm to compensate for the losses in the fibre on that path. Because we observed limiting variations in the power split ratio due to changes in the polarisation of the fibre transmitted light, we also added another PBS cube to clean up the polarisation.

To obtain the right frequencies for each beam (see Figure 2.9), we use three different AOMs. We further red detune the slowing beam with a negative pass AOM at 170 MHz,

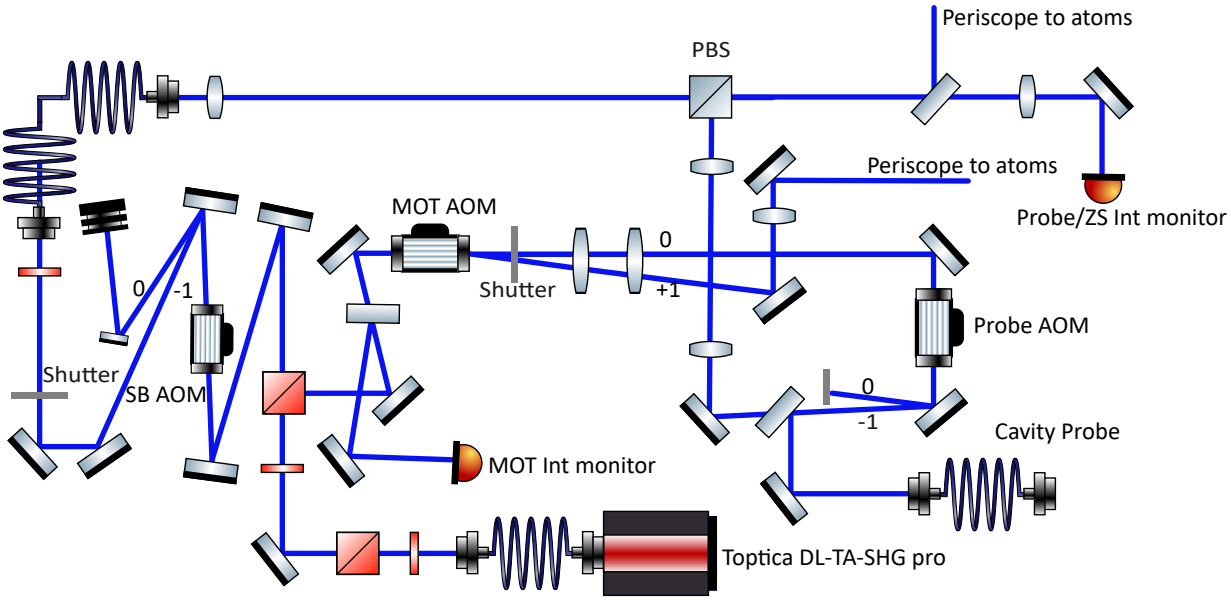

Figure 2.8: **461 nm light distribution**. Optical setup for the distribution of the 461 nm slowing beam (SB), MOT, and probe. A pick-off of the probe light is used to deliver light to the cavity for atomic state detection as described later in Section 2.2.4.

while we increase the MOT frequency by an AOM driven at 265 MHz. The fluorescence probe is derived from the MOT beam as the non-diffracted order of the MOT AOM, and its frequency is then tuned to be resonant with the Sr transition by an AOM driven at 291 MHz. The fluorescence probe and the slowing beam can be combined through a PBS cube thanks to their orthogonal polarisations before being sent to the science chamber. The MOT beam is sent to the delivery breadboard where it is overlapped with the repumping and the red MOT beams before delivery to the atoms.

Because the polarisation out of the high power fibre is not perfectly stable, we need to stabilise the intensity for each arm separately. To do this, we first implement an intensity servo to stabilise the MOT arm by actuating on the TA current based on the signal from a photodetector on that path. This will have an impact on the SB arm as well, so we implement a separate intensity servo by modulating the drive amplitude of the slowing beam AOM using a photodetector after the fibre and the PBS cube used to merge the slowing and fluorescence beams, thus also correcting for polarisation fluctuations through the fibre. Even though we run the TA at around 80% current, we still generate enough light to obtain 50 mW in the MOT beam and 60 mW in the slowing beam before delivery to the atoms.

Repumping light

The lasers used to close the blue MOT transition by repumping the atoms leaking to the $5s4d\ ^1D_2$ state have also been changed. Out of the 1-in-50,000 atoms that leak, two thirds make it to the $^3P_1$ red MOT state from where they can decay to the ground state relatively quickly and rejoin the cooling mechanism [85]. The other third decays to the long-lived

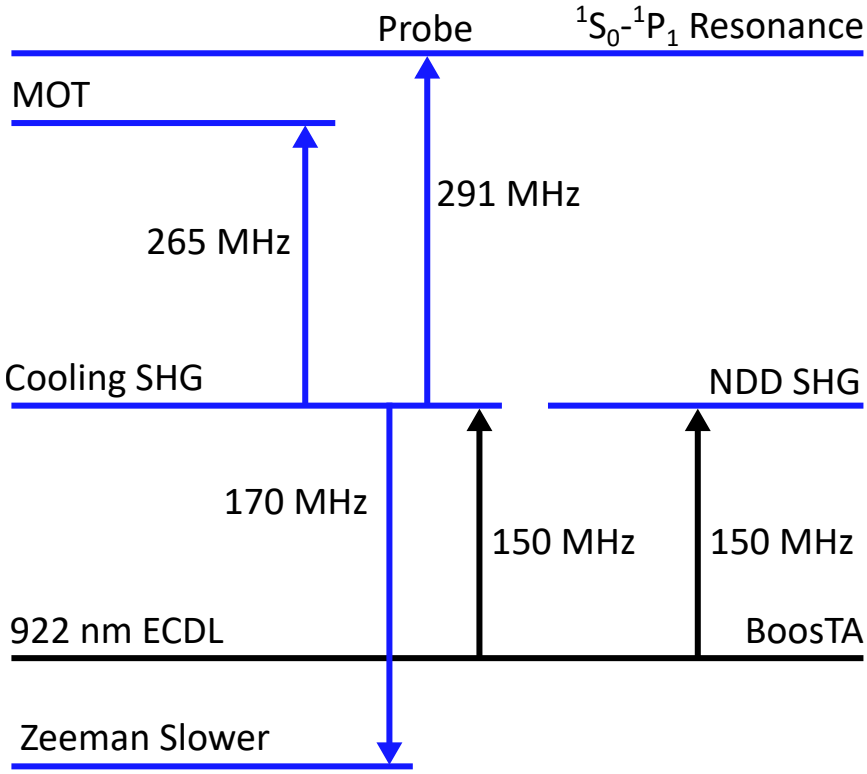

Figure 2.9: **Frequency diagram for the 461 nm light used in Sr2**.

$^3P_2$ state where atoms become transparent to the cooling light. Previously we have used the 497 nm transition to repump the dark atoms from $^3P_2$ via the $5s5d\ ^3D_2$ state. Because of a non-zero decay rate to the clock state $^3P_0$, we also had to address those atoms using the 679 nm transition via $5s6s\ ^3S_1$.

We previously generated the two frequencies using an ECDL at 679 nm and an ECDL at 994 nm sent to a frequency doubling crystal. However, degradation of the frequency doubling crystal led to gradual loss in the efficiency of the conversion. Blue MOT measurements in Sr2 revealed that we can achieve saturation of the repumps at 2.5 mW for the 497 nm light, which was close to the maximum that we could deliver after fibre to the atoms. Because of further degradation, however, and because the light was shared between Sr1 and Sr2, we ended up with less than 1 mW in each clock, even after replacing the 994 nm laser diode. This made simultaneous operation of the two clocks not feasible. In an attempt to obtain a more robust 497 nm source, we built an ECDL with output directly at 497 nm similar to the design in [86]. This was unsuccessful because of the small gain in that wavelength range for laser diodes that were available on the market. A brief attempt to inject a laser diode with the small amount of 497 nm light from the SHG proved equally unsuccessful.

We finally landed on a different repumping scheme using the 707 nm transition to $5s6s\ ^3S_1$ instead of the 497 nm transition. This was convenient because we could find promising new lasers operating at that wavelength and because the second laser required in the scheme is the 679 nm which we already had. We use a Micron laser from Sacher

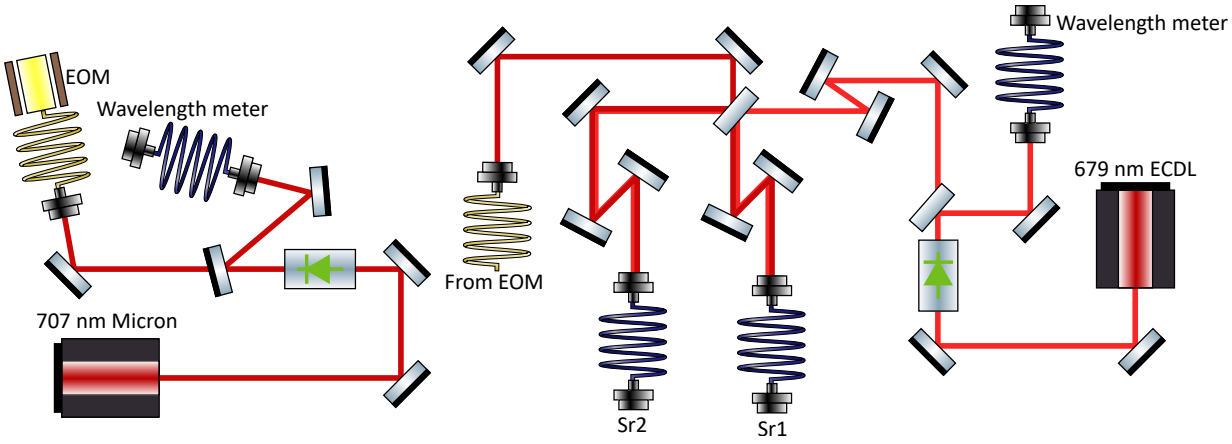

Figure 2.10: **Lasers for blue MOT repumping**. Frequency diagram for the generation and distribution of light for the 707 nm and the 679 nm repumping transitions.

Lasertechnik tuned to 707 nm with a butterfly package laser controller from Koheron. This results in a very stable and easily tuneable laser, which we frequency-stabilise by actuating on the temperature controller with a simple digital servo based on the wavelength meter readings. A similar frequency steering is implemented for the 679 nm ECDL with the distinction that the corrections are actuated through a piezo stage on the grating mirror mount. The optical setup is illustrated in Figure 2.10. We generate sidebands for the 707 nm transition using a waveguide EOM with a combination of drive frequencies to address atoms in different m_F hyperfine levels of the $^3P_2$ state. The output of the waveguide is then combined in free space with the 679 nm light using a partial mirror that also acts to distribute the combined light into two channels, for Sr1 and for Sr2 respectively. The resulting optical power after fibre delivery to the atoms is a little over 1 mW in each wavelength for each clock.

The 707 nm power is limited by a 5 dB insertion loss in the waveguide EOM. As a way to overcome this, we have recently implemented EOM-free sidebands in a second identical 707 nm laser by applying the modulating signal to the diode current instead of the EOM. To test this setup, we compared the loading rate and lifetime of the blue MOT in Sr2 with the two lasers. Figure 2.11 shows the advantage of increasing the optical power. This technique can deliver higher optical power by a factor of 3 and at the same time simplify the setup and reduce costs.

Strontium oven

Modifications to the vacuum components aimed at increasing the operability of the Strontium oven have also been implemented. The crucible has been replaced by one with a new design featuring a nozzle with laser drilled holes. Furthermore, a short bellow that used to connect the crucible to the differential pumping stage has been removed to reduce the number of degrees of freedom and facilitate the alignment of the atomic beam. For the same purpose, a 6-way cross with two view ports has been added just after the mouth of the oven. This allows us to align the slowing beam into the oven observing fluorescence of

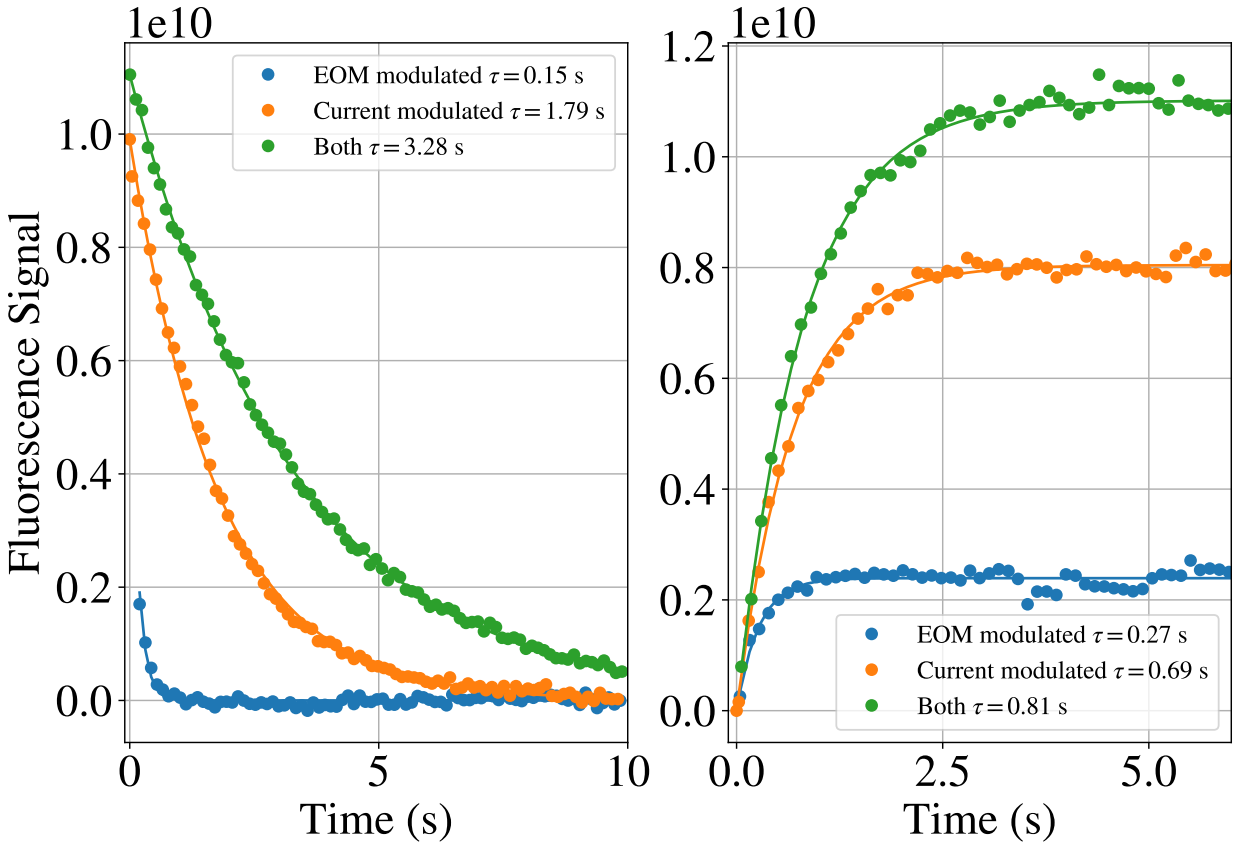

Figure 2.11: **Blue MOT with 707 nm repump lasers in Sr2**. *Left*: Fluorescence vs wait time after turning off the slowing beam and keeping the MOT beam and repumping beams on, obtained while using the EOM modulated 707 nm light, the current modulated 707 nm light, and both sources together. The solid lines indicate exponential fits with the decay constants quoted in the legend. *Right*: Fluorescence counts vs loading time for the same three cases as in the left plot. The times quoted in the legend correspond to saturation time constants determined from the fits.

the atomic beam from the top view port. Of course, we also used the opportunity to put in a fresh batch of dendritic Strontium.

Magnetic trap lifetime

As an additional check we implemented a magnetic trap to investigate the background pressure in the science chamber. We followed the method described in [87] and [88] to magnetically trap $^3P_2$ atoms, selected fort their high m_j number. This state is accessible from the blue MOT state $^1P_1$ building up gradually during the blue MOT if the repumping beams are not used. This makes them transparent to the MOT but susceptible to the magnetic field potential if they have $m_j > 0$. To compensate for the reduced loading rate in the absence of repumping, we use ^{88}Sr to achieve better atomic signal against background scatter noise from the MOT beam. After running the blue MOT for 2 s we turn off the MOT beam and the slowing beam, keeping the MOT coils and compensation coils currents

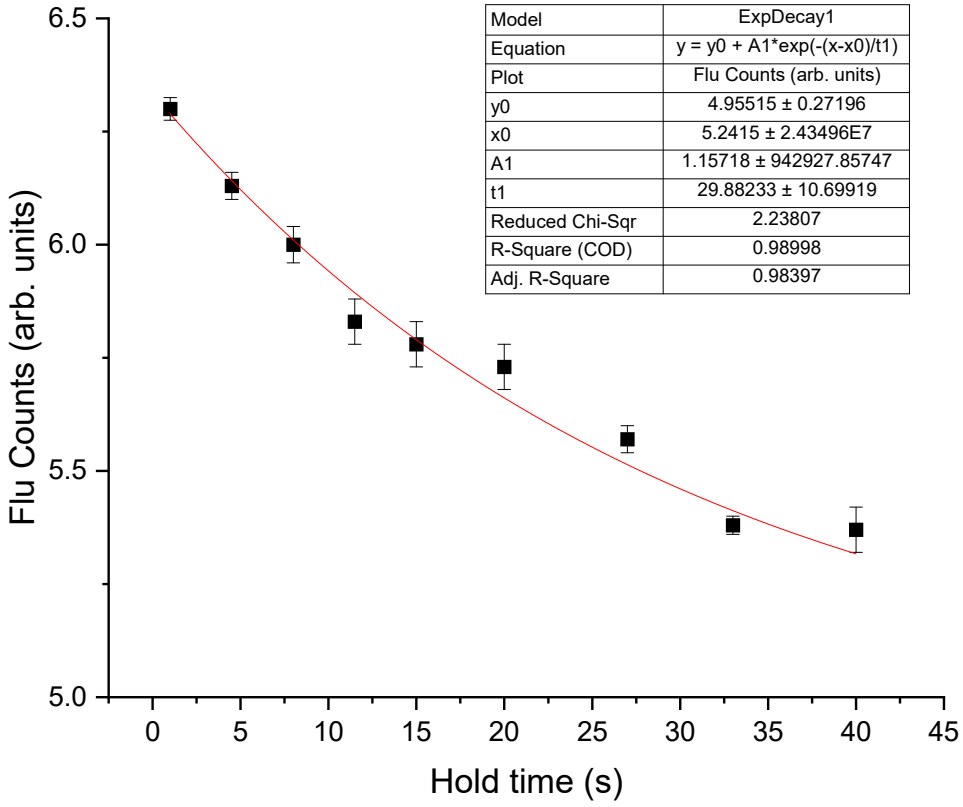

Figure 2.12: **Magnetic trapping of ^{88}Sr**. The fluorescence signal recorded using the MOT beam after holding the atoms in the magnetic trap for different hold times. Error bars represent the standard deviation across repeats.

at the same values. After a variable hold time in the magnetic trap, we image the atoms with the MOT beams, this time applying the repumping beams to bring atoms to the ground state for imaging.

The exponential decay of the atomic population shown in Figure 2.12 yields a lifetime of around 30 s, in agreement with our previous measurement [72], although with a significant uncertainty. Using the empirical relation from [72] we can estimate the residual background gas pressure at 1×10^{-10} mbar. Even if using the lower end of the lifetime estimate, we can still place a limit of $< 2 \times 10^{-10}$ mbar, especially considering the BBR quenching-reduced lifetime of the $^3P_2$ of a few 100 s at an ambient temperature of 300 K [89].

The magnetic field also affects the MOT loading as shown in Figure 2.13. A higher MOT coil current results in stronger fields and higher field gradient. On one hand this increases the capture velocity resulting in a higher loading rate at short times. At the same time, the steeper gradient reduces the volume of the atom cloud thus increasing density losses so that the saturation point is lower. We typically operate with a current around 60

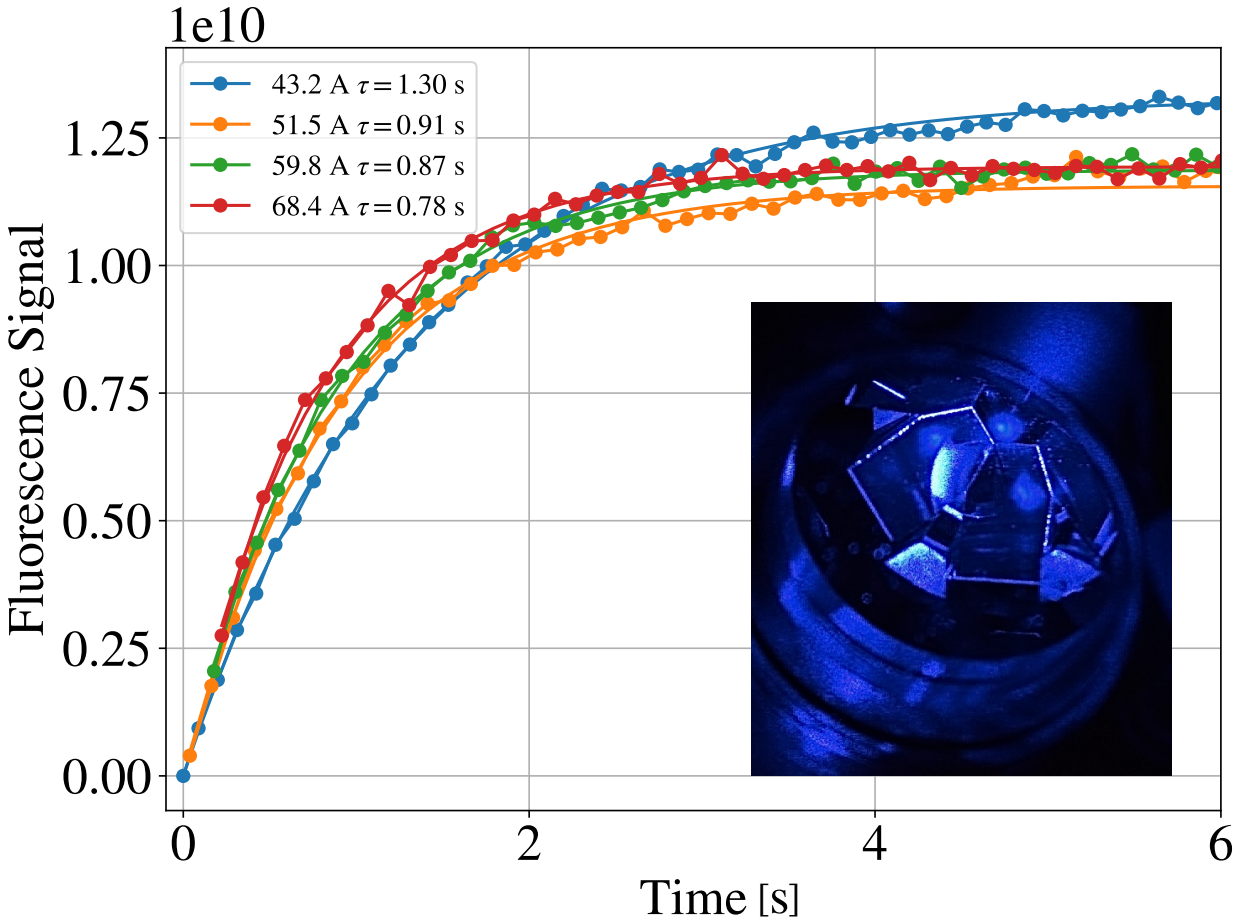

Figure 2.13: **Blue MOT vs magnetic field gradient**. The fluorescence signal from the blue MOT is plotted during the load time for different MOT coil currents. Image shows the pyramid MOT and main atom cloud as well as a couple of reflections.

A, prioritising the loading rate rather than the saturation point.

2.2.3 Second stage MOT

In previous publications, Sr2 was using the MOT formed on the 2.92 μm transition between the $5s5p\ ^3P_2$ and $5s4d\ ^3D_3$ states [74]. Since then, it has been modified to use the standard 689 nm MOT. Having already a 689 nm system for Sr1, the extension to Sr2 only required the addition of an injected diode seeded by a pickoff beam from Sr1, as depicted in Figure 2.14. The pickoff beam sampled at an intermediate point in the Sr1 setup having a frequency positively detuned from the MOT by 803 MHz is frequency shifted negatively by a double passed AOM driven at 281 MHz. This then seeds the Sr2 diode whose output is further detuned by an AOM driven at 241 MHz giving it the right frequency for the MOT. We also run the diode output through an EOM which can be used to add sidebands at 1.464 GHz for the 'stirring' beam. The frequency steps are represented in Figure 2.15

Once we generate the correct frequencies, we send the 689 nm light near Sr2 via fibre and

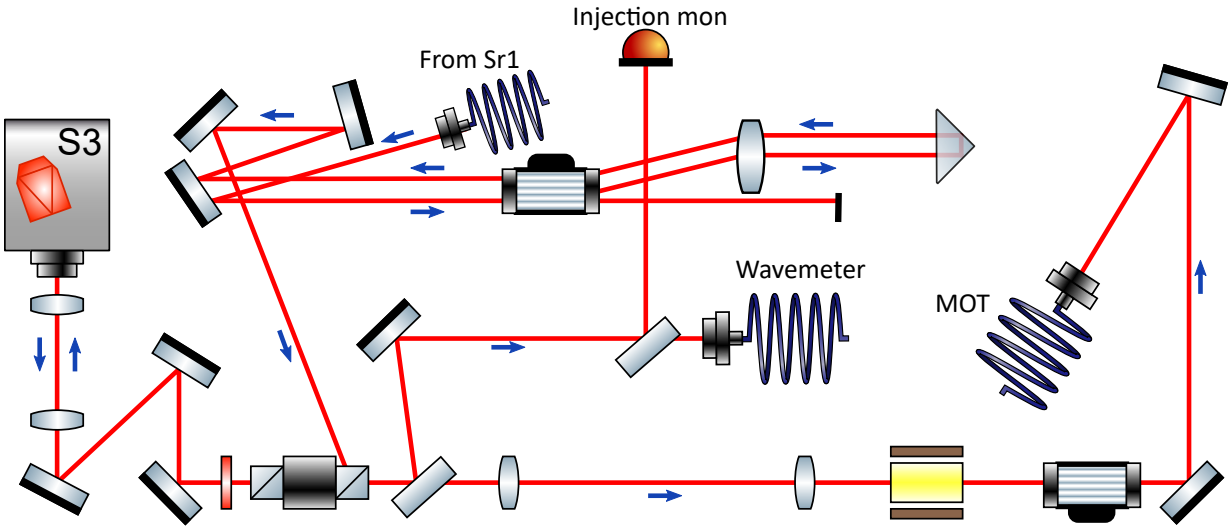

Figure 2.14: **689 nm light generation setup**. Optical setup for the generation of the 689 nm light used in Sr2, showing the injected diode seeded by a pickoff from the Sr1 'stir' beam, the bridging AOM, the shifting AOM, and the EOM for generation of the 'stir' beam sideband.

we distribute it into three channels, as shown in Figure 2.16. The main channel is for the MOT beam and is sent to the delivery breadboard via a periscope mirror pair. The other two channels are picked off from the MOT beam and used to generate the spin polarising beams. A second reflection from the beam sampler used here reaches a photodetector to monitor the intensity of the light and to stabilise it by modulating the drive amplitude of the AOM before the fibre. We combine the spin polarising beams through a PBS cube after rotating the polarisation of the σ^- beam, and we send them to the atoms via a second periscope mirror pair and finally a quarter waveplate for conversion from linear to circular polarisation. In the state preparation stage when we engage a spin polarising beam, we reduce the amplitude of the EOM drive to keep most of the power in the carrier at the MOT frequency. The frequency sweep necessary to accumulate atoms in the $m_F = \pm 9/2$ stretched states in this stage is done by varying the frequency of the injected diode through the bridging AOM applied to the seeding light.

2.2.4 Atomic state detection

Another modification to Sr2 involves the detection stage. Light at 461 nm is sampled from the probe beam and sent to the lattice cavity for fluorescence imaging. We have initially set it up to facilitate the process of overlapping the MOT with the lattice trap which otherwise proved challenging due to the long break in operation of Sr2 and to changes in the external magnetic field. As shown in the comparison in Figure 2.17, it turned out to also be a very efficient imaging beam due to the low scattering rate and power enhancement from the cavity, also opening the door for potentially longer imaging times through Sisyphus cooling with a blue detuned probe mediating recoil heating.

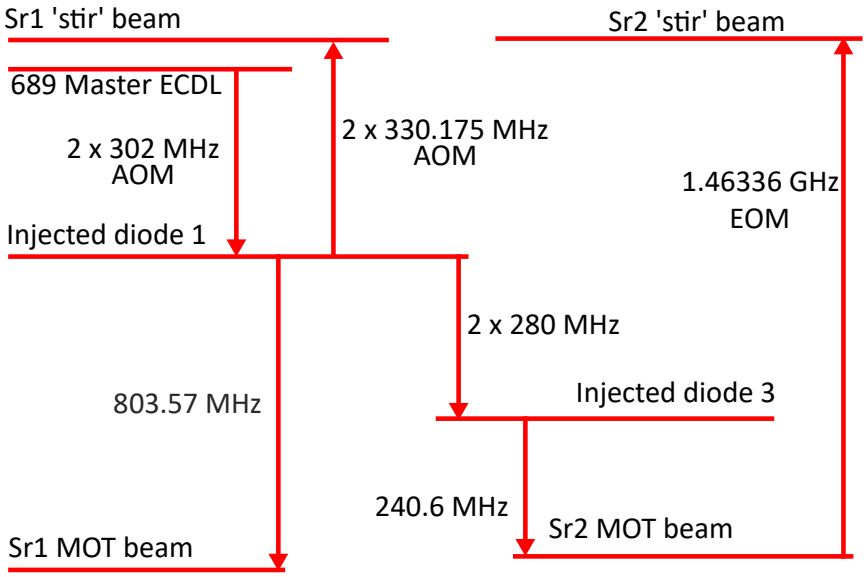

Figure 2.15: **Frequencies at different stages in the 689 nm light system for Sr1 and Sr2**.

2.2.5 Measurement cycle

A typical clock cycle (Figure 2.18) consists of three main stages: atomic preparation, spectroscopy, and detection. To prepare the atoms, we first load the atoms in a blue MOT engaging the slowing beam and MOT beams in a high gradient quadrupole magnetic field. This last around 300 ms and should reach Doppler-limited temperatures of 720 μK. Following this, we transfer the atoms to a broadband stage red MOT which uses a 30 kHz modulation to create a frequency comb over a range of about 2 MHz bridging to the 7.5 kHz narrow transition. The modulated stage lasts around 100 ms after which the intensity is ramped down with a high gradient for 150 ms, and then with a small gradient for another 100 ms. The sub-μK temperatures reached at this point allow us to load the atoms into the lattice trap.

Before starting the spectroscopy stage, we prepare a clean atomic state to improve the spectroscopic contrast. We do this by moving the atoms into the stretched $m_F = \pm 9/2$ substates of the ground state, gradually addressing higher m_F substates using σ polarised light on the 689 nm transition and a frequency sweep. Once the atoms are spin polarised in the desired stretched state, we apply a clean-up procedure. This consists in a short (16 ms) clock pulse that coherently drives the atoms to the excited clock state followed by a short clearout pulse of the 461 nm MOT to blow out any atoms left in the ground state, thus ensuring that all the remaining atoms are in a pure clock state.

Because of this preparation method, for the spectroscopy stage we drive atoms from the excited state to the ground state, which is approximately symmetrical to doing it the other way because of the relatively short interrogation times compared to the minute-long lifetime of the doubly forbidden clock state. We then apply a number of pulses of the clock probe depending on the spectroscopy protocol (i.e. Rabi, Ramsey or dynamical decoupling).

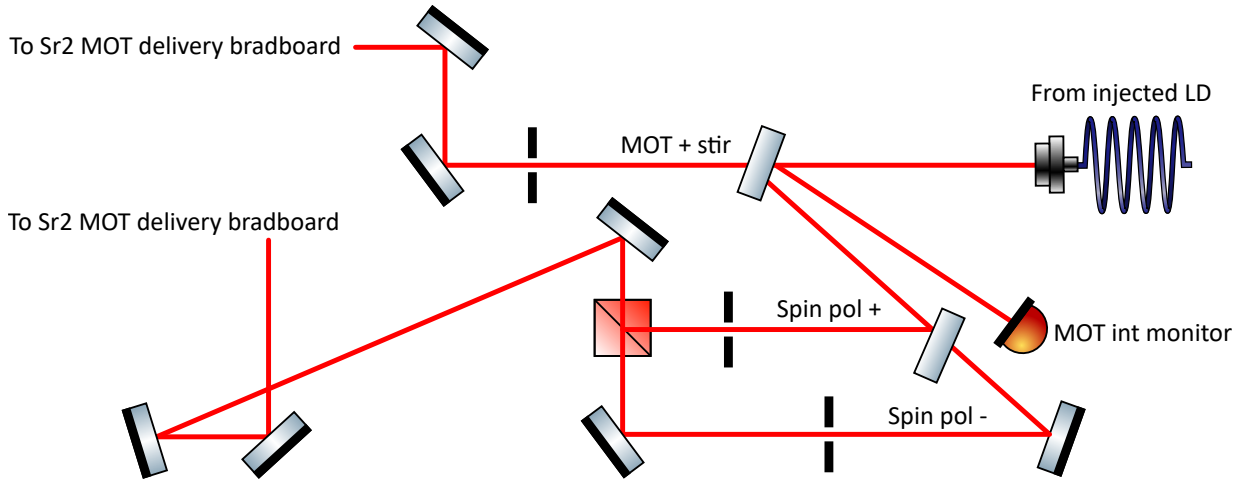

Figure 2.16: **689 nm light distribution setup**. Optical setup for the distribution of the 689 nm light used in Sr2, showing the two delivery channels to the atomic chamber: the main beam containing the MOT and stir frequencies and the pick-off beam for spin polarising.

During the spectroscopy and state preparation stages, we apply a small magnetic bias field to separate the m_F sublevels and be able to resolve different transitions.

Finally, to detect the atomic state after the interaction with the clock light, we measure the excitation fraction using shelving detection: we use a fluorescence probe at 461 nm to first image the ground state atomic population, then after applying the repumps to drive the excited state atoms to the ground state, we image the excited state atomic population in the same way. After each fluorescence pulse, the atoms in the ground state heat up enough to leave the trap and the detection area. A third image is taken of the background at the end which will be subtracted from the image of the atoms.

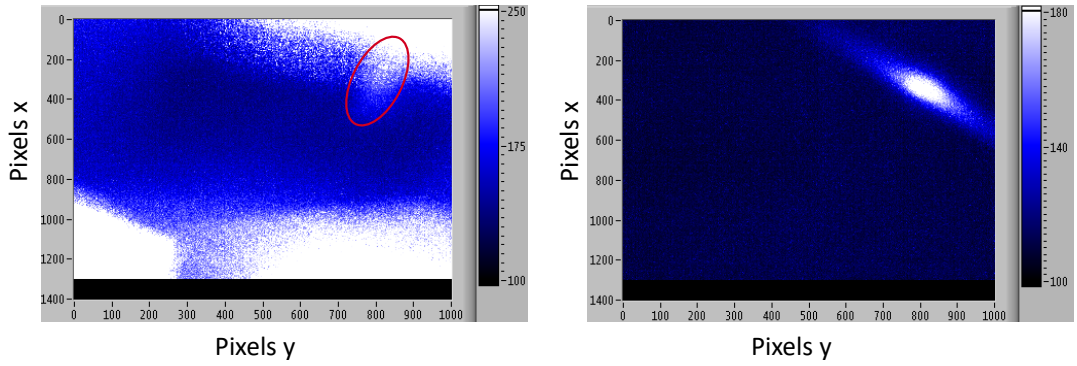

Figure 2.17: **Fluorescence probes**. *Left*: Screenshot of the camera reading of a narrow band low intensity red MOT using the conventional fluorescence probe. The ellipse indicates the approximate location of the atom cloud. *Right*: Screenshot of the same MOT but using the cavity coupled fluorescence probe.

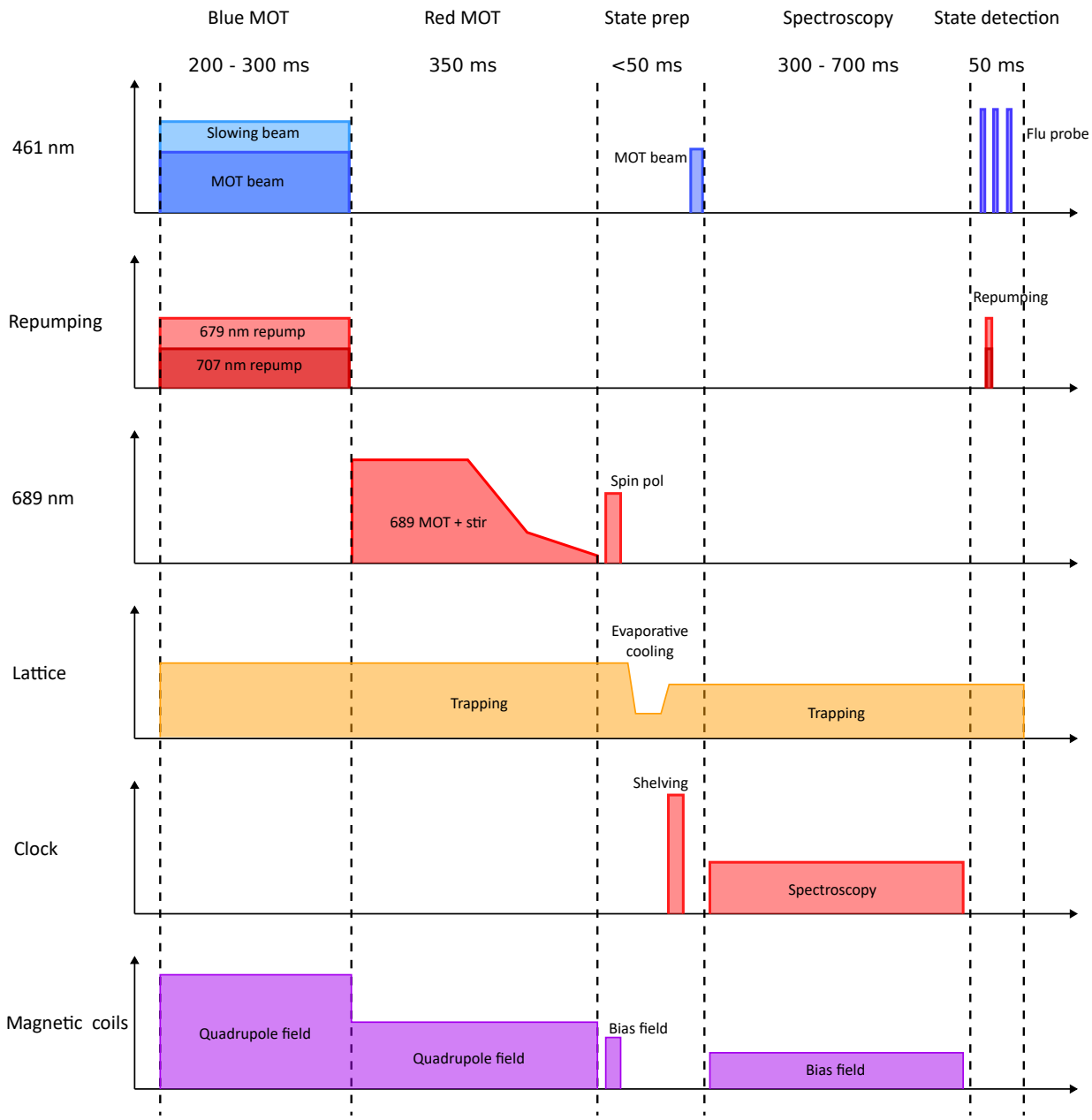

Figure 2.18: **Typical clock cycle for Sr2**. The preparation and spectroscopy steps are illustrated through the amplitude of various signals over time in arbitrary units. The time estimates at the top are approximate and can be changed through optimisation.

Chapter 3

Stability limits in optical clocks

Optical clocks use atomic transitions with high Q and with very good isolation from or characterisation of external perturbations so that the uncertainty in the transition frequency is very low. Optical clocks have been reported with uncertainty budgets at or even below the 10^{-18} level [10–13, 90]. However, instability introduces statistical uncertainty in the clock frequency which requires averaging over a time interval to approach the accuracy of the frequency reference. The instability imposes a trade-off between the precision and the time resolution of the measurement which can limit the detection of time varying phenomena

The accuracy of a clock's frequency is concerned with the time-varying frequency offsets, $\Delta(t) = \nu(t) - \nu_0$, between the real clock frequency, $\nu(t)$, and its nominal value, ν_0. For generality, it is useful to look at the fractional frequency fluctuations of the oscillator, $y(t) = \Delta(t)/\nu_0$. These are typically quantified through the Allan variance (AVAR) defined as the average squared difference between mean frequencies in consecutive averaging time intervals τ [91]

$$\sigma_y^2(\tau) = \left\langle \frac{1}{2}\left[\overline{y}_{n+1}(\tau) - \overline{y}_n(\tau)\right]^2 \right\rangle, \tag{3.1}$$

where averages over intervals τ are used

$$\overline{y}_n(T) = \int_{(n-1)T}^{nT} y(t)dt. \tag{3.2}$$

Another way to characterise frequency fluctuations is the Power Spectral Density (PSD) which is a frequency domain picture of the noise while the Allan variance is a time domain picture with exact relations converting between the two metrics [1], as shown in Table 3.1 for a selection of relevant noise types. Although phase modulating noise is relevant as it generally affects the frequency stability, for most of this thesis, the discussion will refer to frequency modulating (FM) noise unless otherwise specified. Oscillators are characterised

[1]Except for white phase noise and flicker phase noise, which have the same Allan variance but different PSD.

through a model consisting of several types of frequency noise depending on the time correlation. White noise is uncorrelated, so it averages down as $1/\sqrt{\tau}$.

Table 3.1: Power spectral density and Allan variance for common noise types

Noise type	$S_y(f)$	$\sigma_y^2(\tau)$
White FM	h_w	$\frac{1}{2}\frac{h_\mathrm{w}}{\tau}$
Flicker FM	$h_\mathrm{f} f^{-1}$	$2\ln(2)h_\mathrm{f}$
Random walk FM	$h_\mathrm{r} f^{-2}$	$\frac{2\pi^2}{3}h_\mathrm{r}\tau$

An atomic clock works as a servo which repeatedly measured the frequency offset of a local oscillator (LO) from a reference frequency and then corrects it. In particular, the oscillator is a narrow linewidth laser and the frequency reference is an atomic transition with a long-lived excited state. Repeated interrogations of the atoms by the laser generate an error signal from which frequency corrections are derived and applied to steer the laser towards the resonance. The oscillator is usually stabilised to a high-finesse cavity and has a noise spectrum typically formed from a mix of noise types with the stability limit given by the flicker floor [45] due to thermal fluctuations in the cavity mirror coatings.

An ideal hypothetical servo would be able to cyclically measure the frequency offset exactly and then apply a correction accordingly. The stability of such a system is illustrated in Figure 3.1. The duration of the measurement cycle imposes a limit on the time scales at which the frequency can be corrected, thus on shorter intervals the clock output matches the local oscillator. For times on the order of the servo cycle, the instability is slightly higher because of the corrections. At longer time scales the stability starts to improve averaging down as $1/\sqrt{\tau}$ with a level determined by the laser noise, the servo time (correction rate) and the gain. Monte Carlo simulations of this servo scheme confirm these features (see Figure 3.1 and Figure 3.2).

In real life, the frequency offset $\overline{\Delta}_n$ in a cycle is estimated indirectly by measuring the atomic excitation after the atoms interact with the laser light. For small frequency offsets, the excitation fraction changes linearly. However, the measurement is not immune to noise, so we end up with an error signal:

$$\epsilon_n = D\overline{\Delta}_n + \eta_n, \tag{3.3}$$

which contains a component proportional to the frequency offset and a random component which degrades the servo corrections and the resulting instability.

The narrow linewidth laser interrogates the cold atoms driving the clock transition. The resulting frequency-dependent atomic state then provides information about the frequency offset of the laser with respect to the transition frequency. Rabi interrogation is the most straightforward protocol using a single π-pulse which yields a frequency dependent Sinc^2

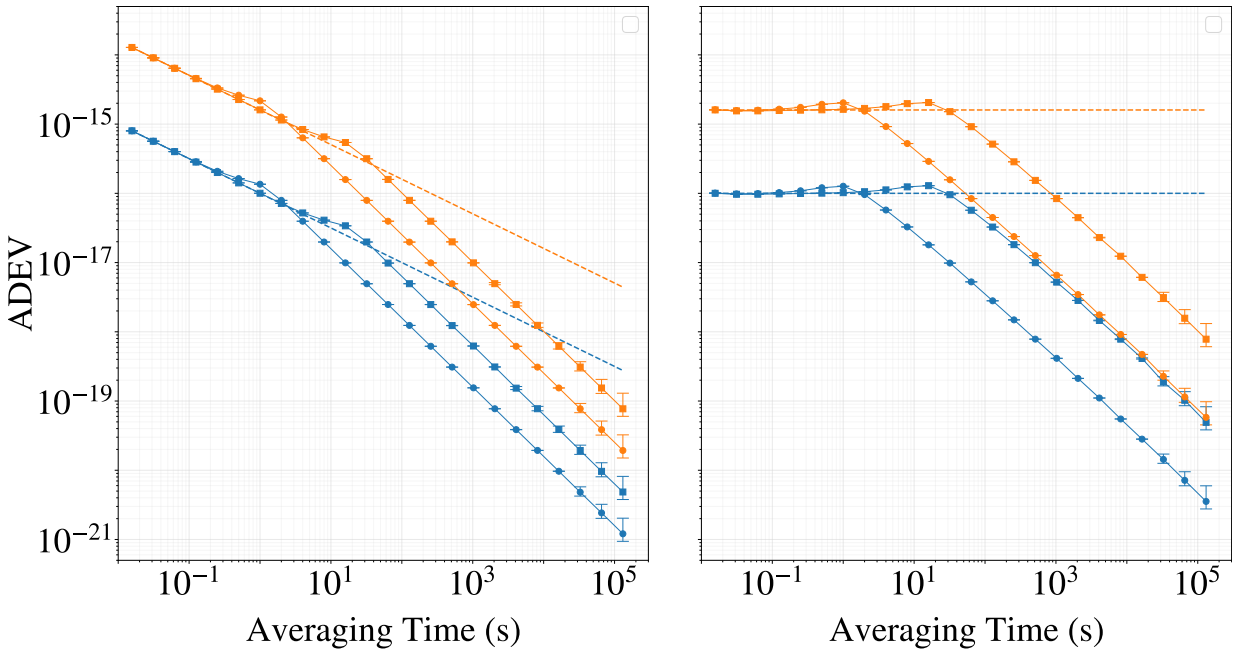

Figure 3.1: **Perfect servo**. Allan variance of the perfect servo. Left: Blue (orange) points are the stability for an oscillator with white noise at the level $1\times10^{-16}/\sqrt{\tau}$ ($1.6\times10^{-15}/\sqrt{\tau}$) with 1 s cycle times and 16 s cycle times for dots and squares respectively. Right: Blue (orange) points are the stability for an oscillator with flicker noise at the level 1×10^{-16} (1.6×10^{-15}) with 1 s cycle times and 16 s cycle times for dots and squares respectively.

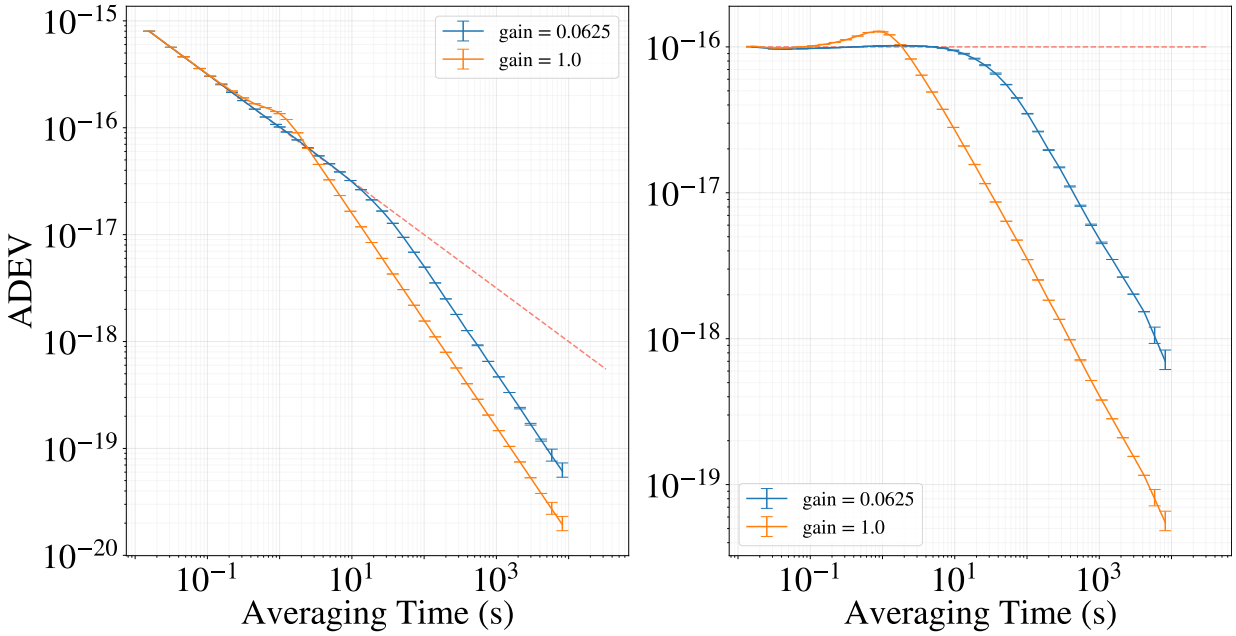

Figure 3.2: **Perfect servo with different gain**. Allan variance of the perfect servo. Left: white noise at the level $1 \times 10^{-16}/\sqrt{\tau}$ corrected by perfect servos with gains of 1 and 1/16. Right: flicker noise at the level 1×10^{-16} corrected by perfect servos with gains of 1 and 1/16.

excitation function [92]. Ramsey interrogations use two short $\frac{\pi}{2}$-pulses separated by a dark time. The first pulse drives the atoms in a superposition where the two states interfere depending on the phase of the laser that accumulates over the interrogation time relative to the phase of the atoms. The laser is detuned by half the linewidth to probe where the lineshape has maximal gradient. After the interrogation, fluorescence readout is used to measure an atomic excitation fraction which is mapped to the frequency offset of the laser using the discriminator determined from the interrogation. Two measurements of excitation fraction are normally used for a frequency estimate where the discriminator has opposite signs either by inverting the lineshape through a phase change in the second pulse or by detuning the probe to regions of the lineshape where the discriminators are opposite due to symmetry.

A theoretical model of the servo action shows that the long-term instability ADEV of the steered laser is given by the ADEV of the frequency errors in the servo [71] which remain after it has corrected the laser noise as in the perfect servo.

$$\sigma_y^2(\tau) = \frac{1}{\nu_0^2 D^2}\sigma_\eta^2(\tau) \tag{3.4}$$

All the effects considered here which are adding noise in the servo are modelled as white noise. This means that the errors are sampled from a normal probability distribution with some variance V_η and the Allan variance is of the form $\sigma_\eta^2(\tau) = V_\eta^2/N_c$ decreasing with the number of correction cycles included in the averaging, $N_c = \tau/T_c$, where T_c is the duration of one cycle, i.e. the time between consecutive corrections. Thus, the instability is determined from the errors in the measurement as

$$\sigma_y^2(\tau) = \frac{1}{\nu_0^2 D^2} V_\eta \frac{T_c}{\tau} \tag{3.5}$$

The result implies that for noise with a variance of errors that does not change with cycle time, the instability is usually worse if the cycle time is longer since it takes more time to average the same number of noisy corrections. The discriminator, however, generally increases with probe time as the spectroscopic line becomes narrower, so actually this reduces the variance by T_i^2/T_c, where T_i is the interaction time and the cycle time $T_c = T_i + T_d$ might also include dead time. Moreover, V_η usually depends on the probe time but the exact form depends on the details of the noise. The aim of this chapter is to determine the variance of measurement errors for all relevant noise sources and from that to estimate the long term instability of the clock.

3.1 Sources of clock instability

The indirect estimation of frequency in the atomic servo is a series of transducers each with the potential to introduce errors. Firstly, the fluorescence measurement which determines the excitation fraction is affected by detection noise from imaging the atoms for counting, such as photon shot noise and background noise. By having enough power in the

imaging beam, and an easily achievable number of atoms, however, this can be reduced to a negligible level [39]. Nonetheless, the excitation fraction itself is an imperfect estimate of the excited state amplitude due to randomness in the projection of the wavefunction. Moreover, even the excitation amplitude can be an imperfect estimate of the differential phase accumulated during the atom-light interaction due to ambiguity attributed to the periodicity of the Bloch vector evolution for large offsets leading to the so-called coherence time limit (CTL). Finally, the frequency offset that the atomic state is sensitive to in the atom-light interaction is not exactly the frequency offset of the laser during the servo cycle because of non-uniform sensitivity leading to the Dick effect. We will describe each of the main sources of errors next excluding only detection noise as it is usually significantly lower than the others and because it can be decoupled from them.

3.1.1 Quantum projection noise

The fluorescence measurement causes collapse of the wavefunction such that the fraction of atoms that are detected in the excited clock state has a certain probability distribution [57]. The normalised excited state amplitude determines the mean of the distribution $F_0 = |a_e|^2$ and the number of atoms in the ensemble determines the variance of the distribution $F_0(1 - F_0)/N_{at}$. Using this in equation 3.5 leads to the following instability.

$$\sigma_y^2(\tau) = \frac{1}{\nu_0^2 D^2} \frac{F_0(1 - F_0)}{N_{at}} \frac{T_c}{\tau} \tag{3.6}$$

The instability is smaller for larger numbers of atoms which reduce the variance of the distribution of the excited state fraction F. Furthermore, the instability also decreases with interrogation time through a stronger discriminator. This can also be understood by looking at the spectroscopic line which is narrowed by longer interrogations so that a given fluctuation in F corresponds to a smaller error in frequency. Finally, the instability increases with cycle time due to lowering the rate of averaging as explained at the beginning of this section.

3.1.2 Coherence time limit

Due to the nature of the excitation response characterised by the atomic excitation line-shape, the excited state amplitude becomes an ambiguous estimator for long interrogation times. The spin evolution is periodic making the spin projection a quasi-periodic function of the laser phase which is a proxy for the laser frequency offset. Thus, the phase estimates are incorrect for values falling outside an invertible range of $\pi/2$ either side of resonance. In longer interrogations the likelihood of the phase evolution to reach higher values increases and thus errors are more frequent. The interaction can be described as a phase diffusion process where the phase starts at zero and randomly evolves as the integral of frequency noise. The laser noise plays an important role in setting the expectation value of the phase evolution for a given interrogation time. In this way, the laser noise level defines

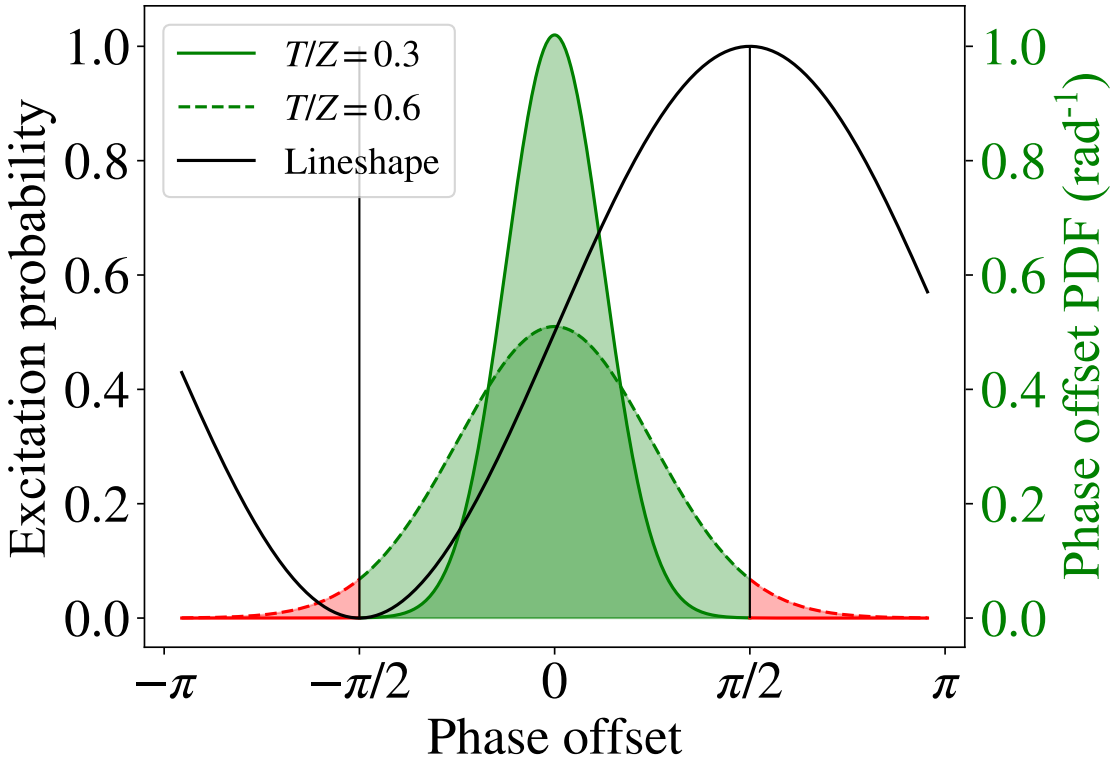

Figure 3.3: **Phase probability distribution functions**. Two cases with different normalised probe times are shown in green, $T/Z = 0.3$ and $T/Z = 0.6$ with solid and dashed lines respectively. The normalised probe time might vary through longer absolute probe time or higher laser noise. The atomic excitation probability is also shown in black.

a timescale for the loss of coherence in phase estimates. Borrowing from Leroux et al [93], the coherence time is defined as the probe time, Z, for which the phase noise standard deviation has a value of

$$\sigma_y(Z)\omega Z = 1 \text{ rad} \tag{3.7}$$

The longer the coherence time is, the narrower the distribution of possible phase offsets will be for a given interrogation time, and thus fewer phase estimation errors will occur in the servo, as shown in Figure 3.3.

It is useful to describe the laser noise through a Gaussian probability distribution of the phase accumulated during an interrogation, $\delta\phi = (\omega_0 - \omega_{LO})t$, rather than an ADEV. Then the coherence of the phase estimates is related to the variance of the phase noise distribution, $V_\phi = \langle \delta\phi^2 \rangle$. This mostly matches the Allan variance of phase noise at the servo cycle time, $\sigma_\phi^2(T_c) = \sigma_y^2(T_c)(\omega T_c)^2$, but with a dependence on the servo gain and possible contributions from servo noise like QPN, which will be discussed in section 3.3. The distribution of phase results in a distribution of errors in the atomic measurement depending also on the excitation lineshape, as illustrated in Figure 3.3. From Leroux et al [93] we see that the phase estimation error for Ramsey interrogation has a variance $V_{CTL} = \sinh V_\phi - V_\phi$ which sets the long-term instability:

$$\sigma_y^2(\tau) = \frac{1}{\nu_0^2 D^2} \left(\sinh V_\phi - V_\phi\right) \frac{T_c}{\tau} \tag{3.8}$$

Like in all types of white noise the instability increases with cycle time as this reduces averaging rate. The dominant factor in the instability is however implicit in the phase variance which depends strongly on interrogation time. This sets a coherence limit on the interrogation which is important in determining the limiting stability of a clock.

3.1.3 Dick effect noise

Gaps in the frequency measurement due to time required for preparing the atoms for spectroscopy and non-uniform sensitivity during the atom-light interaction period both result in uneven weighting of the LO frequency noise at different times during the measurement cycle leading to aliasing errors [94, 95]. During each cycle, the evolution of the Bloch vector, $\mathbf{a}(t)$, is governed by the equation

$$\boldsymbol{a}(T_c) = U(T_c, 0)\boldsymbol{a_0}, \tag{3.9}$$

where $\mathbf{a_0} = \mathbf{a}(0)$ and the evolution operator is given by [96]

$$U(T_c, 0) = U_0(T_c, 0) + 2\pi \int_0^{T_c} U_0(T_c, t)\Delta(t) M_\epsilon U_0(t, 0) dt \tag{3.10}$$

Here, U_0 is the evolution operator for a probe that is on resonance and depends on the chosen pulse sequence applied during the interrogation, while $\Delta(t)M_\epsilon$ represents a perturbation of the evolution operator due to small frequency offsets $\Delta(t)$. The second term therefore reflects changes in the Bloch vector evolution due to laser frequency offsets. We are interested in the z-component of the Bloch vector, $a_3 = (0, 0, 1)\boldsymbol{a}$, which becomes

$$a_3(T_c) = a_{3,0}(T_c) + 2\pi \int_0^{T_c} g(t)\Delta(t), \tag{3.11}$$

where $a_{3,0}(T_c)$ is the z-component that the Bloch vector would have at the end of a sequence where the laser frequency is perfectly resonant, and the sensitivity function is defined as

$$g(t) = (0, 0, 1)U_0(T_c, t)M_\epsilon U_0(t, 0)\boldsymbol{a_0} \tag{3.12}$$

The frequency offset, $\Delta(t)$, represents a difference between the frequency of the laser and of the atomic transition including any external perturbations that shift the energy levels. The fact that the atomic excitation amplitude after the interaction with the laser is sensitive to the difference between laser and clock transition means that we can treat laser offsets and shifts to the transition equally. This will be relevant later when we consider such shifts since it means we can use the same approach to estimate their instability contribution. Ignoring shifts for now, we find that the atomic excitation fraction at the

end of the interrogation will be different to the mean value, i.e. the value obtained in the absence of offsets, by an amount

$$\delta F = \pi \int_0^{T_c} g(t)\Delta(t)dt, \tag{3.13}$$

which is the equation normally used to introduce the sensitivity function. In converting between a_3 and F we lose a factor of 2 due to the fact that the former takes values between -1 and 1 while the latter takes values between 0 and 1.

To calculate the sensitivity function one can solve equation 3.12 analytically. For the purposes of this work, specifically in simulations, we estimate it numerically by calculating the Bloch vector evolution with a small frequency offset at different points during the probing cycle. In Rabi interrogation a single π pulse drives the pseudo-spin vector Bloch vector by rotating it around an axis which depends on the laser detuning, resulting in a sensitivity that varies as a sinusoidal function over the $[0, \pi]$ interval. A Ramsey probe uses two short $\frac{\pi}{2}$ pulses separated by a pause in the laser light and gives a more uniform sensitivity because after the first pulse the spin vector sits on the equator of the Bloch sphere and rotates at the resonant frequency given by the energy level difference. In the rotating wave frame, frequency offsets build up a phase in the equatorial plane. The second $\frac{\pi}{2}$ pulse projects the phase onto the z axis of the Bloch sphere so the differential phase between laser and atoms leads to an atomic population imbalance in the readout.

The resulting instability from this uneven sampling of laser noise is the convolution of the sensitivity function with the noise spectrum of the laser, S_ν, at frequencies that are multiples of the inverse of the cycle time [71].

$$\sigma_y^2(\tau) = \frac{1}{\nu_0^2 D^2}\frac{1}{\tau}\pi^2 \sum_{m\neq 0} \left|\hat{g}\left(\frac{m}{T_c}\right)\right|^2 S_\nu\left(\frac{m}{T_c}\right) \tag{3.14}$$

A simple analytical result can be obtained for a white noise dominated clock laser, in the idealised case of Ramsey spectroscopy with negligibly short $\pi/2$ pulses, dark time T, and dead time T_d. In this case, the instability evaluates to the following expression:

$$\sigma_y^2(\tau) = \sigma_{LO}^2(\tau)\frac{T_d}{T} \tag{3.15}$$

Like in all other white noise types, the cycle time determines the averaging rate. This has a negative effect on instability by bringing the $\frac{m}{T_c}$ frequencies closer together. However, sensitivity changes are more complex and dominate, so the behaviour is different if the cycle time is increased by extending the probe time or the dead time. We illustrate this in Figure 3.4 where we plot the numerically evaluated Allan deviation (square root of equation 3.14) against probe time for a few dead time values. For clocks using Ramsey spectroscopy, the instability decreases monotonically, is higher with longer dead times, and asymptotes to the Rabi line as the dark times get smaller and the sensitivity approaches that of two $\pi/2$ pulses side-by-side. As we extend the probe time, the instability goes down, faster in

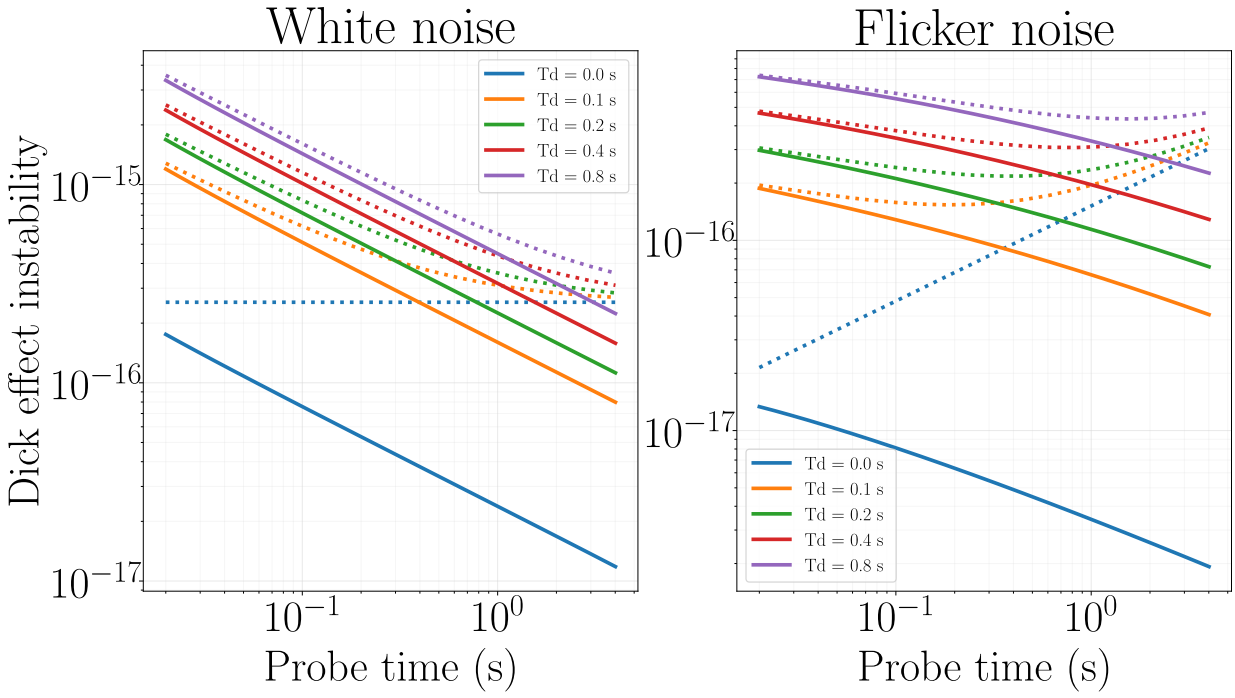

Figure 3.4: **Dick effect instability**. Calculated Dick effect instability vs probe time for $1 \times 10^{-16}/\sqrt{\tau}$ white noise (left) and 1×10^{-16} flicker noise (right) respectively, for a range of dead times. The solid lines and dotted lines indicate Ramsey and Rabi interrogation respectively. The Ramsey interrogations comprise two 5 ms $\pi/2$ pulses and varying dark time.

the case of white noise, where the spectrum is uniform, and slightly slower for flicker noise where longer cycle times lead to sampling at the lower frequency end of the noise spectrum which has larger amplitude.

For clocks using Rabi spectroscopy, the instability is still higher with longer dead times, but asymptotes to the zero dead time line at long probe time. Interestingly, however, this line is a constant value in the case of white noise and a $\sqrt{\tau}$ line in the case of flicker noise. Thus, there is a limit to which we can improve the stability by extending the Rabi probe, beyond which the performance does not improve or even starts to degrade. The point at which this happens depends on the dead time, moving to longer probe times for longer dead times. Particularly for flicker noise, the inflection point seems to move as $T_p = 2T_d$. At zero dead time, the best stability in terms of the Dick effect requires the shortest probe times. This is the reason why Ramsey spectroscopy is best suited for zero dead time systems, which will be discussed in the next chapter. These characteristics remain valid for different levels of laser noise the effect of which is just to scale S_ν in equation 3.14 by a constant.

3.2 Simulations for instability model validation

We developed simulations running on Python to investigate the theoretical instability model. Using a Monte Carlo algorithm we calculate the clock servo action on randomly generated frequency data with a probability distribution given by the laser noise and we compare the results from the stochastic equations presented above with the results from the numerical computation. Thus, the simulations are used to test the soundness of our derivations starting from known sources of errors in the servo but their accuracy is given by the inclusion of realistic noise mechanisms.

To simulate the clock operation we first define the interrogation sequence including dead-time for atom cooling and the interrogation protocol, which can be Rabi, Ramsey or any other custom pulse sequence. Based on this we calculate the sensitivity function and the excitation lineshape as a function of laser detuning. Next, we simulate the frequency data using the *allantools* package based on the noise components of the laser to be simulated. This generates frequency data that is random but has the desired ADEV profile. The noise array is then sequenced like in the real clock and for each cycle a weighted mean offset is calculated using the sensitivity function. The frequency offset is mapped to the atomic excitation lineshape to determine the excitation amplitude which is finally converted to an atomic excitation fraction by generating a random value with a probability distribution centred on the excitation probability and with a variance given by the number of atoms probed. After each servo cycle which normally contains two detection cycles to probe two sides of the lineshape with opposite discriminators a correction frequency is calculated according to

$$\nu_{c,n+1} = \nu_{c,n} + g_1 \frac{\epsilon_n}{D} + g_2 \frac{\sum_{k=0}^{n} \epsilon_k}{D} T_c, \tag{3.16}$$

where g_1 and g_2 are the first and second integrator servo gains respectively. The first integrator servo is the conventional servo that we discussed so far and it averages previous measurements to make a frequency correction. The second integrator averages past corrections and may be used to avoid frequency offsets in the clock when the local oscillator is drifting. We restrict the rest of the discussion to cases where the local oscillator is not drifting and we neglect the second integrator.

As mentioned earlier, the accuracy of the simulations rests on the inclusion of realistic noise mechanisms, besides the noise data that represents the laser frequency. We include noise from the Dick effect simply by using the sensitivity function to calculate the offset, meaning that noise which occurs during the dead-time will have a zero weighting and not contribute to the measurement. Phase estimation errors are also intrinsic to the algorithm since only the measured excitation fractions are used to calculate the corrections which accounts for the atomic state propagation. Finally, we include QPN by adding a fluctuation in the measurement of excitation fraction based on a random number generator with Gaussian distribution according to the number of atoms.

Figure 3.5 shows the results from the simulation of a Sr optical lattice clock which operates with a 650 ms cooling stage and a 500 ms Ramsey interrogation. The noise of the clock output matches the noise of the laser on short time scales. At time scales on the

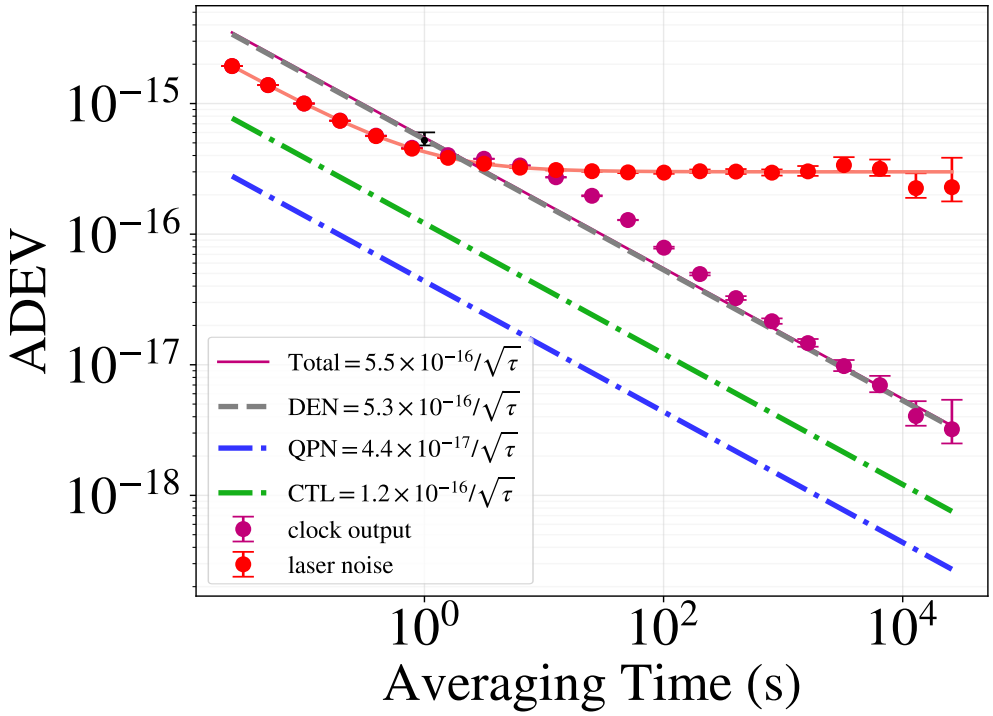

Figure 3.5: **Clock simulation**. Allan plot of the clock servo simulation. Red dots are the Allan deviation of the LO and the red line is the theoretical profile of the LO. The purple dots are the Allan deviation of the steered LO. Dashed lines indicate the theoretical instability contribution for different noise sources. Error bars represent 1σ confidence intervals.

order of the servo cycle (around 2 s) the clock output has a bump due to servo corrections just like in the ideal servo. As expected, at time scales longer than the servo attack time the clock output performs better than the free laser and asymptotes to a white noise line.

To check the model, we compare the instability predicted by the total contribution from all noise mechanisms with the long-term instability inferred from the ADEV of the simulation. The long-term instability is determined by the asymptotic behaviour of the ADEV. The ADEV initially averages down with a rate approaching $1/\tau$ as in the case of the perfect servo. Eventually, the ADEV asymptotes to a $1/\sqrt{\tau}$ white noise line as the laser noise diminishes leaving the measurement errors. We define this line as the long-term instability of the clock and compare to the quadrature sum of modelled instability contributions. As established theoretically, the long-term instability is set by the frequency estimation errors, and differently to the perfect servo, the servo attack time controlled by the servo gain only determines how fast the instability limit is reached; however the choice of gain does have an impact on the phase variance which can change the CTL contribution to the white noise limit, as will be discussed in the next section.

3.3 Coherence time limit with realistic spectroscopy

As mentioned previously, we predict the CTL contribution to instability from the distribution of laser phase noise. Estimating the variance of that distribution is thus a crucial step in determining CTL instability. The phase variance is simply the frequency offset variance multiplied by $(2\pi T_i)^2$. The Allan variance is different from the standard variance since it gives the variability between two samples rather than the variability of a sample from the mean. However, for a LO locked to a frequency reference the frequency is constantly steered which means that the frequency jump from one cycle to the next will be approximately equal to the frequency jump from the mean. For an AVAR with power law $\sigma_y^2(T) = \sigma T^\mu$ the phase variance then scales as

$$V_\phi \propto \sigma_y^2(T) \left(\omega T\right)^2 = T^{\mu+2} \left(\omega\sigma\right)^2 = \left(T/Z\right)^{\mu+2} \tag{3.17}$$

where we used the coherence time of the laser $Z = (\omega\sigma)^{-2/(\mu+2)}$ to normalise the interrogation time T. Writing Z in this form agrees with the definition in equation 3.7. This confirms that the phase variance increases with the coherence-time-normalised probe time, and the exponent of that relation depends on the type of noise present in the LO.

3.3.1 Atomic phase evolution

The aim of the atomic interrogation is to determine the offset between the noisy laser frequency and the atomic transition frequency by mapping frequency offsets to the atomic state evolution. In the ideal Ramsey case with no external perturbations, the atoms are instantly driven into the fully mixed state $|\psi\rangle = \frac{1}{\sqrt{2}}\left(|g\rangle + e^{-i\phi}|e\rangle\right)$ and the atomic phase $\phi = \omega_0 t$ evolves with the resonance frequency $\omega_0 = (E_e - E_g)/\hbar$. In the rotating frame of the laser, the atomic phase is the differential phase between the laser and resonance $\delta\phi = (\omega_{LO} - \omega_0)t = \delta\omega t$. This differential phase that accumulates by the end of the interrogation is instantly mapped onto the z axis of the Bloch sphere by the second pulse to yield a population difference read by the following excitation fraction measurement. The coherence time limit arises from errors in the projection when the phase is larger than $\pi/2$ in magnitude.

However, in other less ideal cases there may be dead-time in the cycle and the sensitivity may not be perfectly flat and maximal during the interrogation, as is the case during the $\pi/2$ pulses of the Ramsey protocol or when applying dynamical decoupling methods (discussed later in section 4.1). The phase that accumulates in the rotating frame of the laser frequency is then not equal to the differential phase for the duration of the cycle. During the dead time the phase will not grow at all while during the interrogation it will evolve with the rate set by the laser frequency scaled by the sensitivity function. This means that the phase will be different to when the sensitivity is uniform and so the CTL errors will also differ. The relevant phase to use in this case is not the true differential phase based on the actual laser frequency offset but rather the differential phase based on the sensitivity-weighted frequency offset.

Finally, in cases where external fields perturb the atomic transition frequency, such as those discussed in section 3.5.1, the phase that determines the CTL instability should also include those clock shifts. To account for them, we determine the phase variance for each effect and type of noise individually provided they are statistically uncorrelated, and then add the resulting variances to obtain the total variance.

3.3.2 The effect of servo gain

Considering for now a perfect servo we perform a range of clock operation simulations with different probe times and look at the phase variance. We determine that a fitting function

$$V_\phi = k\,(T/Z)^{\mu+2} \tag{3.18}$$

represents the data well and the coefficient k does not depend on the noise level, but it does depend on the noise type and the servo gain. Figure 3.6 shows the coefficients determined from fitting this function to the simulations for a range of servo gain values in the case of white noise and flicker noise respectively. Thus, the phase variance for a given normalised interrogation time appears to be higher than the Allan variance by a factor depending on the time correlation of the noise and on the ability of the servo to remove those correlations through an appropriate choice of servo gain. Leroux et al. ([93]) present equations for the coefficients for white noise

$$k_w(g) = \frac{2}{2-g} \tag{3.19}$$

and for flicker noise

$$k_f(g) = \frac{1.6 + 0.4g - \ln 4 \ln g}{2-g} \tag{3.20}$$

which we plot over the simulation data (Figure 3.6) and see a good fit.

The best case is white noise with a servo gain approaching 0, i.e. no corrections needed, with a pre-factor of 1 indicating that the Allan variance and the standard variance are equal. Flicker noise needs the action of the servo to remove time correlations and even at the optimal gain value around 0.6 the phase variance is larger than for white noise, with a pre-factor close to 1.8.

The next step to try is an ideal atomic servo, i.e one with uniform sensitivity and negligible QPN. This would differ from the perfect servo through the atomic state evolution which leads to the periodic lineshape for atomic excitation probability. The excitation fraction is converted back into a frequency offset estimate by assuming a linear discriminator like in the operation of the real clock. In this case the servo feeds back the phase estimation errors along with the corrections which could have an impact on the phase variance. It turns out that if the linear discriminator used in the conversion is chosen to be the maximum gradient of the lineshape then the phase variance has the same gain dependence as the perfect servo. If the scaling is different by a factor χ, this effectively changes the gain from g to $g\chi$ and the equations for the coefficients can still be used.

The cases discussed here contain a single source of noise. However, in realistic situations, there are often multiple sources contributing independently to the LO noise profile.

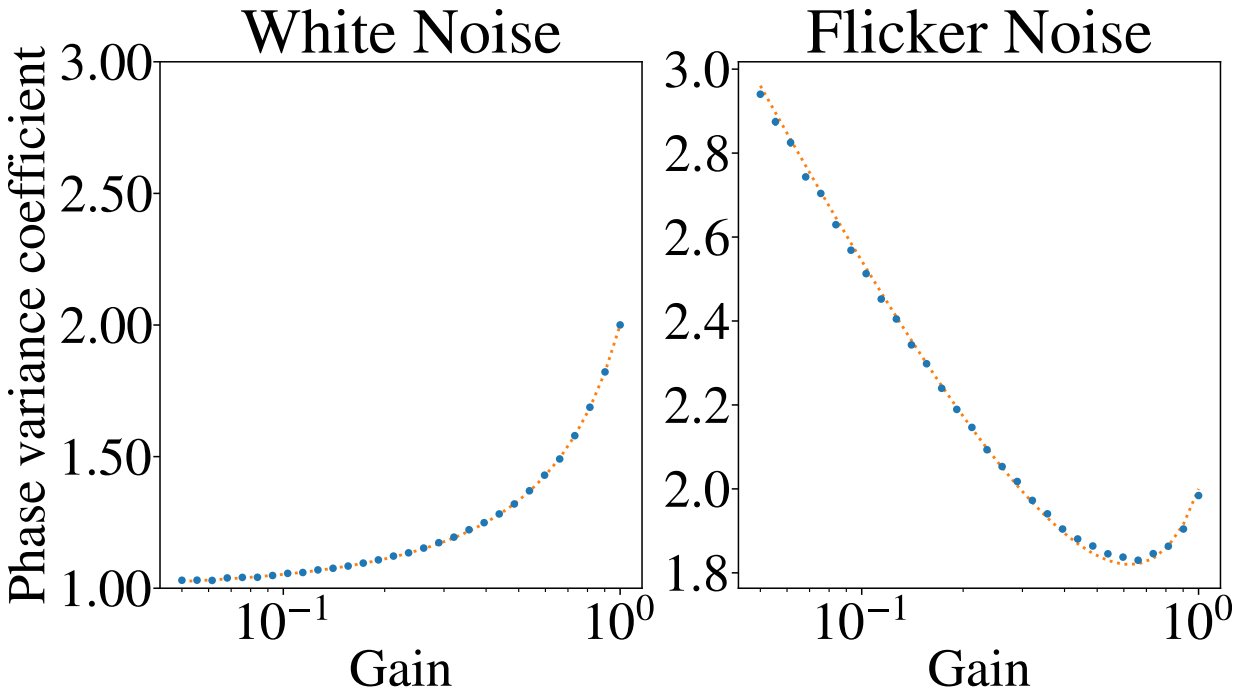

Figure 3.6: **Phase variance gain factor**. Phase variance coefficients vs. servo gain. The proportionality coefficients between the phase variance and the Allan variance at one cycle time are plotted for a range of servo gain values for white noise (left) and flicker noise (right). The dashed lines show the values obtained from equations 3.19 and 3.20.

Because the processes are independent, one can simply use the additivity of variance and calculate the phase variance for each one separately adding them together to obtain the total variance. Although not shown here, this has been verified by running the simulations based on frequency data with a mixture of white and flicker noise.

3.3.3 The effect of QPN

In the real clock, the imperfect servo feeds back additional noise to the LO which can change the phase noise affecting the phase variance. At low atom numbers and short interrogation time the QPN can be larger than the laser noise meaning that after a few clock cycles the LO will be infused with additional white noise from the corrections. To work out the contribution of this additional noise, assume for the moment that it is significantly larger than the laser noise. We start from the atomic excitation fraction difference from the mean, $\delta F_n = F_n - F_0$, using the equation

$$\delta F = \delta P_n + \delta F_{QPN}, \tag{3.21}$$

where δP_n is the difference in excitation probability from the mean $P_0 = 1/2$ and δF_{QPN} is a random variable with mean 0 and variance $\langle \delta F_{QPN}^2 \rangle = \frac{F_0(1-F_0)}{N_{at}}$. Assuming a Ramsey

interrogation of duration T_i, the probability becomes

$$\delta P_n = \frac{1 + \sin\left(\delta\nu_n 2\pi T_i\right)}{2} - \frac{1}{2} \approx \delta\nu_n \pi T_i, \tag{3.22}$$

where the last approximation holds under the condition that the frequency remains within the linear region of the lineshape, which is satisfied for short enough interrogation times. Then we can write the servo equation 3.16 (using only the first integrator) as

$$\delta\nu_{n+1} = \delta\nu_n \left(1 - g_1 \frac{\pi T_i}{D}\right) - g_1 \frac{\delta F_{QPN}}{D}. \tag{3.23}$$

which can be simplified by equating the discriminator to the maximum gradient of the lineshape $\frac{dP}{d\nu}|_{P=0.5} = \pi T_i$ to get

$$\delta\nu_{n+1} = \delta\nu_n \left(1 - g_1\right) - \frac{g_1}{\pi T_i} \delta F_{QPN}. \tag{3.24}$$

Now we can use this recursive equation to find the variance of the frequency

$$\left\langle \delta\nu^2 \right\rangle = \left(1 - g_1\right)^2 \left\langle \delta\nu^2 \right\rangle + \left(\frac{g_1}{\pi T_i}\right)^2 \left\langle \delta F_{QPN}^2 \right\rangle - \frac{g_1}{\pi T_i} \left(1 - g_1\right) \left\langle \delta\nu \delta F_{QPN} \right\rangle \tag{3.25}$$

The last term is zero since both the frequency and the QPN fluctuations have a mean of zero and are statistically uncorrelated. Thus, we arrive at the frequency corrections variance

$$V_\nu = \frac{\left(g_1/\pi T_i\right)^2}{1 - \left(1 - g_1\right)^2} \left\langle \left(\delta F_{QPN}\right)^2 \right\rangle = \frac{g_1/\left(\pi T_i\right)^2}{2 - g_1} \frac{F_0(1 - F_0)}{N_{at}}, \tag{3.26}$$

or in terms of phase

$$V_\phi = \frac{4 g_1}{2 - g_1} \frac{F_0(1 - F_0)}{N_{at}}, \tag{3.27}$$

Thus, in the short probe time regime the phase variance is a constant gain-dependent term. Since this white noise is uncorrelated with the laser noise, this independent QPN contribution to phase variance remains valid at longer probe times and we add it to the laser noise contributions. Figure 3.7 shows the results from simulations compared with the model. For short probe times, the QPN contribution is dominant, and the phase variance reaches a time-independent value. At long probe times, the phase variance follows the laser noise AVAR and at intermediate times is just the sum of the two.

It might be interesting to consider the case when multiple measurements are made before the correction is applied. For the QPN contribution, one would expect that averaging a few measurements reduces the variance. Indeed it can be shown that the variance of the corrections in equation 3.27 when averaging a number M of consecutive measurements has the reduced value in equation 3.28. However, as will be discussed in the next section, this also changes the feedback to the laser noise, which has the opposite effect.

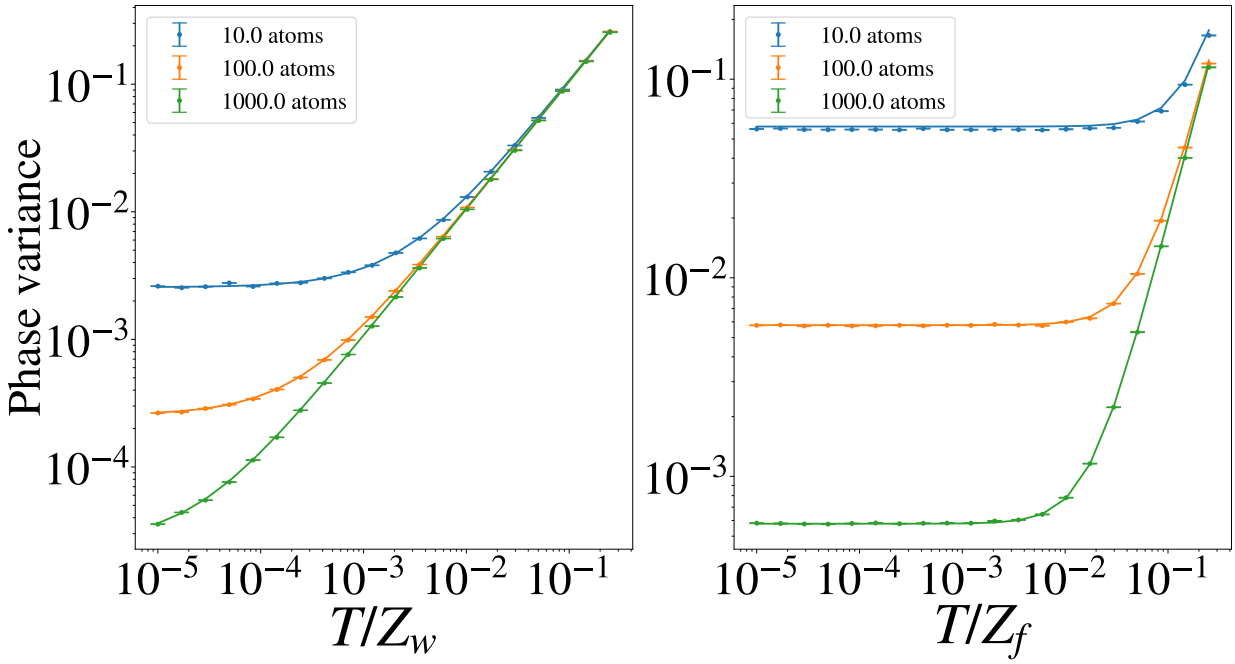

Figure 3.7: **QPN effect on phase variance**. Phase variance from simulations for an atomic servo with no dead-time. The phase variance observed in simulations for a range of measurement times normalised by the coherence time for a white noise LO at $1 \times 10^{-16}/\sqrt{\tau}$ (left) and for a flicker noise LO at 1×10^{-16} (right) repeated using different numbers of atoms. The lines are theoretical values calculated as the sum of equations 3.18 and 3.27.

$$V_\phi = \frac{4g_1}{2 - g_1/M} \frac{F_0(1 - F_0)}{N_{at}} \tag{3.28}$$

3.3.4 The effect of servo rate

Since the phase variance depends so much on the quality of the servo including the choice of servo gain and sources of noise it is reasonable to assume that it also depends on the rate at which corrections are applied, which for a given probe time can change due to dead-time and the protocol used to apply the corrections. The most basic protocol would be a single frequency measurement followed by a correction. However, in most cases this is not a reliable method since it is susceptible to line broadening or shifting so optical lattice clocks use two measurements to probe a transition line with a measurement on each side of the line averaging the results to get an error signal as explained at the start of the section. Furthermore, in the case of single ion clocks several measurements need to be made on each side of the line to obtain an excitation fraction. This can significantly extend the duration of the servo cycle. So it is useful to investigate how the phase variance changes when a correction uses multiple measurements.

Simulations indicate an overall increase in the phase variance for flicker noise when multiple shots are used and a reduction for white noise, as shown in Figure 3.9. There are

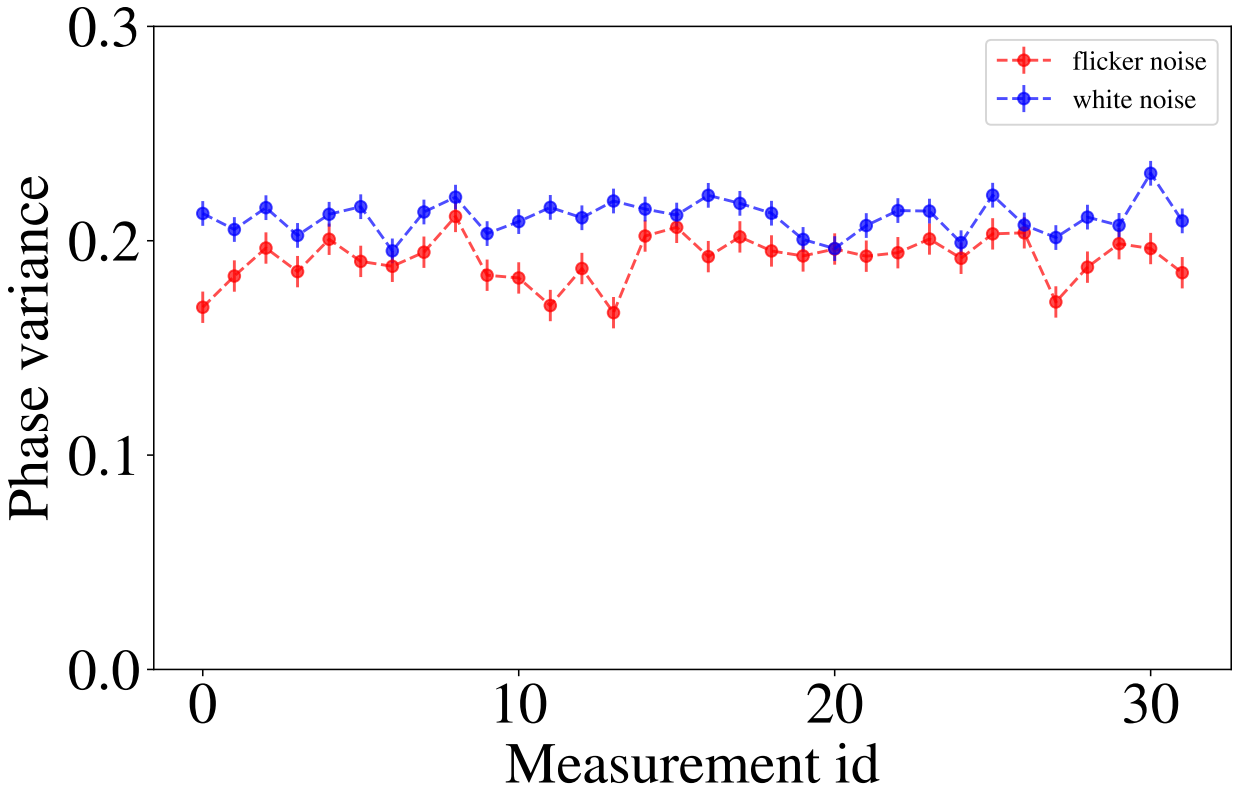

Figure 3.8: **Phase noise in servos with multiple measurements**. Phase variance estimated from simulations of the clock servo using randomly generated frequency data following a white noise distribution or a flicker noise distribution. The servo pattern consists of 32 consecutive measurements followed by a single frequency correction. For each measurement number in the cycle, the phase variance was estimated from the distribution of phase offsets in the corresponding measurements over the whole simulation. Error bars represent the uncertainty in fitting the phase distribution.

a few effects that could contribute to this. First, the frequency is not steered before each measurement but only before the first measurement during a servo cycle. This might lead to a frequency offset that on average gets progressively larger during the servo cycle, at least in the case of flicker noise. However, simulations indicate that this does not happen. Figure 3.8 shows the phase variance as a function of the measurement number in a servo using 32 consecutive measurements per correction. The variances have been calculated by computing frequency measurements and servo corrections and grouping the phase data according to the measurement number in each cycle. As expected, if the laser has a white noise profile, the variance does not get progressively higher during the cycle. However, this remains true even for flicker noise. Thus, this cannot serve as an explanation for the increased phase variance

Another possible factor is the effective gain reduction performed by taking multiple measurements. If M measurements are averaged then the contribution of each measurement to a correction is reduced by M, which is equivalent to using a gain smaller by a factor M. Adjusting the equations accordingly gives a better match for small gains but not as good for

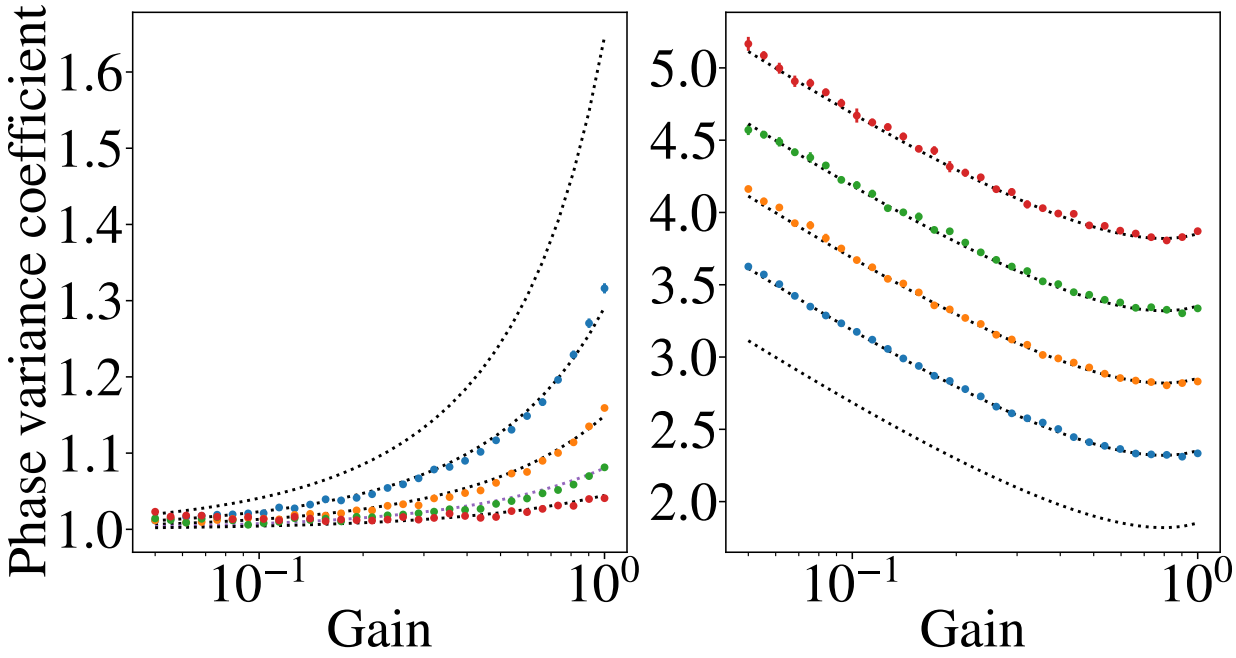

Figure 3.9: **Phase variance and correction rate**. Phase variance coefficients vs. servo gain and number of measurements per correction. The proportionality coefficients between the phase variance and the Allan variance at one cycle time are plotted for a range of servo gain values for white noise (left) and flicker noise (right). Servos using 2, 4, 8, and 16 measurements are in blue, orange, green and red circles. The dashed lines show the values obtained from empirical relations 3.29 and 3.30

gain values closer to 1. Lastly, because the rate at which corrections are applied decreases, the attack time of the servo increases which moves the servo bump in the instability. It is not straightforward to predict how the phase variance would be affected in the multiple measurements servo based on these considerations. However, from simulations, we arrived at the following empirical relations which we plot in Figure 3.9:

$$k_w(g, M) = \frac{2}{2 - g/M^{0.8}} \tag{3.29}$$

$$k_f(g, M) = k_f(g, 1) + \frac{1}{2}\log_2 M \tag{3.30}$$

So, in the case of white noise the effect of multiple measurements on the phase variance coefficient is equivalent to a reduction of the gain, while in the case of flicker noise the effect is a gain-independent offset that scales with the logarithm of the number of measurements taken for each correction.

Besides the effect on the phase variance, simulations indicate that the CTL calculation is also affected by servos using multiple measurements per correction. It appears that even if the correct phase variance is used, the CTL model underestimates the instability. This was verified by running simulations where the QPN was removed leaving only CTL errors. Then, looking at the resulting instability in the simulations, a correction factor can be

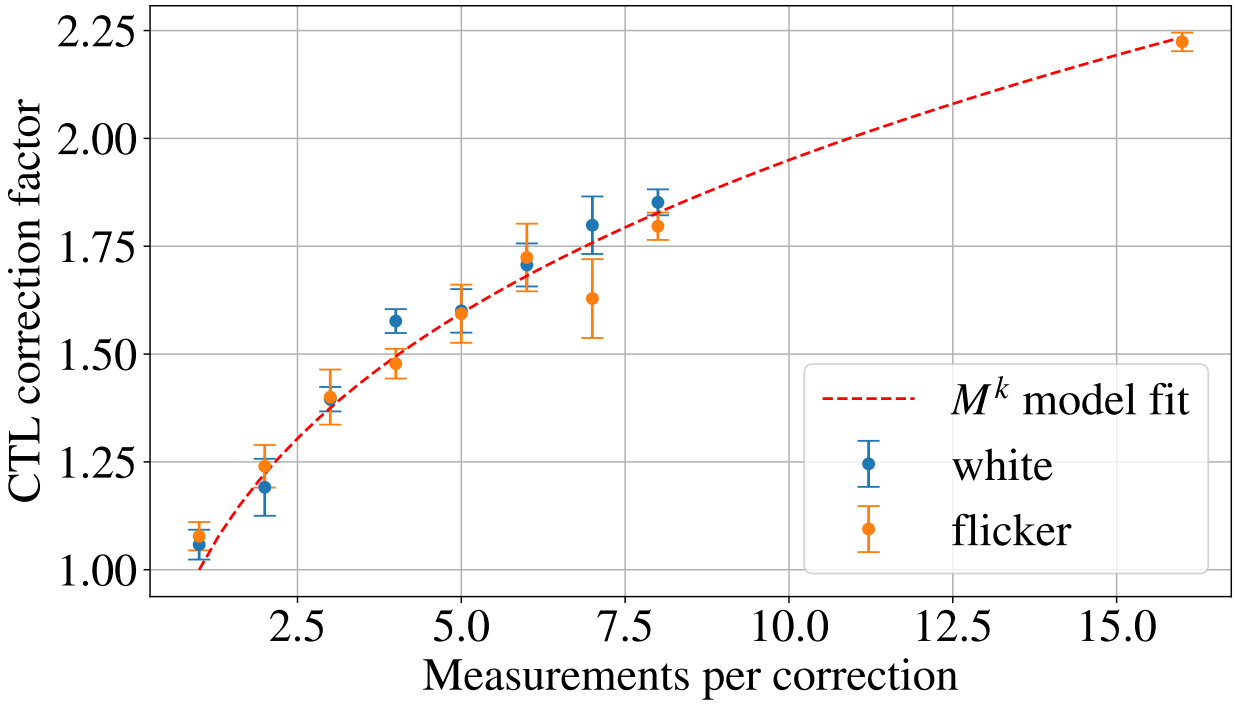

Figure 3.10: **CTL correction factor** for servos where multiple measurements are used for each correction. Error bars represent variance in repeats with different gains: 0.8, 0.9, 1.0.

fitted to the CTL to match the instability. Figure 3.10 shows the dependence of the CTL instability correction factor on M revealing a relation

$$\frac{\sigma_{CTL}(\tau, M)}{\sigma_{CTL}(\tau, 0)} = M^k, \tag{3.31}$$

where k = 0.29(1), and $\sigma_{CTL}(\tau, 0)$ is the standard CTL model from equation 3.8. The fitting does not change significantly for different gains and between flicker noise and white noise dominated LOs.

3.3.5 The effect of dead time

When the measurement cycle includes dead-time, the phase variance is affected in two ways. First, the servo cycle time increases by a factor $M = (T_p + T_d)/T_p$ which has the effect that was just discussed. And second, the additional noise on the corrections due to the Dick effect is fed back into the local oscillator and contributes to subsequent phase measurements. Here also predictions of the effect on phase variance are not straightforward. When simulating such cases we use a semi-analytical approach where the CTL is calculated using equation 3.8 while the phase variance is estimated from the simulations rather than predicted analytically.

Although only applicable near the optimal probe time, a model based on the indepen-

dent phase diffusion during dead times was proposed in [97] by assigning a phase variance solely to dead time and fluctuations therein. In Figure 3.11, the phase variance estimated through simulations is plotted for servos which use a single measurement for each correction but contain dead time. Differently to the dead time phase diffusion model, no effect on the phase distribution for white noise can be observed in the simulations. For flicker noise, a higher phase variance is observed when dead time is introduced, but the effect diminishes at long probe times as the duty cycle approaches 100%.

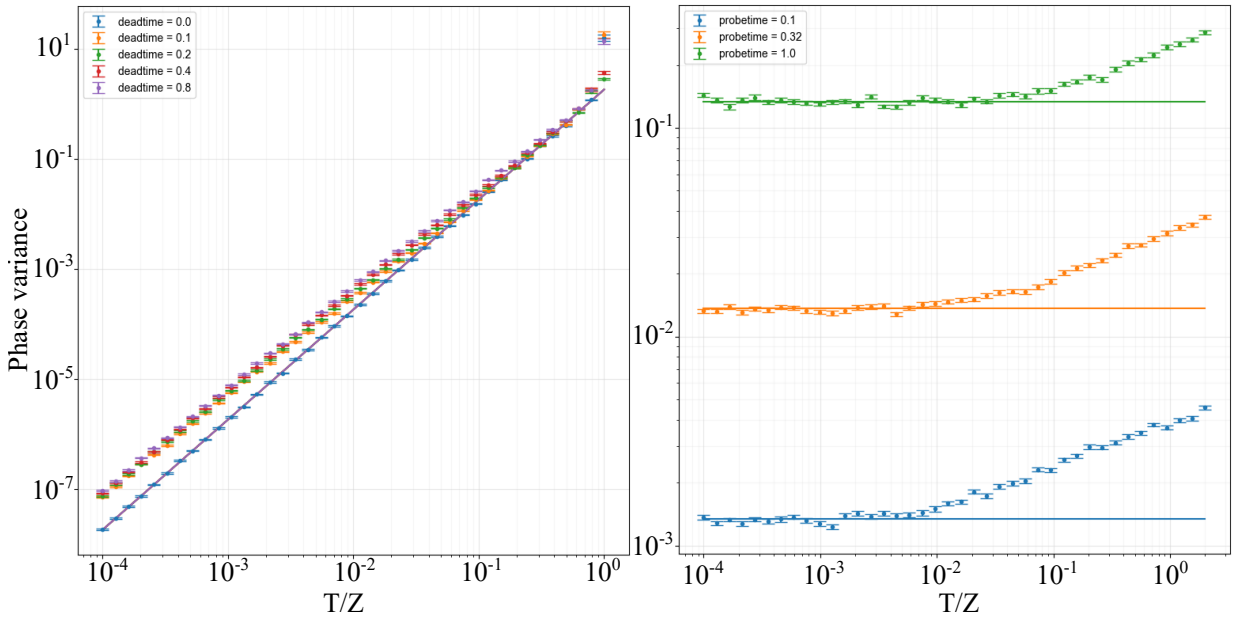

Figure 3.11: **Dead time effects on the phase variance.** Left: Phase variance vs probe time for a range of dead times. Right: Phase variance vs dead time for a range of probe times

3.4 Optimal probe time

The three effects that contribute to errors in the frequency estimation have limiting instabilities that scale differently with probe time. As explained at the start of the section, the leading effect of probe time is to reduce the impact of the measurement errors through making the line narrower as a leading contribution, with a secondary effect of increasing the instability through reducing the rate of averaging of the errors. Looking at the errors themselves, we see that the errors from QPN have a variance which only depends on the number of atoms probed in each measurement, so the time stability gains from extending probe time persist. The Dick effect errors have an additional advantage as longer probe times increase the duty cycle improving the sensitivity function and reducing the weight of the dead-time. The CTL errors on the other hand increase with the probe time so as to roughly cancel the narrowing of the line, leading to an increase in instability with probe time. The opposite scaling for CTL from QPN and the Dick effect means that at short probe times the instability can be improved by extending the probe time but at some point

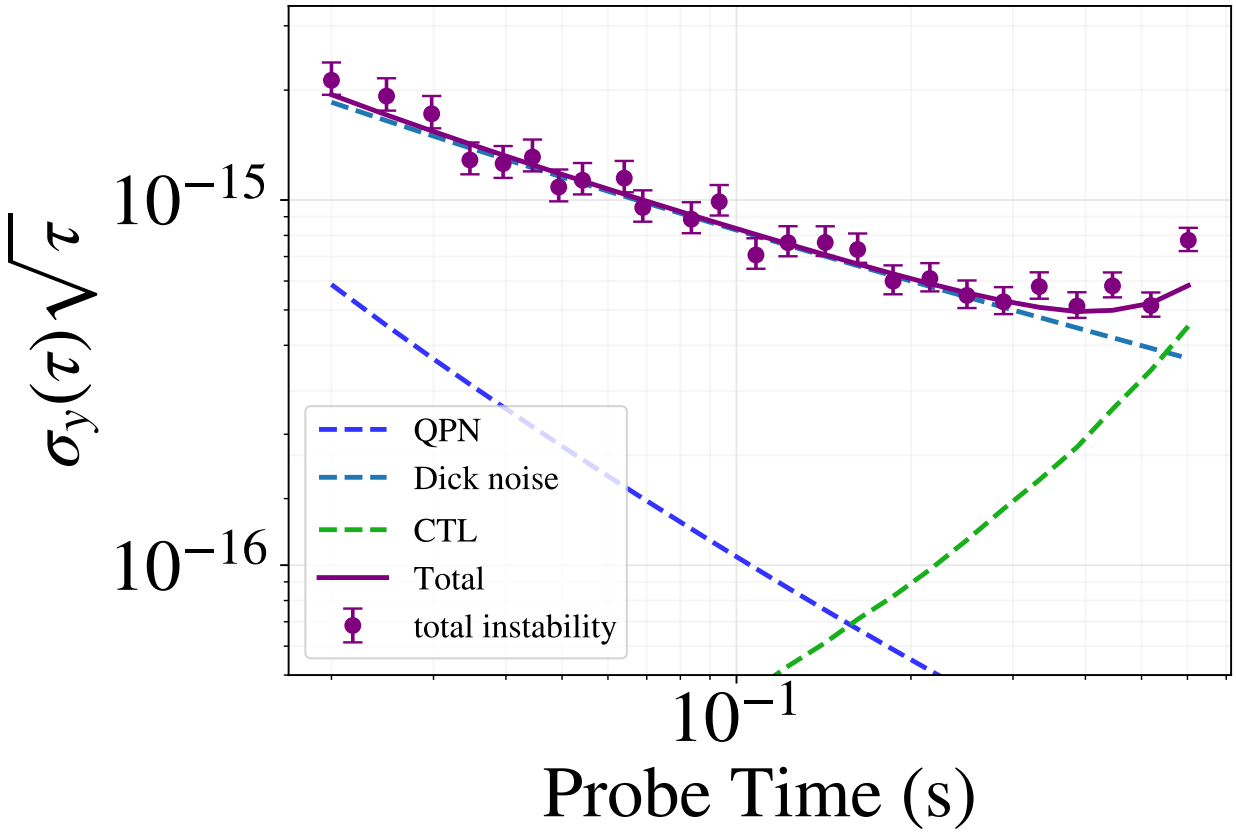

Figure 3.12: **Probe time optimisation**. Instability limit vs. probe time. The instability asymptotes from the simulations are plotted in purple. Dashed lines show individual contributions from different noise sources predicted theoretically.

the CTL takes over. Thus, there is an optimal point where the instability is minimised, as noted in [43].

To observe this, we run a range of simulations with different probe times and plot the long-term instability limit in each case. In all cases, the dead-time is kept at 650 ms, the number of atoms is 1000 and the frequency data is generated based on a local oscillator with a white noise contribution of 1e-16 and a flicker floor of 3e-16. A crude estimate of the optimal probe time is the point at which the Dick effect contribution is equal to the CTL contribution since beyond this point the instability is largely determined by CTL and thus only increases. However, due to the steep scaling with probe time of the CTL instability, usually steeper than that for the Dick effect or for QPN, minimal instability is reached at a slightly shorter probe time.

3.5 Stability of clock shifts

We have discussed how white noise on the frequency measurements remains in the clock output and determines its long-term instability. This noise comes from imperfections in the measurement of the local oscillator frequency offset from the frequency of the atomic

transition. However, if the frequency of the transition itself is shifted by environmental perturbations, the measurements will be affected and so will the clock stability. Spectroscopy measurements cannot distinguish between laser offsets and atomic transition shifts and because the feedback architecture is set up to lock to the clock transition, the clock output would blindly follow these shifts. Characterisation and management of these shifts is possibly through temperature measurements, magnetic field estimation and so on, but with non-zero uncertainty. The uncertainties from all the effects are summarised in uncertainty budgets and represent the long term uncertainty of the clock after instability-related uncertainties become negligible, so are considered when talking about accuracy rather than stability. However, one effect in particular is directly relevant to stability because of the way it is measured and corrected.

3.5.1 Linear Zeeman shifts

Shifts due to external magnetic fields can be suppressed to some extent. The Zeeman effect has opposite sign for symmetric transitions between sublevels with different m_F in fermionic Strontium (This is discussed in more detail in Chapter 5, see Figure 5.6). Thus, the shift cancels in the average of the two lines. The standard detection protocol for the atomic excitation fraction does not permit simultaneous measurements of two different transitions. So, instead, we alternate between driving one transition and driving the other one. The shift then cancels only to the extent that it does not vary between the measurement of one line and the measurement of the other. Any changes on that timescale would result in measurement noise just like all the other effects discussed so far, and would contribute to the long-term instability of the clock. This section presents a statistical model for the amplitude of the effect in terms of the magnetic field noise and measurement protocol.

We compute the clock correction as the mean of the measurements of the two lines. Using equation 3.3 (and ignoring other sources of noise for now) we can write the error signals for the two lines as

$$\epsilon_n^- = D\frac{\Delta_{2n}^L + \Delta_{2n}^B}{2},\ \epsilon_n^+ = D\frac{\Delta_{2n+1}^L - \Delta_{2n+1}^B}{2} \tag{3.32}$$

and the combined error signal as

$$\epsilon_n = \frac{\epsilon_n^+ + \epsilon_n^-}{2} = D\frac{\Delta_{2n}^L + \Delta_{2n+1}^L}{2} + D\frac{\Delta_{2n}^B - \Delta_{2n+1}^B}{2}, \tag{3.33}$$

where the terms on the right-hand side represent average frequency offsets over 2-cycle intervals due to laser noise (L) or linear Zeeman shifts (B).

This averaging retains the laser noise contributions giving the first term in the equation, but reduces the magnetic field noise contributions giving the second term. The second term is equivalent to the noise term, η, in equation 3.3, and it is small if the magnetic field does not change much between the measurements for the two lines, so that the two shifts cancel in the averaging. So, the error depends on the variability of the magnetic field noise on time scales on the order of one measurement cycles.

To calculate the long-term instability contributions from these errors we can use equation 3.4 for which we need the Allan variance of the noise. This is

$$\begin{aligned}\sigma_\eta^2(4NT_c) &= \frac{1}{2}\left\langle\left[\frac{1}{N}\sum_{n=N}^{2N-1}\frac{D}{2}\left(\Delta_{2n+1}^B-\Delta_{2n}^B\right)-\frac{1}{N}\sum_{n=0}^{N-1}\frac{D}{2}\left(\Delta_{2n+1}^B-\Delta_{2n}^B\right)\right]^2\right\rangle \\ &= \frac{D^2}{8N^2}\left\langle\left[\sum_{n=N}^{2N-1}\left(\Delta_{2n+1}^B-\Delta_{2n}^B\right)-\sum_{n=0}^{N-1}\left(\Delta_{2n+1}^B-\Delta_{2n}^B\right)\right]^2\right\rangle\end{aligned} \tag{3.34}$$

where the averaging time is a multiple of $4T_c$ because we use 4 measurements (2 lines with 2 measurements each) to make a correction. We can expand the second order binomial and group together diagonal terms and cross terms respectively, also making use of the ergodicity of the noise, i.e. $\left\langle\Delta_n^B\right\rangle = \left\langle\Delta_m^B\right\rangle$, to get

$$\begin{aligned}\sigma_\eta^2(4NT_c) = &\frac{D^2}{2N^2}\sum_{n=0}^{N-1}\left\langle\frac{1}{2}\left[\Delta_{2n+1}^B-\Delta_{2n}^B\right]^2\right\rangle \\ &+\frac{D^2}{2N^2}\sum_{n=0}^{N-1}\sum_{m\neq n}^{N-1}\left\langle\frac{1}{2}\left(\Delta_{2n+1}^B-\Delta_{2n}^B\right)\left(\Delta_{2m+1}^B-\Delta_{2m}^B\right)\right\rangle \\ &-\frac{D^2}{2N^2}\sum_{n=N}^{2N-1}\sum_{m=0}^{N-1}\left\langle\frac{1}{2}\left(\Delta_{2n+1}^B-\Delta_{2n}^B\right)\left(\Delta_{2m+1}^B-\Delta_{2m}^B\right)\right\rangle\end{aligned} \tag{3.35}$$

Here the summands of the first sum are Allan variances, σ_B^2, and we define the summands of the second and third sums as correlations, $\sigma_{BB'}$, which we relate to the Allan variance in Appendix 8 using the bias function B_2 defined by Allan and Barnes [98, 99]. Then by carefully considering all the terms in the double sums we can turn them into single sums, also converting to fractional frequency instability, to get

$$\begin{aligned}\sigma_y^2(4NT_c) = &\frac{1}{2N}\sigma_B^2(2T_c) \\ &+\frac{1}{N^2}\sum_{n=1}^{N-1}(N-n)\sigma_{BB'}(2T_c,2n) \\ &+\frac{1}{2N^2}\sum_{n=1}^{2N-1}(N-|N-n|)\sigma_{BB'}(2T_c,2n).\end{aligned} \tag{3.36}$$

In the case of white noise, all the correlations are 0 (see Appendix 8), so the sums evaluate to zero and the long-term instability contributions from the uncompensated magnetic field errors are simply the Allan variance of the magnetic field noise.

$$\sigma_y^2(\tau) = \sigma_B^2(\tau) \tag{3.37}$$

In the case of flicker noise, the first sum was estimated by numerical evaluation to approach $\approx -0.2N\sigma_B^2(2T_c)$ in the limit of large N, whereas the second sum has a negligible value of

the order $1 \ll N$. Thus, we find the Allan variance as

$$\sigma_y^2(\tau) \simeq 1.2\sigma_B^2 \frac{T_c}{\tau} \tag{3.38}$$

So, averaging two lines with opposite sensitivity to the linear Zeeman shift corrects flicker noise in the magnetic field leaving a residual error with white frequency profile. The instability is on the order of the Allan deviation of the magnetic field noise at an averaging time equal to the time required to measure one line.

Interleaving measurements

We can actually do better than this if we use a servo where the measurements for the two sides of each line are interleaved rather than performed consecutively. In this case, the error signal is

$$\begin{aligned} \frac{\epsilon_+ + \epsilon_-}{2} &= D^2 \frac{\frac{\Delta_n^L + \Delta_n^B + \Delta_{n+2}^L + \Delta_{n+2}^B}{2} + \frac{\Delta_{n+1}^L - \Delta_{n+1}^B + \Delta_{n+3}^L - \Delta_{n+3}^B}{2}}{2} \\ &= D^2 \frac{\Delta_n^L + \Delta_{n+1}^L + \Delta_{n+2}^L + \Delta_{n+3}^L}{4} + D^2 \frac{\frac{\Delta_n^B - \Delta_{n+1}^B}{2} + \frac{\Delta_{n+2}^B - \Delta_{n+3}^B}{2}}{2} \end{aligned} \tag{3.39}$$

In this case, the $\Delta_n^{L,B}$ terms represent average frequency offsets over a single measurement cycle. Similarly to the non-interleaved case, the correction contains the average laser noise and an error from the magnetic field changing between measurements. To calculate the instability of these errors we follow similar steps as before. For brevity, we skip the derivation and quote the results, noting that the instability for white noise magnetic field fluctuations is unchanged whereas that for flicker noise fluctuations is exactly half the result for the non-interleaved servo

$$\sigma_y^2(\tau) \simeq 0.6\sigma_B^2 \frac{T_c}{\tau} \tag{3.40}$$

Adding intermediate corrections

It is possible to increase the feedback rate of the servo by introducing intermediate corrections. These are generated by using the information from one line as soon as it is obtained by averaging it with the last measurement of the other line (which has been used to calculate a correction already) rather than waiting for a new one. In other words, one can use the new information about one line as soon as it is generated rather than waiting for new information about both lines. So, instead of applying a single correction $\frac{\epsilon_n^+ + \epsilon_n^-}{2}$ at times $4T_c \times n$, we also apply another correction $\frac{\epsilon_n^+ + \epsilon_{n-1}^-}{2}$ at times $4T_c \times n - 2T_c$. Assuming for simplicity that the lines are measured one-by-one rather than in the interleaved fashion,

the instability in this case is

$$\sigma_\eta^2(2NT_c) = \frac{1}{2}\left\langle \left[\frac{1}{N}\sum_{n=N}^{2N-1} \frac{1}{2}(-1)^n \left(\Delta_{n+1}^B - \Delta_n^B\right) - \frac{1}{N}\sum_{n=0}^{N-1} \frac{1}{2}(-1)^n \left(\Delta_{n+1}^B - \Delta_n^B\right) \right]^2 \right\rangle \tag{3.41}$$

where the averaging time is $\tau = 2NT_c$ because we make a new correction once every two cycles and the offsets, Δ^B, are averages over a time interval $\tau = 2T_c$ like before. We can note that in the limit $N \gg 1$, the sums approach

$$\begin{aligned}
\sum_{n=0}^{N-1}(-1)^n \left(\Delta_{n+1}^B - \Delta_n^B\right) &= -\Delta_0^B + \Delta_1^B + \Delta_1^B - \Delta_2^B - \Delta_2^B + \Delta_3^B + ... \\
&= 2\sum_{n=0}^{N/2-1} \left(\Delta_{2n+1}^B - \Delta_{2n}^B\right) + \left(\Delta_0^B - (-1)^{N-1}\Delta_N^B\right) \\
&\approx 2\sum_{n=0}^{N/2-1} \left(\Delta_{2n+1}^B - \Delta_{2n}^B\right)
\end{aligned} \tag{3.42}$$

By writing both sums this way and making a substitution $N = 2M$ we get back equation 3.34. Thus, the intermediate corrections do not affect the long-term instability, though they can increase the bandwidth of the servo.

Including the sensitivity function

The model for the linear Zeeman shift stability can be generalised by accounting for dead time between measurements as well as for the spectroscopic protocol (Rabi, Ramsey or dynamical decoupling). This can be included in our model by acknowledging that the variation in excitation fraction depends not on the mean frequency shifts, $\bar{\Delta}_n^B$, but rather on the sensitivity-weighted mean frequency shifts. Then we get an equation similar to equation 3.13

$$\delta F_n = \pi \int_{-\infty}^{\infty} \Delta^B(t) g^B(t - nT_c) dt, \tag{3.43}$$

where the single interrogation sensitivity function for Zeeman shifts, $g^B(t)$, is defined to be zero for times $t \notin [0, T_c]$ and otherwise the same as the sensitivity function for laser noise up to a minus sign depending on which m_F state is used and which side of the transition line we centre the laser on. We also define the error sensitivity function for the error in the averaging of two lines using 4 measurements

$$g_\eta^B(t) = \frac{1}{4}\left[g^B(t) + g^B(t - T_c) - g^B(t - 2T_c) - g^B(t - 3T_c)\right], \tag{3.44}$$

such that the noise component in the error signal becomes

$$\eta_n = \pi \int_{-\infty}^{\infty} \Delta^B(t) g_\eta^B(t - 4nT_c) dt \tag{3.45}$$

For a uniform sensitivity $g^B(t \in [0, T_c]) = 1$, we see that this is equivalent to our original expression for the error term in equation 3.33 for a discriminator $D = \pi T_c$.

The rest of the derivation will follow a similar approach to the one in [71] which was done for the Dick effect instability. We start by defining the aggregated sensitivity function

$$h^B(t) = \frac{1}{N} \sum_{n=N}^{2N-1} g_\eta^B(t - 4nT_c) - \frac{1}{N} \sum_{n=0}^{N-1} g_\eta^B(t - 4nT_c) \tag{3.46}$$

In this case, N is the number of measurement sets, where each set estimates both lines using 4 measurements. This allows us to write the Allan variance of the errors as

$$\sigma_\eta^2(4NT_c) = \left\langle \frac{1}{2} \left[\pi \int_{-\infty}^{\infty} \Delta^B(t) h^B(t) dt \right]^2 \right\rangle, \tag{3.47}$$

which after several steps including converting into the frequency domain (see [71], equations 3.38) can be expressed in terms of the power spectral density of the linear Zeeman shifts, $S^B(f)$, and the Fourier transform of the aggregated sensitivity function, $\hat{h}^B(f)$,

$$\sigma_\eta^2(4NT_c) = \frac{\pi^2}{2} \int_{-\infty}^{\infty} \left| \hat{h}^B(f) \right|^2 S_\nu^B(f) df \tag{3.48}$$

Next, we use the Fourier transform shift property

$$\mathcal{F}\left\{ g(t - 4nT_c) \right\} = e^{-2\pi i 4nT_c} \mathcal{F}\left\{ g(t) \right\} \tag{3.49}$$

and the linearity of the Fourier transform to express $\hat{h}^B(f)$ in terms of $\hat{g}_\eta^B(f)$ as

$$\hat{h}^B(f) = -2ie^{-i\pi 4(2N-1)T_c f} \frac{\sin^2(\pi 4NT_c f)}{N \sin(\pi 4T_c f)} \hat{g}_\eta^B(f) \tag{3.50}$$

and $\hat{g}_\eta^B(f)$ in terms of $\hat{g}^B(f)$ as

$$\hat{g}_\eta^B(f) = ie^{-3\pi i T_c f} \sin(2\pi T_c f) \cos(\pi T_c f) \hat{g}^B(f) \tag{3.51}$$

Combining these expressions and squaring we get

$$\left| \hat{h}^B(f) \right|^2 = \frac{\sin^4(\pi 4NT_c f) \cos^2(\pi T_c f)}{N^2 \cos^2(\pi 2T_c f)} \left| \hat{g}^B(f) \right|^2 \tag{3.52}$$

In the limit of large N, this approaches a sum of delta functions

$$\left|\hat{h}^B(f)\right|^2 = \frac{1}{4NT_c}\sum_{-\infty}^{\infty}\delta\left(f-\frac{2m+1}{4T_c}\right)\left|\hat{g}^B(f)\right|^2 \tag{3.53}$$

which turns equation 3.48 into

$$\sigma_\eta^2(4NT_c) = \frac{\pi^2}{8NT_c}\sum_{-\infty}^{\infty}\left|\hat{g}^B\left(\frac{2m+1}{4T_c}\right)\right|^2 S_\nu^B\left(\frac{2m+1}{4T_c}\right) \tag{3.54}$$

Since the sensitivity function is real, its Fourier transform is symmetric. So, we can convert to the single sided power spectral density as $S_\nu^B(f) = \frac{1}{2}L_\nu^B(|f|)$ and sum twice over $m \geq 0$ terms only. Finally, generalising the averaging time $\tau = 4NT_c$, we write the Allan variance of the errors as

$$\sigma_\eta^2(\tau) = \frac{1}{\tau}\frac{\pi^2}{2}\sum_{m=0}^{\infty}\left|\hat{g}^B\left(\frac{2m+1}{4T_c}\right)\right|^2 L_\nu^B\left(\frac{2m+1}{4T_c}\right) \tag{3.55}$$

And using equation 3.4 we find the fractional frequency instability as

$$\sigma_y^2(\tau) = \frac{1}{\tau}\frac{\pi^2}{2D^2\nu_0^2}\sum_{m=0}^{\infty}\left|\hat{g}^B\left(\frac{2m+1}{4T_c}\right)\right|^2 L_\nu^B\left(\frac{2m+1}{4T_c}\right) \tag{3.56}$$

The results obtained in the first part of this subsection were based on a constant sensitivity function, $g^B(t \in [0, T_c]) = 1$, which has a discriminator $D = \pi T_c$ and the Fourier transform

$$\left|\hat{g}^B\left(\frac{2m+1}{4T_c}\right)\right|^2 = \frac{8}{\pi^2}\frac{T_c^2}{(2m+1)^2} \tag{3.57}$$

We can try to reproduce the results for this special case using our general result. For a magnetic field noise that has a white frequency profile $L_\nu^B(f) = 2\sigma_B^2(\tau = 1s)\nu_0^2$, where σ_B represents the Allan deviation of the linear Zeeman shifts in fractional frequency units, and the instability is

$$\begin{aligned}\sigma_y^2(\tau) &= \frac{\sigma_B^2(1s)}{\tau}\frac{8}{\pi^2}\sum_{m=0}^{\infty}\frac{1}{(2m+1)^2} \\ &= \sigma_B^2(\tau)\end{aligned} \tag{3.58}$$

The sum of the squared inverses of the odd numbers is exactly $\frac{\pi^2}{8}$, so the instability of the errors is equal to the instability of the shifts.

For a magnetic field noise that has a flicker frequency profile $L^B(f) = \frac{\sigma_B^2}{2\ln 2}\nu_0^2 f^{-1}$, and

the instability is

$$\begin{aligned}\sigma_y^2(\tau) &= \frac{\sigma_B^2}{2\ln 2}\frac{4T_c}{2\tau}\frac{8}{\pi^2}\sum_{m=0}^{\infty}\frac{1}{(2m+1)^3} \\ &= \frac{7\zeta(3)}{\pi^2\ln 2}\sigma_B^2\frac{T_c}{\tau},\end{aligned} \tag{3.59}$$

where $\zeta(3) = 1.202..$ is the Riemann zeta function and the whole prefactor evaluates to about 1.23, in agreement with our result from the numerical calculation using correlations $\sigma_{BB'}$ (see equation 3.38).

Our equation 3.56 is not completely general as it is specific to the order in which we measure different sides of the two transition lines. To calculate the instability for the interleaved servo, we repeat this derivation modifying equation 3.44 writing the error sensitivity function as

$$g_\eta^B(t) = \frac{1}{4}\left[g^B(t) - g^B(t-T_c) + g^B(t-2T_c) - g^B(t-3T_c)\right], \tag{3.60}$$

And its Fourier transform becomes

$$\hat{g}_\eta^B(f) = ie^{-3\pi i T_c f}\sin(\pi T_c f)\cos(2\pi T_c f)\hat{g}^B(f) \tag{3.61}$$

which combined with equation 3.50 leads to

$$\begin{aligned}\left|\hat{h}^B(f)\right|^2 &= \frac{\sin^4(\pi 4NT_c f)\sin^2(\pi T_c f)}{N^2\sin^2(\pi 2T_c f)}\left|\hat{g}^B(f)\right|^2 \\ &\overset{N\gg 1}{=} \frac{1}{2NT_c}\sum_{-\infty}^{\infty}\delta\left(f - \frac{2m+1}{2T_c}\right)\left|\hat{g}^B(f)\right|^2\end{aligned} \tag{3.62}$$

and then plugging this result in equation 3.48 we get the Allan variance of the errors as

$$\sigma_y^2(\tau) = \frac{\pi^2}{\tau}\sum_{m=0}^{\infty}\left|\hat{g}^B\left(\frac{2m+1}{2T_c}\right)\right|^2 L_\nu^B\left(\frac{2m+1}{2T_c}\right) \tag{3.63}$$

and the fractional frequency instability as

$$\sigma_y^2(\tau) = \frac{1}{\tau}\frac{\pi^2}{D^2\nu_0^2}\sum_{m=0}^{\infty}\left|\hat{g}^B\left(\frac{2m+1}{2T_c}\right)\right|^2 L_\nu^B\left(\frac{2m+1}{2T_c}\right) \tag{3.64}$$

If we again try the constant sensitivity case (equation 3.57) we have that

$$\left|\hat{g}^B\left(\frac{2m+1}{2T_c}\right)\right|^2 = \frac{4}{\pi^2}\frac{T_c^2}{(2m+1)^2} \tag{3.65}$$

So, for white noise

$$\begin{aligned}\sigma_\eta^2(\tau) &= \frac{2\sigma_B^2(1s)\nu_0^2}{\tau}\frac{1}{\nu_0^2 T_c^2}\frac{4T_c^2}{\pi^2}\sum_{m=0}^{\infty}\frac{1}{(2m+1)^2} \\ &= \sigma_B^2(\tau)\end{aligned} \tag{3.66}$$

While for flicker noise

$$\begin{aligned}\sigma_\eta^2(\tau) &= \frac{\sigma_B^2}{2\ln 2}\frac{2T_c}{\tau}\frac{4}{\pi^2}\sum_{m=0}^{\infty}\frac{1}{(2m+1)^3} \\ &= \frac{7\zeta(3)}{\pi^2 2\ln 2}\sigma_B^2\frac{T_c}{\tau},\end{aligned} \tag{3.67}$$

which is half the value that we get in the non-interleaved case. So, the interleaved servo has an advantage over the non-interleaved servo for flicker noise but is the same for white noise as neither servo can correct white noise.

The instability of the uncompensated Zeeman shift errors has a similar expression to that of the Dick effect instability, in which the local oscillator noise spectrum is replaced by the spectrum of the linear Zeeman shifts. However, there are subtle differences in their relationships with dead-time and probe time stemming from their fundamentally different nature. Their difference can be summarised in the following way. The Dick effect errors arise due to aliasing of the laser noise because of variations in sensitivity, while the source of linear Zeeman shift errors is twofold, having a similar contribution from the same sensitivity function but also one from the field changes between measurements of the two lines. This is most evident in the case where the sensitivity is constant and there is no dead time, since in that case, the Dick effect vanishes while Zeeman shift errors persist. In Figure 3.13 we calculate the two instabilities for a range of dead time and probe time values to illustrate this. When dead time is short, we get back the instabilities calculated at the start of this section for the linear Zeeman shift errors. At longer dead time, the sensitivity function errors become dominant and the two effects converge. This is also true when the probe time is short. As the probe time increases, however, the sensitivity function errors decrease monotonically, whereas the errors from field changes behave differently, asymptoting to the zero dead time value for white noise and increasing for flicker noise.

Contribution to phase variance

As mentioned in section 3.3.1, the variance of the measurement phase distribution depends on both laser noise and noise from external fields that shift the atomic transitions. Although the linear Zeeman shifts are canceled to the degree that was discussed in this section by averaging measurements from the two lines, the shifts still cause additional phase noise during the interrogation leading to a higher phase variance. When assessing the additional instability contributions from these shifts, both the errors from the uncompensated shifts and the increased phase variance need to be taken into account.

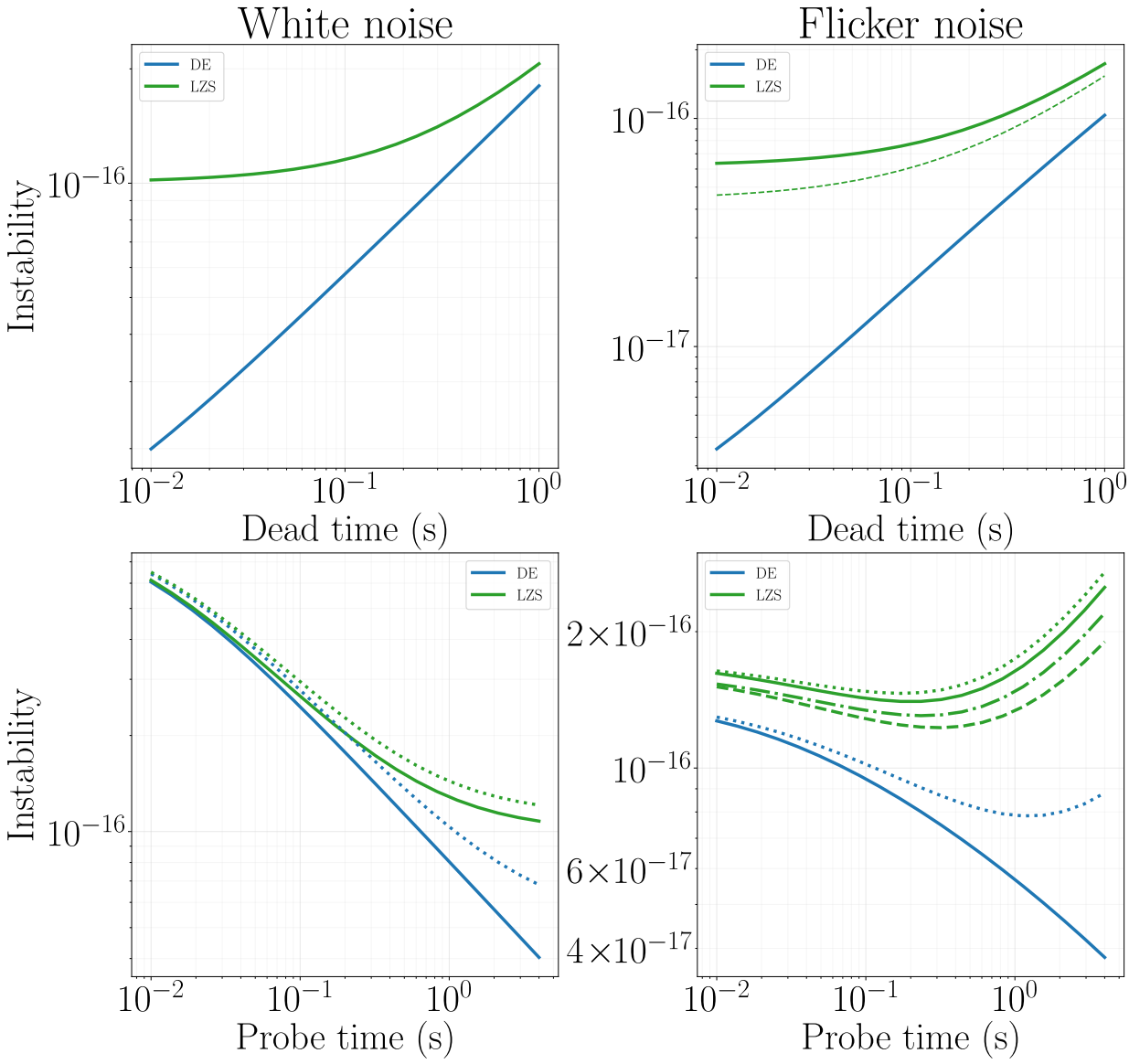

Figure 3.13: **Comparison of Linear Zeeman shift errors and Dick effect noise**. The Allan deviation at 1 s is calculated for both effects assuming 1×10^{-16} white/flicker noise at 1 s averaging time for LO noise and Zeeman shift noise respectively. The top plots are for 300 ms Ramsey probes and varying dead time. Bottom plots are for cycles with 650 ms dead time and varying probe time. Blue and greed curves represent the Dick effect instability and the Linear Zeeman shift errors respectively. Dashed lines show the Zeeman instability for the interleaved servo. Dotted lines show instabilities when Rabi probes are used instead of Ramsey probes.

Chapter 4

Duty cycle engineering for zero dead-time operation

As they stand, optical lattice clocks are limited in terms of stability by the large Dick effect which is typically at a level of a few parts in 10^{16}, about an order of magnitude larger than typical quantum projection noise levels even with state of the art optical cavities. As mentioned in the first chapter, improvements in the fractional frequency stabilities of optical cavities would certainly provide an advantage because not only would that reduce the noise level of the laser but at the same time it would allow longer interrogations improving the duty cycle. In this chapter, however, we consider the potential to improve the duty cycle solely by changing the interrogation protocol to optimise the sensitivity function [83], and without requiring changes to the detection type [61].

4.1 Dynamical decoupling from laser noise

The total sensitivity of the frequency measurements plays an important role in the stability of the clock as it sets the value of the discriminator which significantly impacts instability according to equation 3.5. The shape of the sensitivity function also has an impact on the instability through the Dick effect, with the accent being put on the duty cycle, $T_i/(T_d+T_i)$. Since the dead-time is more or less fixed by the rate at which atoms can be loaded in the optical lattice and the total sensitivity is limited by the requirement for phase coherence, we consider the potential benefits arising from a lower sensitivity level. The idea is essentially to partially decouple the atomic state from the laser noise so as to reduce the measurement phase variance. This would allow longer interrogations with the same total sensitivity and phase coherence, thus increasing the duty cycle without changing the discriminator. This would also have a benefit in the composite clock scheme with interleaved operation assisting in reaching a zero dead-time configuration.

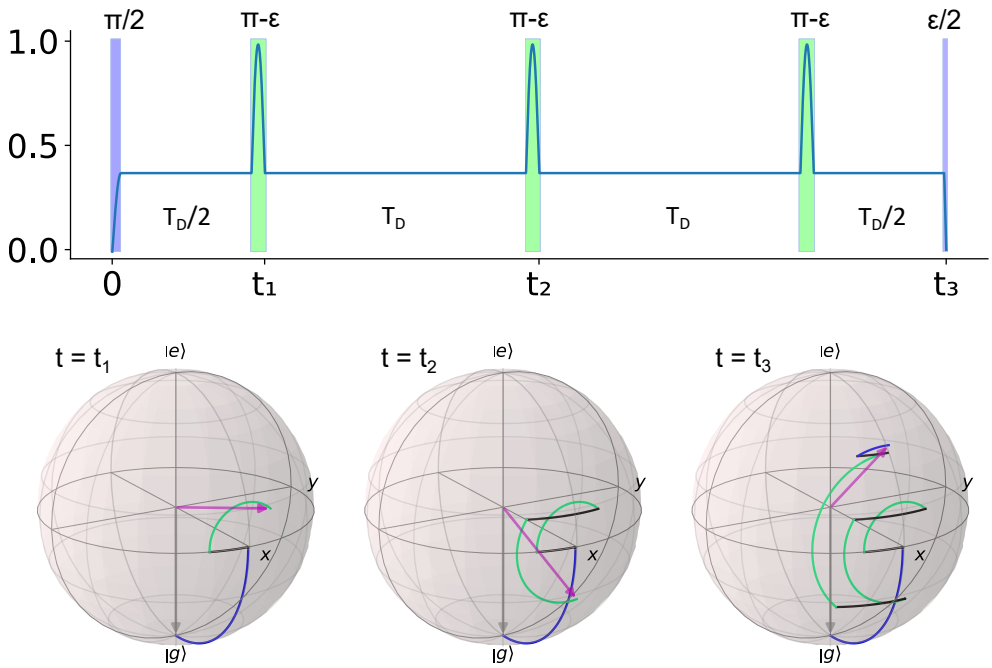

Figure 4.1: **Dynamical decoupling protocol**. *Top*: Pulse sequence and sensitivity function. *Bottom*: The Bloch vector evolution from initial state to three different times in the sequence.

4.1.1 Interrogation protocol

An interrogation scheme that decouples the measurement from laser noise was proposed in 2020 [65]. The method is similar to Ramsey interrogation only instead of letting the atomic phase evolve freely during the time between the two $\pi/2$ pulses we frequently interrupt the evolution by flipping the phase. In the Bloch vector picture (see Figure 4.1), the first pulse brings the atomic state to the equatorial plane of the Bloch sphere. Then subsequent laser pulses with area slightly less than π rotate the Bloch vector thus reversing the differential phase. This slows down the accumulation of the differential phase to a degree given by the area of the flip pulse, $\pi - \epsilon$, where a higher pulse area defect, ϵ, indicates a higher sensitivity.

The resulting sensitivity function is depicted in Figure 4.2 and compared to a Ramsey interrogation having the same total integrated sensitivity. The sensitivity level is given by $\sin\frac{\epsilon}{2}$ which is around 0.54 in this particular case, and the interrogation is extended by increasing the dark time to maintain the same total integrated sensitivity and therefore the same discriminator. This can be seen in the atomic excitation lineshapes of the two spectroscopy types which match for the detuning region near the central fringe. The overlap range can be extended by using more frequent flip pulses to enhance the phase coherence.

The flip pulses with area $\pi - \epsilon$ contribute spikes in the sensitivity which lead to slightly higher Dick effect noise. One could imagine an unfortunate sequence on the Bloch sphere where the phase evolution happens to be changing course after every flip pulse, thus ending

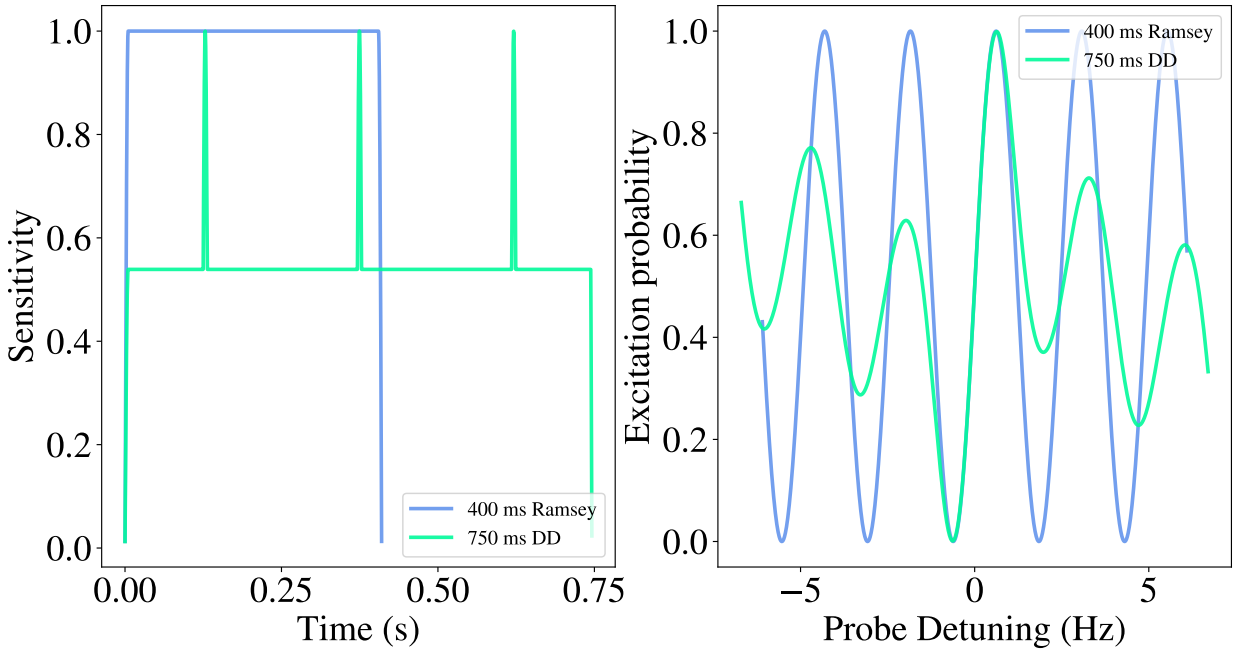

Figure 4.2: **Dynamical decoupling spectroscopy features**. Sensitivity function (left) and atomic excitation probability (right) for an interrogation using dynamical decoupling (lime green) and for standard Ramsey interrogation (blue).

up with a larger value than in the Ramsey case. In other words, this sequence has particular sensitivities to laser noise with frequencies of multiples of $1/T_D$, the inverse of the dark time between pulses. This is indeed true and is reflected in the Fourier transform of the sensitivity function shown in Figure 4.3. Compared to the Ramsey case, there are higher amplitudes at frequencies of 4 Hz, 8 Hz, 12 Hz... corresponding to a dark time of 250 ms, as selected for this example. In particular, the odd harmonics have a higher amplitude than the even harmonics, which is consistent with the phase evolution in the Bloch picture. Thus, the effect can be accounted for by the Dick effect estimation by simply using the right sensitivity function. It should be noted that the effect is reduced when the flip pulse error is large (i.e. pulses have a small area) or when the π-pulse time is short.

On the other hand, the advantage of the dynamical decoupling probe is the higher duty cycle that it would offer when cycles have dead time. This can be seen in the bottom of Figure 4.3, where the Fourier amplitude of the sensitivity function is exacerbated at low frequencies compared to the zero dead time case. These amplitudes roll off with a $1/f^2$ decay. The extended dynamical decoupling probes have a significant advantage here, as illustrated by the fitted lines.

4.1.2 Demonstration of extended clock probes in Sr1

As a first step towards realising a zero dead-time composite clock we have implemented dynamical decoupling interrogations in the first generation Strontium optical lattice clock at NPL, Sr1. The coherence-imposed limit on measurement time is around 330 ms for

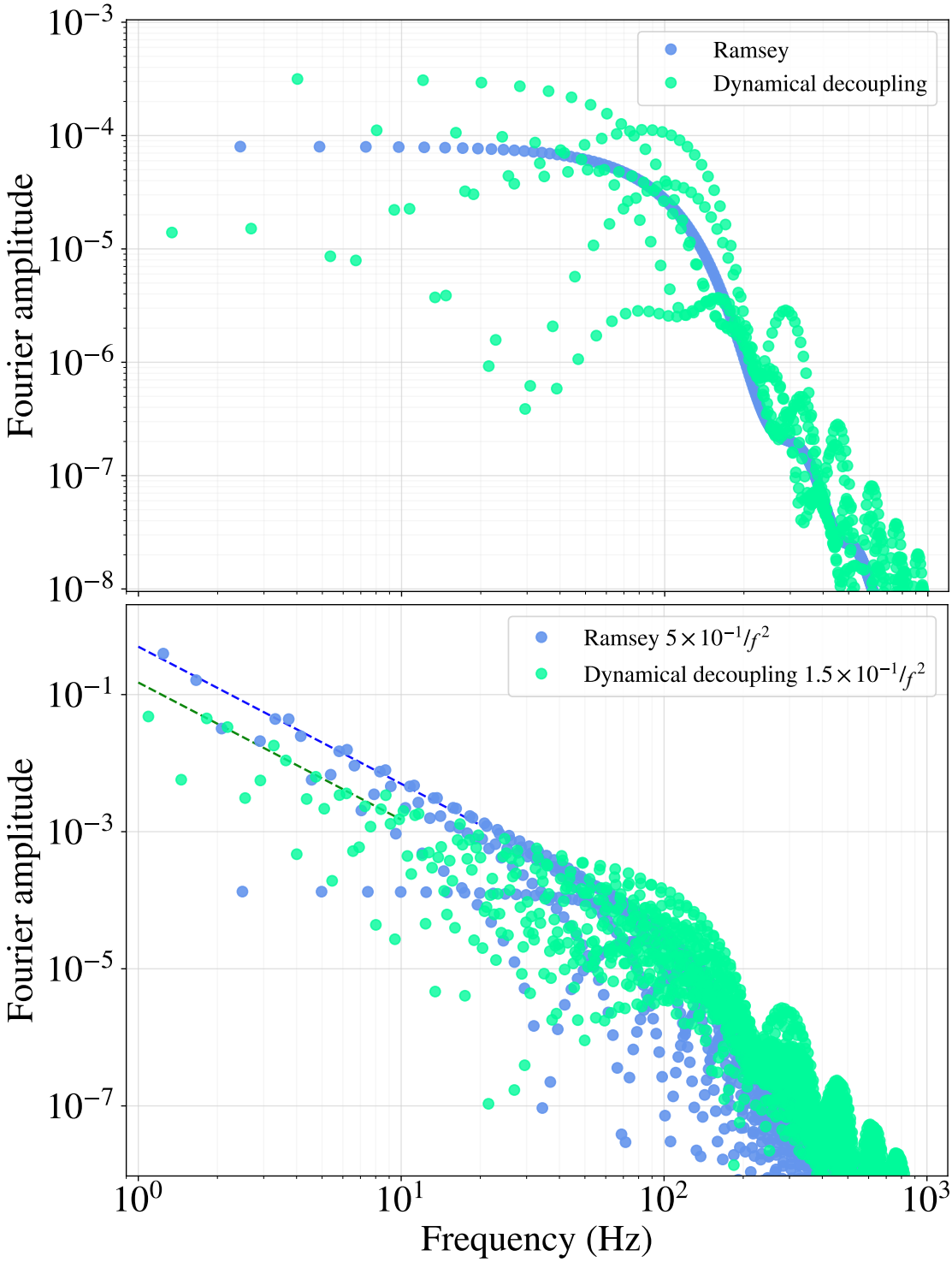

Figure 4.3: **Fourier transform of sensitivity functions**. *Top*: Ramsey and Dynamical decoupling interrogations as shown in Figure 4.2. *Bottom*: The same Ramsey and Dynamical interrogations with 2 s dead time added to each. The Dashed lines indicate the approximate $1/f^2$ scaling for the largest contributing terms.

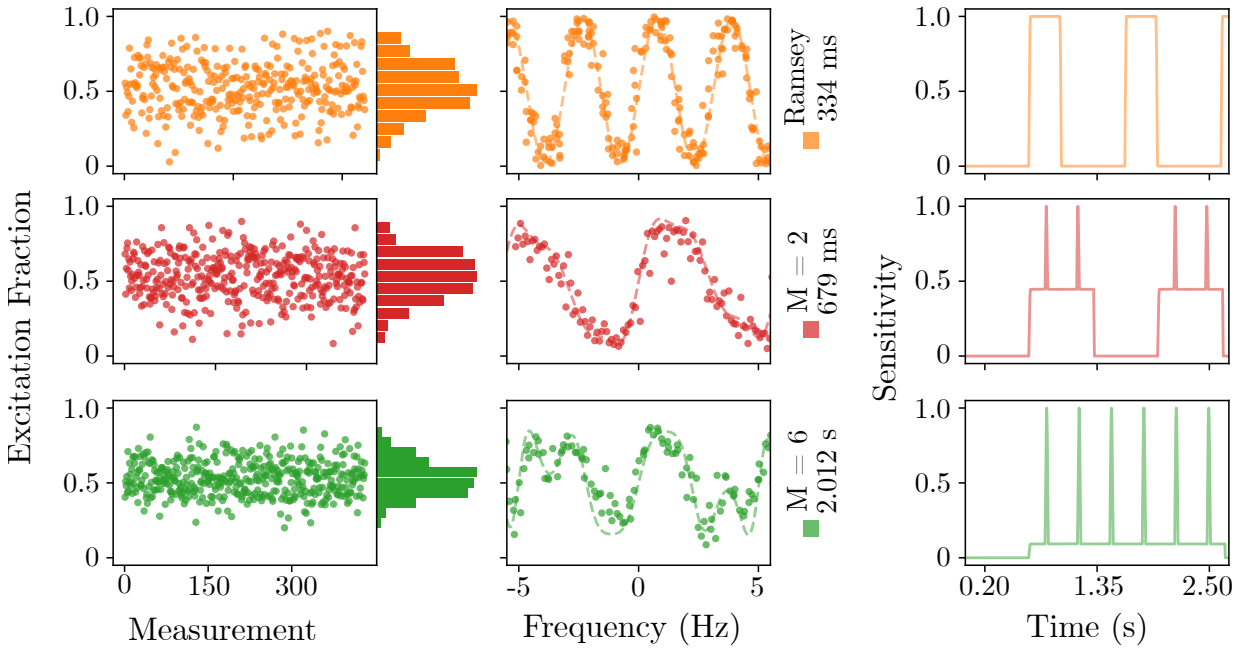

Figure 4.4: **Dynamical decoupling spectroscopy in Sr1**. Spectroscopic data from Sr1 using standard Ramsey interrogations (top row), dynamical decoupling interrogations with M=2 probe extension factor (middle row) and dynamical interrogations with M=6 probe extension factor (bottom row). For each row, the excitation noise data taken during clock operation is shown on the left with the associated histogram on the side, the excitation fraction data while scanning the laser frequency is shown in the middle, and the theoretical sensitivity function is shown on the right. This figure also appears in our paper [83].

Ramsey interrogations. Figure 4.4 shows the atomic excitation fraction recorded while the clock was locked and while the laser frequency was scanned near the resonance alongside calculated sensitivity functions for each case. The excitation response follows the theoretically expected lineshapes for sequences with probe times extended by a factor M=2 and M=6 respectively. We observe a loss of contrast for the extended probes which remains to be investigated further. At the moment, we suspect the fidelity of the pulses to be a limiting factor rather than atomic coherence since previous measurements of similar length showed very good contrast [64]. Correcting for the loss of contrast, the discriminator is preserved to a good degree.

4.1.3 Single clock improvement

This method could benefit optical lattice clocks which have significant dead-time in the experimental sequence. Longer probes with a reduced sensitivity level maintain the total integrated sensitivity while reducing noise due to the Dick effect significantly. There is, however, a trade-off since the servo correction rate is reduced by the longer cycle time affecting CTL and QPN slightly. Trading Dick effect noise for QPN is a good thing because the former dominates the total instability. Trading Dick effect noise for CTL, on the other

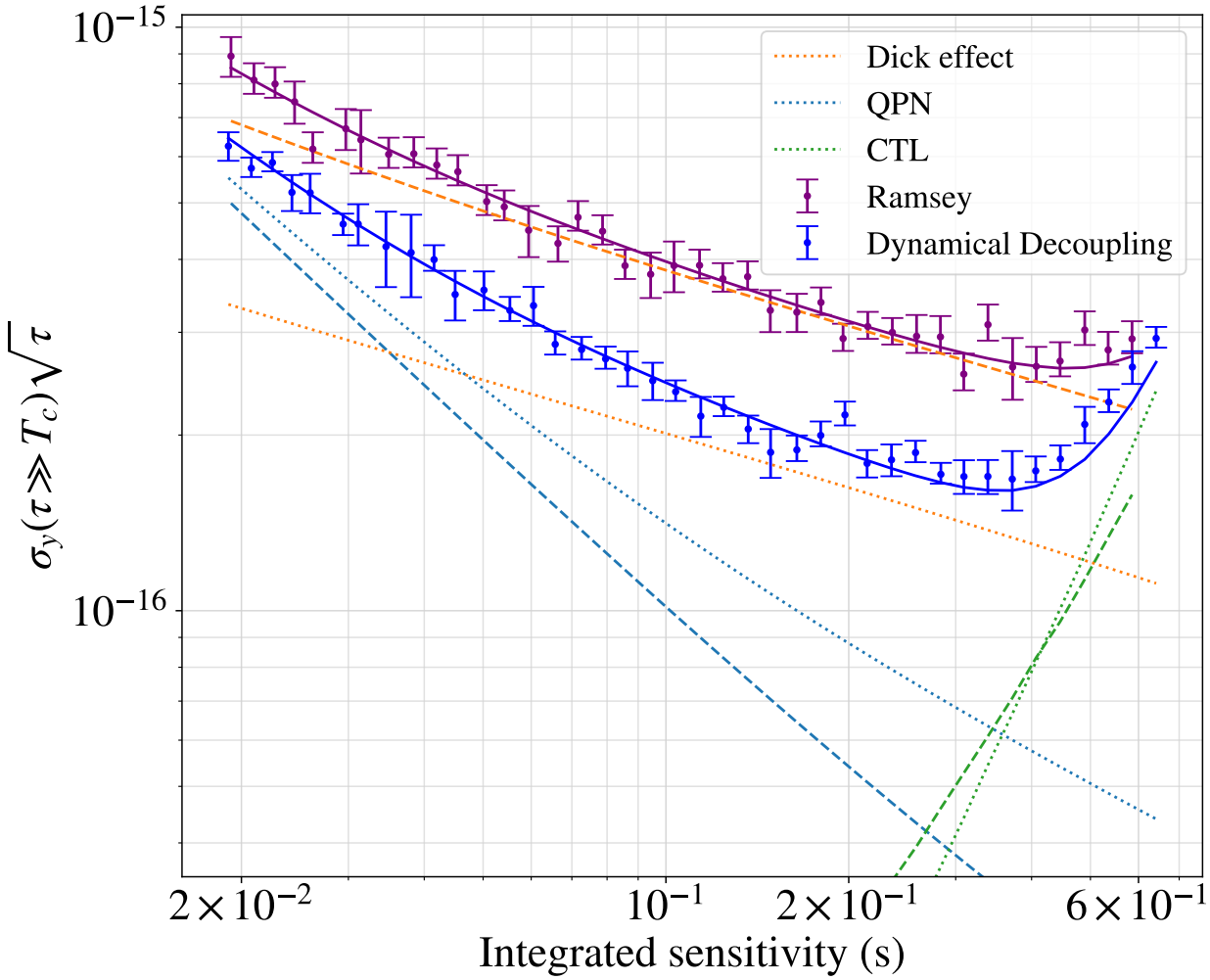

Figure 4.5: **Dynamical decoupling in a single clock**. Purple (blue) dots show simulated data for the Ramsey operation along the theoretical model prediction line in purple (blue). Dashed (dotted) lines show the individual contributions from different noise sources as calculated theoretically for clocks using Ramsey (dynamical decoupling) spectroscopy.

hand, is only useful when CTL is low. But since the best potential stability occurs at the optimal probe time where CTL and Dick effect noise are similar it remains to be seen what can be achieved in terms of the optimal instability by using dynamical decoupling.

To that end, we simulate standard Ramsey interrogations and dynamical decoupling interrogations for a range of probe times to obtain the best instability achievable in each case. We use laser noise with a white frequency noise component of $1 \times 10^{-16}/\sqrt{\tau}$ and a flicker frequency noise component of 3×10^{-16} and calculate corrections from single measurements with 650 ms dead-time. For dynamical decoupling, we use 32 flip pulses with area defects of $\epsilon = 2 \arcsin 1/8$ to achieve a sensitivity level of $\approx 1/8$. The results are presented in Figure 4.5 plotted as instability vs. integrated sensitivity rather than probe time for ease of comparison. We determine a minimum instability of 2.6×10^{-16} at the optimal probe time of 450 ms for Ramsey interrogations and a minimum instability of

1.6×10^{-16} at a probe time of 3 s for dynamical decoupling equivalent to a reduction of 40% in instability.

4.2 Composite clocks with interleaved measurements

Another method to change the duty cycle beyond the limit imposed by laser phase coherence is to use multiple frequency references interrogated by the same LO, such that their duty cycles add up. This leads to the concept of zero dead-time composite systems. Using two clocks is an effective way to remove the Dick effect contribution allowing the clock performance to reach the Standard Quantum Limit (SQL) line set by QPN. In this method, two lattice clocks operate together with measurements interleaved such that the spectroscopy stage in one clock corresponds with the atomic preparation stage in the other clock leaving no effective dead-time.

A zero dead time composite clock, however, requires each clock to have a duty cycle of at least 50%, so that the interrogations can be interleaved with no gaps. The resulting sensitivity function can be very uniform if Ramsey spectroscopy is employed instead of Rabi pulses. In fact, even for Ramsey spectroscopy, a slightly larger duty cycle would be beneficial as it would allow to overlap the Ramsey pulses resulting in a more uniform combined sensitivity at the edges of the measurements, especially if the timing offset between the two clocks is optimised [36] or the amplitude of the pulses is modulated. This is difficult to achieve as in most systems, including the optical lattice clocks at NPL, the preparation time required for obtaining a reasonable number of atoms is larger than the longest phase coherent Ramsey interrogation allowed by the phase noise of the LO. Nevertheless, the technique of interleaving measurements can still yield stability improvements.

4.2.1 Simulations for Sr1 and Sr2

In this section, the stability performance of composite schemes with different spectroscopy types is evaluated through numerical simulations for estimating the potential gains that could result from Sr1 and Sr2 operating together. Composite Ramsey schemes are simulated where the dark time is varied to find the optimal point where the Dick effect is minimised while still maintaining low CTL, in the same way as the optimal probe time for a single clock is determined. The same method is applied for clocks using Rabi pulses. This case is interesting because, although the sensitivity function is not as smooth during the pulse, the larger duty cycles could provide an advantage. Finally, a promising technique for zero dead time operation based on dynamical decoupling spectroscopy is proposed and evaluated. Similarly to Rabi, the reduced sensitivity function allows for longer probes. However, the dynamical decoupling protocol has a more uniform sensitivity. In those simulations, the total probe time is constant and equal to the dead time, and instead the sensitivity level is varied by modifying the flip pulse error to find the optimal value.

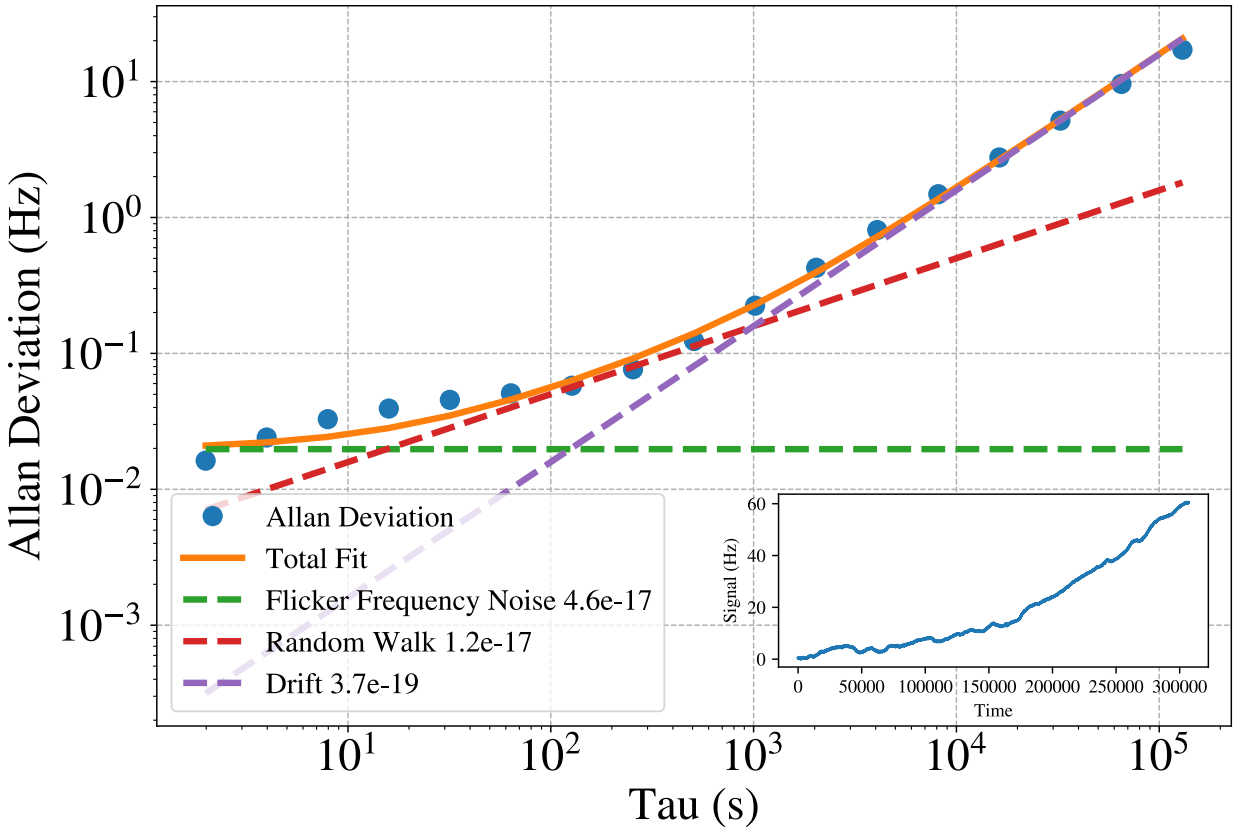

Figure 4.6: **Clock corrections ADEV**. The Allan deviation is computed for the corrections made by the Sr lattice clock to keep the clock laser on the centre frequency, from a period of over 3 days of running the clock (data show in the inset. A fit (solid line) is applied made up of individual components (dashed lines) from flicker frequency noise, random frequency walk noise and frequency drift.

Realistic simulation parameters

An important consideration for being able to extract useful results from the simulations is that the profile of the LO frequency noise and of the magnetic field noise be characterised. The LO frequency stability is largely determined by the ultra stable optical cavity. Measurements of the cavity against a cryogenic silicon cavity connected over an optical fibre network indicate a flicker floor of 7×10^{-17} fractional frequency instability [82]. However, the measurement contains significant noise from the link at short time scales that are relevant for the clock. The development of a new ultrastable cavity at NPL provided the opportunity for a comparison between the two cavities with lower noise on shorter timescales. This indicates a roughly flat Allan deviation at the 2×10^{-16} level around the 2 s range. This flicker-like noise process can be attributed to acceleration noise and is particularly important because it affects frequencies on the order of a clock cycle. Therefore, this is the value that was used in the stability simulations for the flicker noise.

For the frequency stability at longer times the corrections made by the atomic servo can provide an estimate. Figure 4.6 shows the Allan deviation of those corrections from a

3.5 days long stretch of data that was collected during our 2025 summer campaign. Fits to the Allan deviation plot yield a random frequency walk component with 1.2×10^{-17} instability at 1 s as well as a frequency drift of 3.7×10^{-19}/s. Only the random walk component would affect the clock stability, as the drift is easily compensated through the use of a second integrator and therefore is not included in the simulation.

For the white frequency noise component, an estimate can be made by considering the instability of the clock from recent comparisons with other optical lattice clocks, of around $3 \times 10^{-17}/\sqrt{\tau}$ [20]. Assuming the stability of the comparison to be at the level of Sr1, and that level to be set by the Dick effect for cycles with 400 ms interrogation times and 650 ms dead times, and lastly that the flicker and random walk components to be at the levels specified earlier, we arrive at an estimate for the white noise component of $2 \times 10^{-16}/\sqrt{\tau}$. Although we might expect a lower value for the ultrastable cavity, there may be additional white noise on the clock laser due to residual amplitude modulation from the PDH lock and inter-branch noise from the comb.

Another useful piece of information that can be obtained from the clock operation is the variation of the Zeeman stretched states splitting estimated through the difference between the frequencies of the two servos that follow each line. Although this quantity is subject to excessive white noise from the clock measurements as well as aliasing from the non-simultaneous measurements of the two lines, it can still be used to estimate variations on longer time scales. Figure 4.7 shows the Allan deviation of the frequency difference revealing a flicker frequency component of 3.6×10^{-17} and a random frequency walk component with 1.9×10^{-18} instability at 1 s. We include such effects in the simulation by generating another set of frequency noise data similar to that for laser noise, but which is included only in the measurements and not in the clock output.

Interleaving m_F transition lines from two clocks

The Zeeman shift correction requires probing two transition lines in each clock. The magnetic field noise is not necessarily correlated between the two clocks, which means that in terms of linear Zeeman shift instability, the zero dead-time clock does not have an advantage because it does not increase the rate of corrections for each line. We could increase the rate by combining the servos between the two clocks. This would double the correction rate roughly reducing the instability by a factor of $\sqrt{2}$. However, it would also increase the noise by the same factor by mixing the uncorrelated magnetic field noise from the two clocks.

Simulation results

The simulation results are summarised in Figure 4.8. The instability limit is estimated from the long term asymptotic behaviour of the Allan deviation line for each case and plotted against the effective probe time. The single clock cases for Rabi and Ramsey interrogations are also shown for reference showing only a negligible improvement for Ramsey over Rabi. Between the single clocks and the composite clocks using standard spectroscopy types there

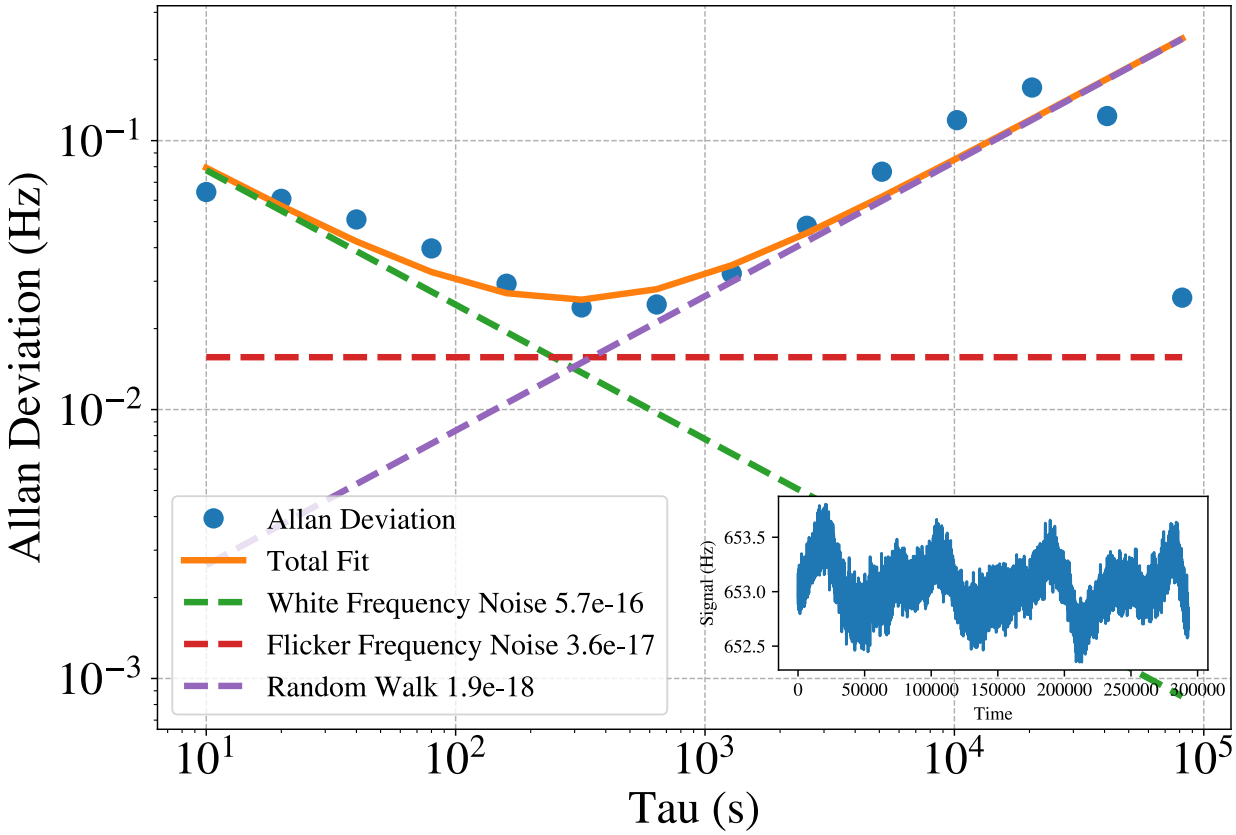

Figure 4.7: **Stability of Zeeman shifts**. The Allan deviation is computed for the Zeeman stretched state splitting for a period of over 3 days (shown in the inset), estimated from the frequencies of the two servos tracking the opposite lines while the Sr lattice clock was running. A fit (solid line) is applied made up of individual components (dashed lines) from flicker noise, random walk noise and white noise.

is a factor of 2 difference in stability, and the composite clock using dynamical decoupling spectroscopy brings another factor of 2 improvement.

In Figure 4.9, the Allan deviation plots for the composite clocks with optimal probe times are shown, with estimates for the individual noise contributions. Because of the high sensitivity of the Ramsey interrogation, the optimal probe time is limited and dead time is still present but nevertheless the Dick effect is reduced by a factor of 4 from the value for a single clock. Furthermore, an improvement in the QPN is also achieved thanks to the higher rate of corrections. For the Rabi case, the limiting factor remains the Dick effect with only a factor of 2 improvement from the single clock case due to the highly non-uniform sensitivity even in the zero dead time case. The dynamical decoupling zero dead time clock shows excellent suppression of the Dick effect instability by an order of magnitude, to a level slightly below the QPN. However, its QPN level is slightly larger than that of the Ramsey composite clock. This is in part due to its slower rate of corrections and also in part due to its lower total sensitivity, as can be seen by the shorter optimal probe time in Figure 4.8. The shorter effective optimal probe time is a consequence of the increased phase variance of the dynamical decoupling spectroscopy. This can be improved by using

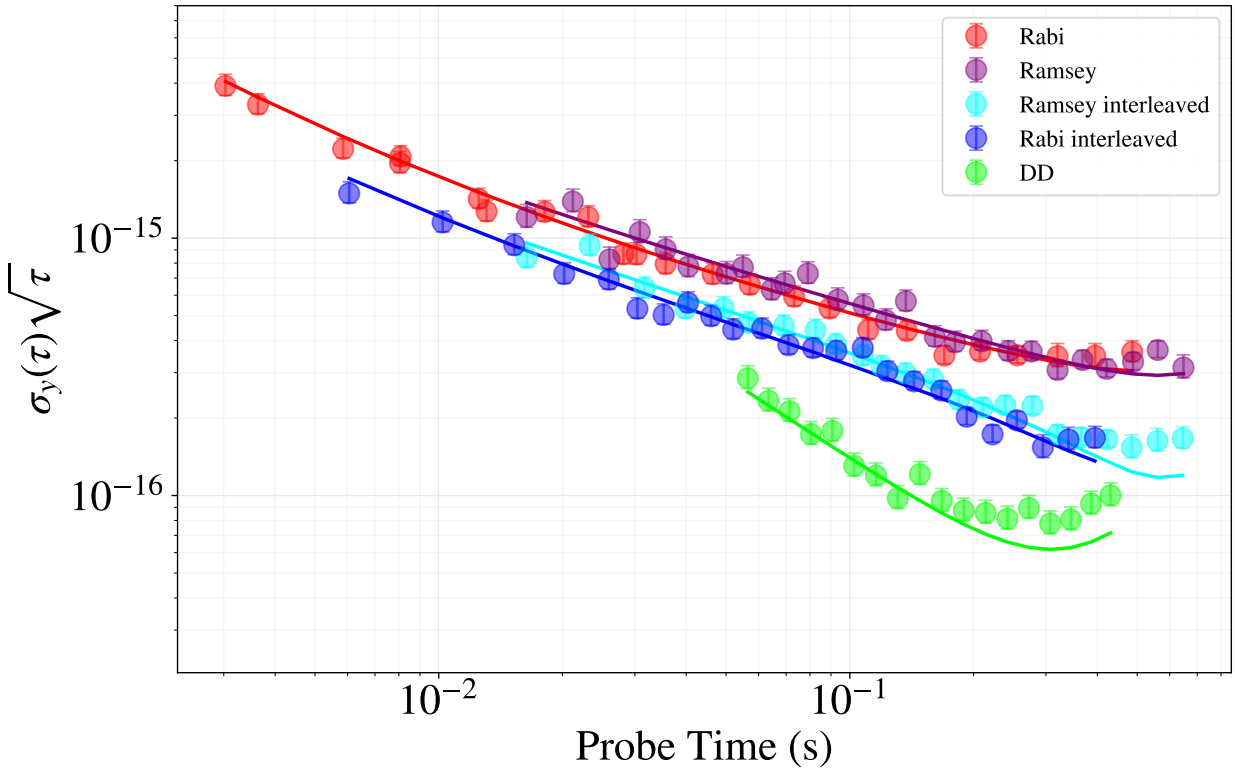

Figure 4.8: **Long-term stability of composite clocks**. The asymptotic white noise limits for the composite clock options described in the main text are estimated through numerical simulations of the clock servo (circles) and through the analytical model (solid lines) described in Chapter 3. The x axis represents the effective probe time calculated as the integrated sensitivity function for a cycle.

multiple flip pulses at the cost of increased instability from the Dick effect. However, by also simulating sequences with 2 and 3 pulses respectively, it was determined that the single pulse case offers the best compromise, though this depends on the laser noise. Furthermore, although according to the model the leading contribution is from the Zeeman shifts, there is a discrepancy between the total instability estimated by the model and the instability of the simulation.

4.2.2 The potential of zero dead time systems

The dynamical decoupling sequence can be used to achieve zero dead time operation with two clocks which do not otherwise have a large enough duty cycle by selecting a low enough sensitivity level. Although the technique does not ensure QPN-level stability for all cases due to the residual LO noise aliasing from sensitivity variations, it nevertheless yields significant improvements. Figure 4.10 shows simulations of zero dead time composite clocks for different levels of LO noise, assuming operation with 650 ms dead time and 10 ms π pulse calibration in each individual clock. A negligible magnetic field noise has been used and the number of atoms was scaled in each simulation so that the stability would be

limited by the residual Dick effect. Considering the case of deployable lattice clocks [100], where cavities with long spacers or cryogenic temperatures are not feasible, a LO with flicker floor at the 8×10^{-16} level was selected, in range with robust cubic cavities values [101]. The best stability was obtained for 6 pulses dynamical decoupling probes reaching a white noise limit of $3 \times 10^{-16}/\sqrt{\tau}$. Such a system would be QPN limited only if the number of atoms would be lower than a modest 30 atoms. For room temperature cavities, similar to those at NPL, the best stability was achieved with single pulse dynamical decoupling resulting in stability equivalent to the QPN effect for 150 atoms. For state-of-the-art cryogenic silicon cavities [47], normal Ramsey interrogations suffice [59] resulting in QPN limited stability if the number of atoms interrogated per cycle does not exceed a few tens of thousands with only a small contribution from the Dick effect which can be eliminated by pulse amplitude.

4.2.3 Differential clock offsets

Another issue to consider when implementing composite interleaved clocks is the frequency offset between the two clocks, which might arise from different uncompensated systematic effects in one or both of the clocks. If a static differential offset is present, the output of the composite clock would be offset by half the difference as each atomic servo would try to steer to their respective resonance. If the offset is due to only one less accurate clock, the resulting composite system would be less accurate than the more accurate clock of the pair. In situations where accuracy is not important, for example when trying to measure time-varying phenomena such as tidal effects, this might not seem like an issue. However, given that the output of the composite clock settles around the midpoint, the two servos will keep trying to correct it in opposite directions, causing a swinging effect that also degrades stability.

One might consider using the error signal in each loop as an indicator of such offsets, since the two clocks should have equal and opposite responses. Simulations confirm this prediction and show that it can be used to track the offsets even if they change with time. However, a complication arises due to the fact that, on average, each clock sees the common centre frequency slightly farther than the midpoint as its measurements occur after corrections from the other clock. This results in the error signals being correlated with the offset but with a scaling factor that is not trivial to predict as it depends on the servo gains and the timings of the corrections.

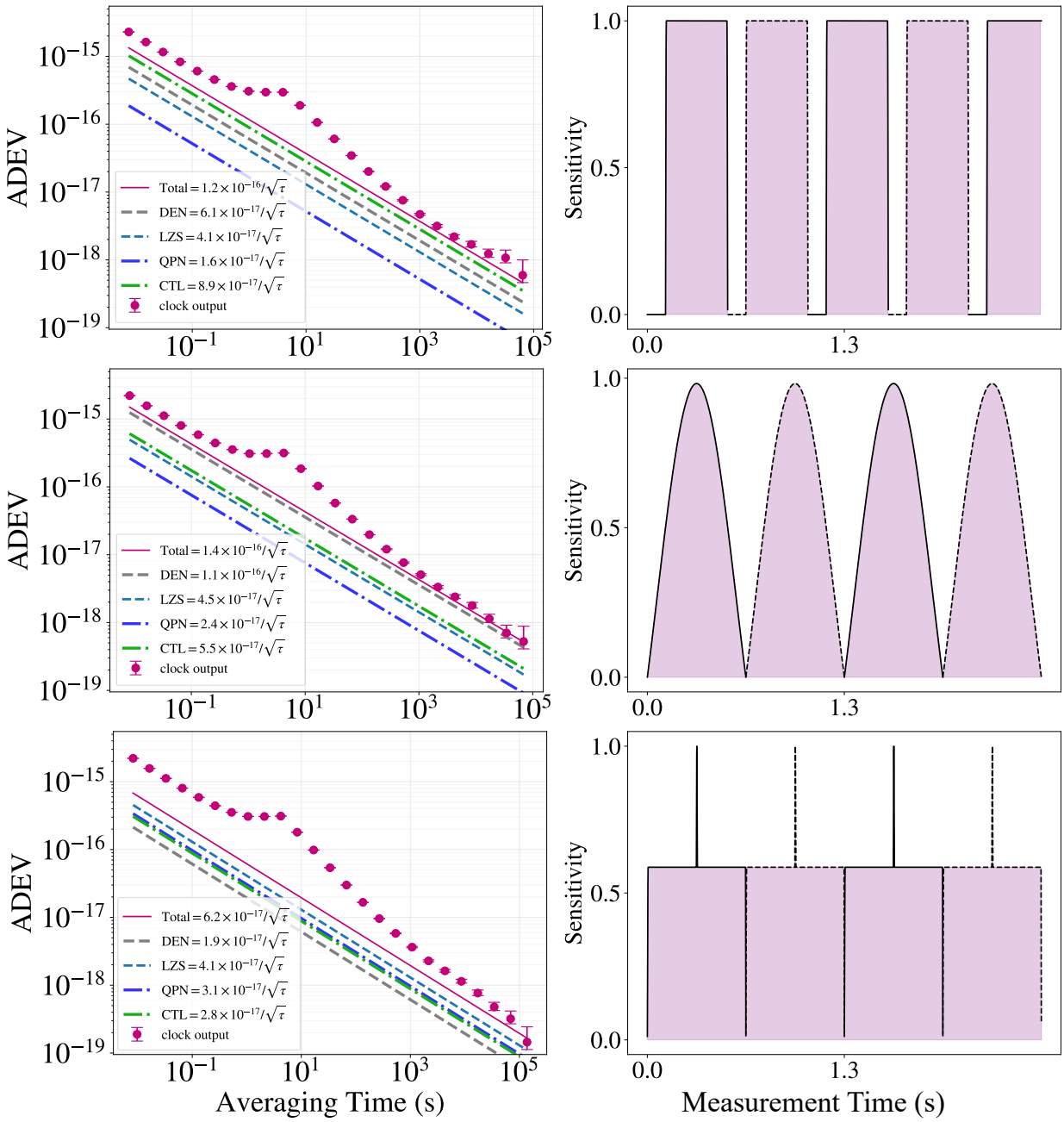

Figure 4.9: **Allan deviation plots for composite clocks**. Individual simulations selected at the optimal probe time from Figure 4.8, shown next to their corresponding sensitivity functions.

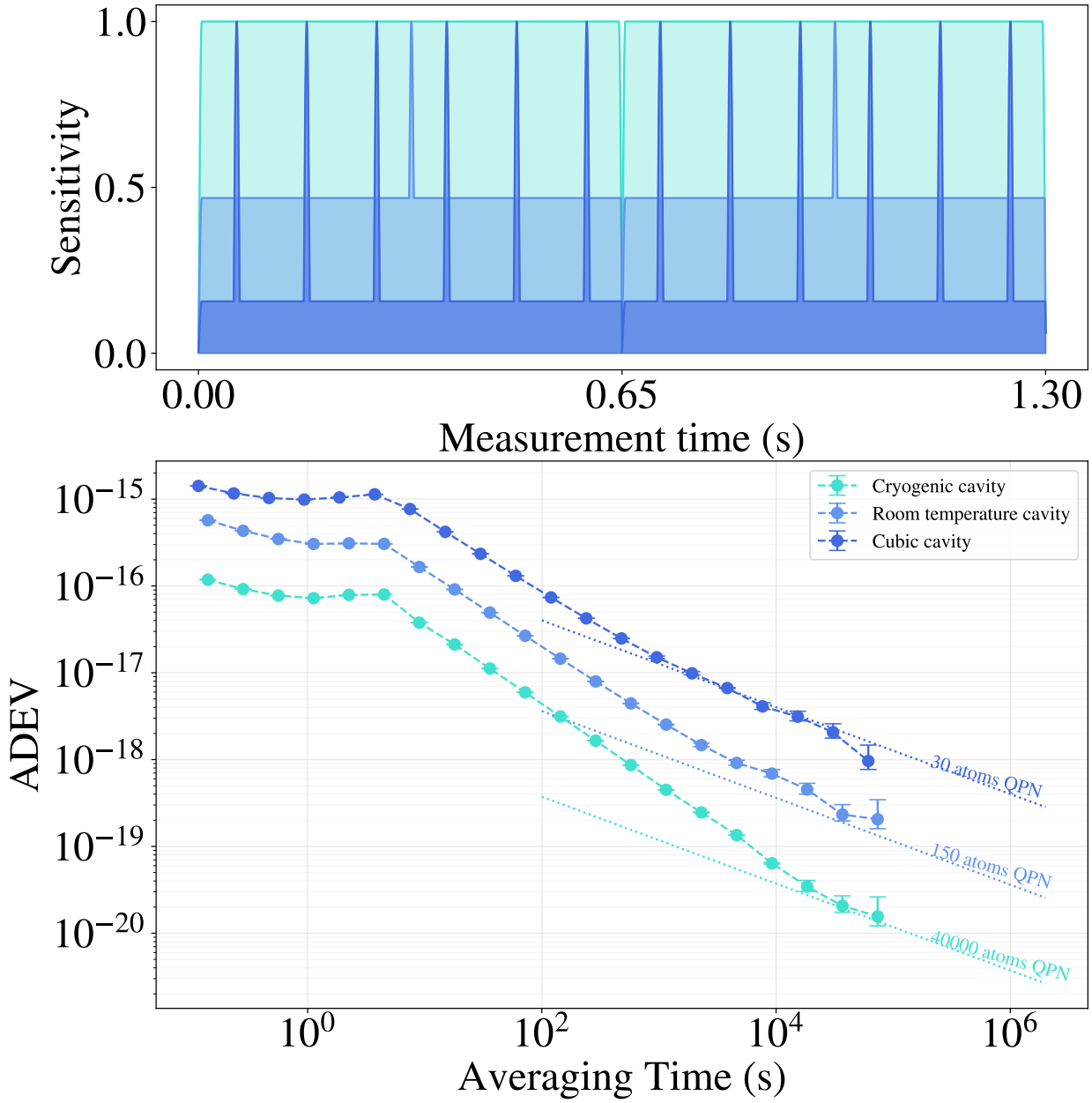

Figure 4.10: **Limits of zero dead time composite clocks** Simulation results for zero dead time composite clocks based on optical cavities with three different performance levels, as described in the main text. The long-term instabilities in dashed lines are also shown indicating the maximum number of atoms for which the clocks are limited by QPN.

Chapter 5

Noise beyond the Dick effect

The zero dead time operation has the potential to suppress Dick noise to below the QPN level. It is therefore relevant to study the other types of noise that would affect the stability of the composite clock. Crucially, the level of the magnetic field noise could prove to be limiting when operating in this regime. In this chapter is discussed our approach to determining and managing these other sources of noise.

5.1 Synchronous operation of Sr1 and Sr2

A straight forward method to quantify the differential noise between two clocks using the same species is to compare the frequencies of their respective servoing AOMs when operating with synchronised spectroscopy times and a shared local oscillator. This makes the laser noise common mode and the resulting frequency difference only sensitive to differential noise between the clocks, arising from detection noise, QPN, magnetic field noise, and residual differential laser noise from uncompensated paths. Our approach to stabilising the path lengths of the clock probe laser is discussed first.

5.1.1 Clock light distribution

For clock operation in general, the optical phase of the clock laser light needs to be stable as it travels throughout the whole link, all the way from the frequency comb used to stabilise the laser to the ultra stable cavity and housed in a separate lab to the atoms in the science chamber. If left unchecked, path length fluctuations caused by mechanical or thermal effects in the fibre or free space optics can produce unwanted and unpredictable modulation of the laser phase.

To minimise this, several path length stabilisation (PLS) loops are employed throughout the link. All the loops are based on the same setup. The light that travels along the relevant path is overlapped on a photodetector with pick-off light that travels a very short path to generate an error signal. This is used to correct the phase through an AOM placed in

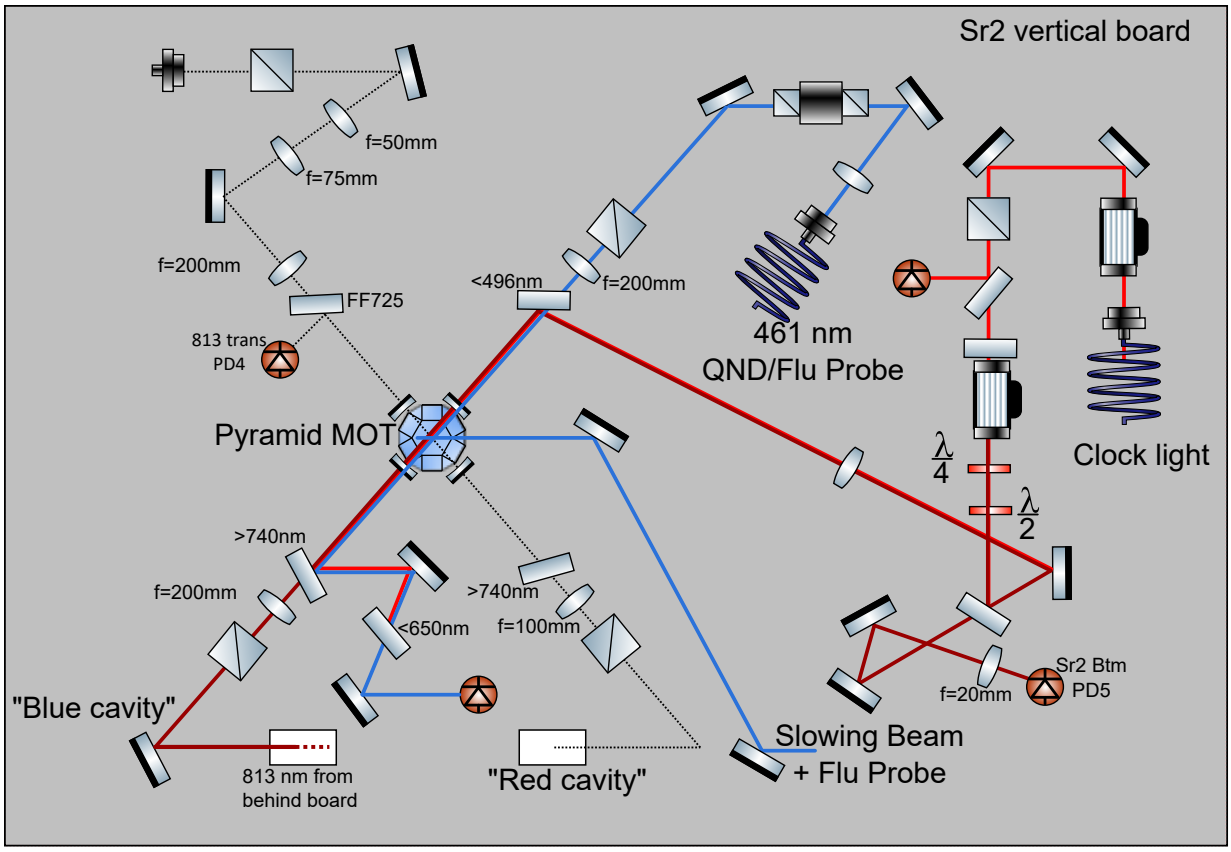

Figure 5.1: **Optical setup around the science chamber in Sr2**.

the long path. The first loop covers the path between the laser and the frequency comb ensuring both that at that point the clock light is stabilised to the comb and that the comb measures the clock frequency without additional phase noise, which is important for clock comparisons. The second path is from the same point to near the science chamber of Sr1, but stops before reaching the atoms. Instead, this final segment from a dichroic mirror to the viewport of the science chamber is implemented by measuring a beat created using the lattice light. Because the lattice light shares the path with the clock probe light for this portion, the corrections are then divided by the 813/698 wavelength ratio and applied to the clock probe. The AOM used for this is the same AOM that detunes the clock probe in the atom servo.

An additional two paths need to be stabilised for Sr2. The clock probe for Sr2 is the undiffracted beam from the Sr1 delivery AOM. Here, the same arrangement is used: a PLS loop is implemented up to the dichroic mirror, after which the lattice is used to feedforward the PLS corrections to the clock probe via the servo AOM. The optics for this are shown in Figure 5.1.

The clock probe AOM implements digital servos by alternating measurements of two Zeeman transition lines and individually tracking the line centres. The lines are usually selected to have opposite Zeeman sensitivities for the determination of the unperturbed centre frequency. To steer the output of the clock (i.e. the light that is sent to the frequency

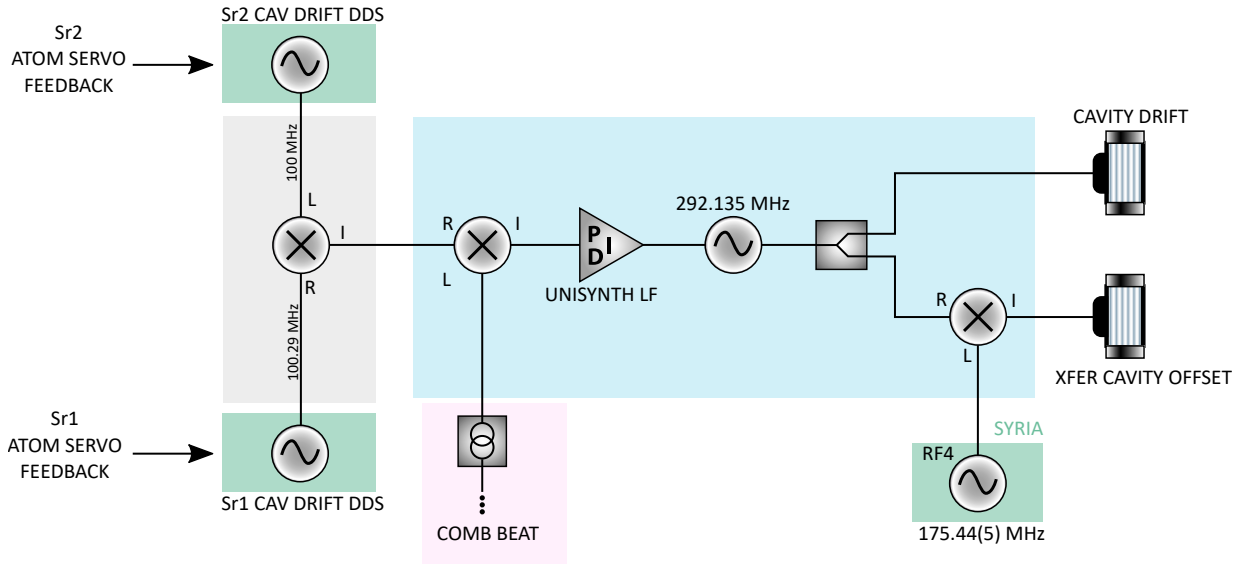

Figure 5.2: **Clock steering with two atomic references**.

comb for absolute or relative frequency measurements) we feedforward the corrections to the cavity drift AOM, which sits upstream of the clock probe AOM. As shown in Figure 5.2, the corrections from Sr1 and Sr2 are combined with the corrections from the comb lock. These modulate a synthesiser that drives the cavity drift AOM thus locking the diffracted light to the ultra stable cavity and to the atomic transition. The same signal is also distributed to the AOM affecting the clock light that is used to lock the transfer cavity ensuring good long-term stability of the lattice and cooling lasers.

5.1.2 Synchronous measurement

The results from the synchronous measurement of Sr1 and Sr2 are shown in Figure 5.3 and Figure 5.4. To perform this experiment, Sr2 and Sr1 were both operated with dead times of 900 ms, Ramsey interrogations with 250 ms dark time, and with 16 ms and 23 ms π pulse calibrations respectively. Although not necessary for the synchronous measurement, we implemented corrections from Sr1 to the shared cavity drift AOM which prevented long-term drifts in the lasers of both clocks. With the digital servos engaged, the centre frequency in each clock was determined from the average of the two Zeeman stretched states π transitions in Sr1 and the two $\pm 9/2$ to $\pm 7/2$ σ transitions in Sr2. Because we interleave four servos with two measurements for each line, the corrections are not distributed uniformly in time, but repeat in patterns of 4 corrections over 8 measurements. Thus, we first average the frequency corrections over such cycles and then estimate the instability through the Allan deviation which shows a white noise limit of $2.7 \times 10^{-16}/\sqrt{\tau}$. The excitation fractions measured in the two clocks show a reasonable degree of correlation with an R-squared coefficient of 0.7. The Allan deviation for the individual frequency corrections from Sr1 and Sr2 are also calculated showing a similar value for both at around $4 \times 10^{-16}/\sqrt{\tau}$. Finally, we also show the self-interleaved comparison between the two pairs

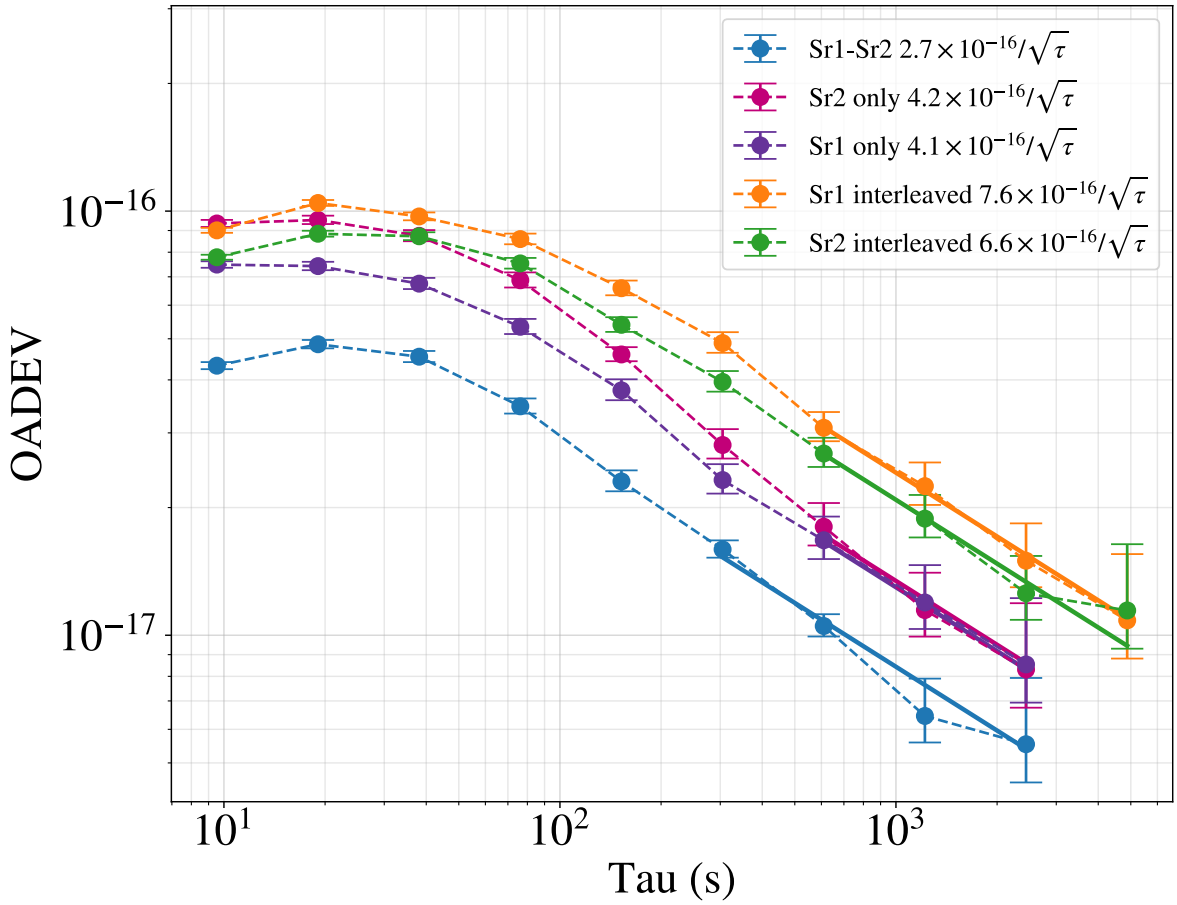

Figure 5.3: **Synchronous comparison of Sr1 and Sr2**. The overlapping Allan deviation of the difference between the corrections of Sr1 and the corrections of Sr2 (blue circles) is computed for synchronised interrogations with a shared local oscillator. Also shown is the overlapping Allan deviation of purely the corrections from Sr2 (pink circles) and of purely the corrections from Sr1 (purple circles). The Allan deviations for the difference between the two servo pairs in Sr1 (orange circles) and the difference of the two servo pairs in Sr2 (green circles) are also shown. Solid lines indicate white noise fits.

in each clock, which has increased Dick effect instability because measurements in one servo pair constitute dead time for the other servo pair.

The long term instability for the synchronous comparison clearly shows rejection of the Dick effect considering the expected instability of 4×10^{-16} for a single clock at this duty cycle, though it is perhaps larger than expected, indicating additional noise in one of the two systems. Due to the Dick noise rejection and the relatively short probe times, the source could be from QPN or linear Zeeman shifts. For this instability to be due to QPN, it would imply that the clocks operate with less than 100 atoms, if both clocks contribute equally, or that one clock operates with less then 50 atoms, if it has a significantly higher QPN instability than the other clock. Both of these cases are unlikely as typical operation involves a few thousand atoms, thus suggesting that the instability is likely to be due to the uncompensated linear Zeeman shifts.

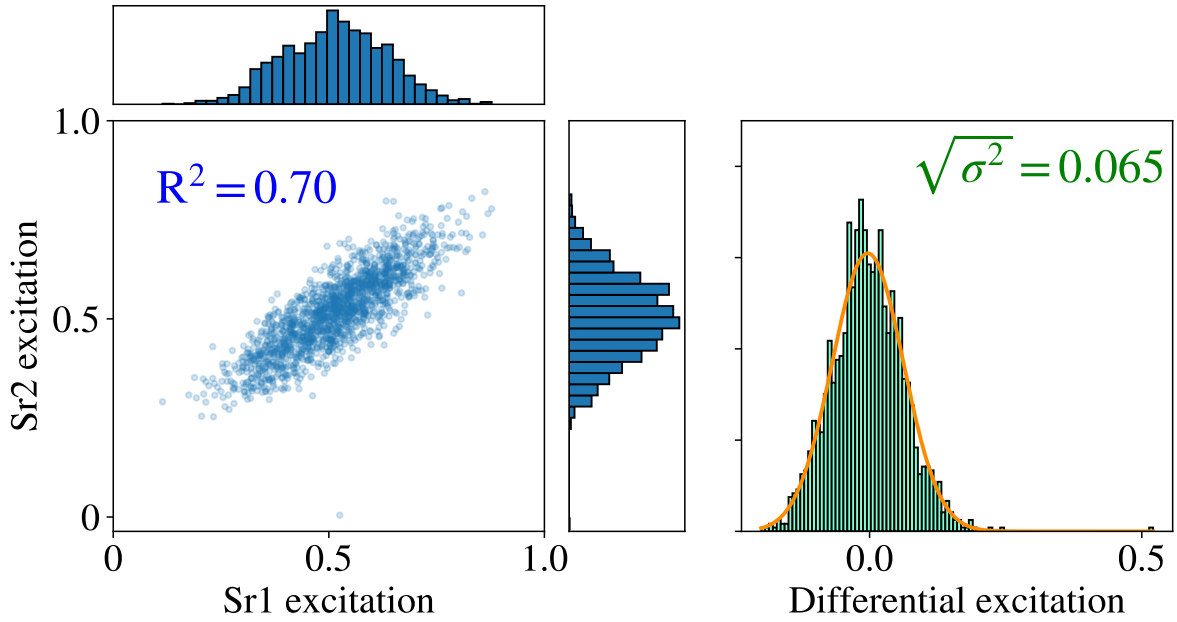

Figure 5.4: **Excitation noise in the synchronous comparison**. *Left*: the atomic excitation fraction measured in simultaneous interrogations in Sr1 and in Sr2 respectively. *Right*: histogram of the differences in atomic excitation fraction between Sr1 and Sr2 fitted with a Gaussian distribution with standard deviation of 0.065.

Indeed, a previous synchronous measurement [64] shows comparable instability and identifies the linear Zeeman shift errors as the limiting factor. Furthermore, the time evolution of the Zeeman splitting in Sr2 (Figure 5.5) shows significant variations over the period of the measurement with an estimated flicker floor of 1.1×10^{-16} and a random walk component of 7.6×10^{-18}. Considering such variations, the theoretical estimate for the linear Zeeman shift errors taking into account the duty cycle is 1.6×10^{-16} without even including any white noise. This makes up a significant portion of the total instability of the synchronous comparison, meaning that the zero dead time composite clock would not be able to improve stability of the single clock if the Zeeman errors would not be addressed first.

5.2 Suppression of magnetic field noise

The nuclear magnetic moment $I = 9/2$ in fermionic Strontium has a paramagnetic effect on the electronic orbitals of the excited clock state which leads to state mixing and a differential g factor between excited and ground states. This causes a corresponding differential Zeeman shift sensitivity of $108.4(4) \times m_F$ Hz/G, as calculated in [44], which means that stray magnetic fields of 2 mG amplitude can cause Hz-level broadening of the line. However, the transitions can be separated by a large enough bias field and probed individually. This allows the cancellation of the linear Zeeman shift to some extent through the probing of states with opposite m_F as discussed in section 3.5.1.

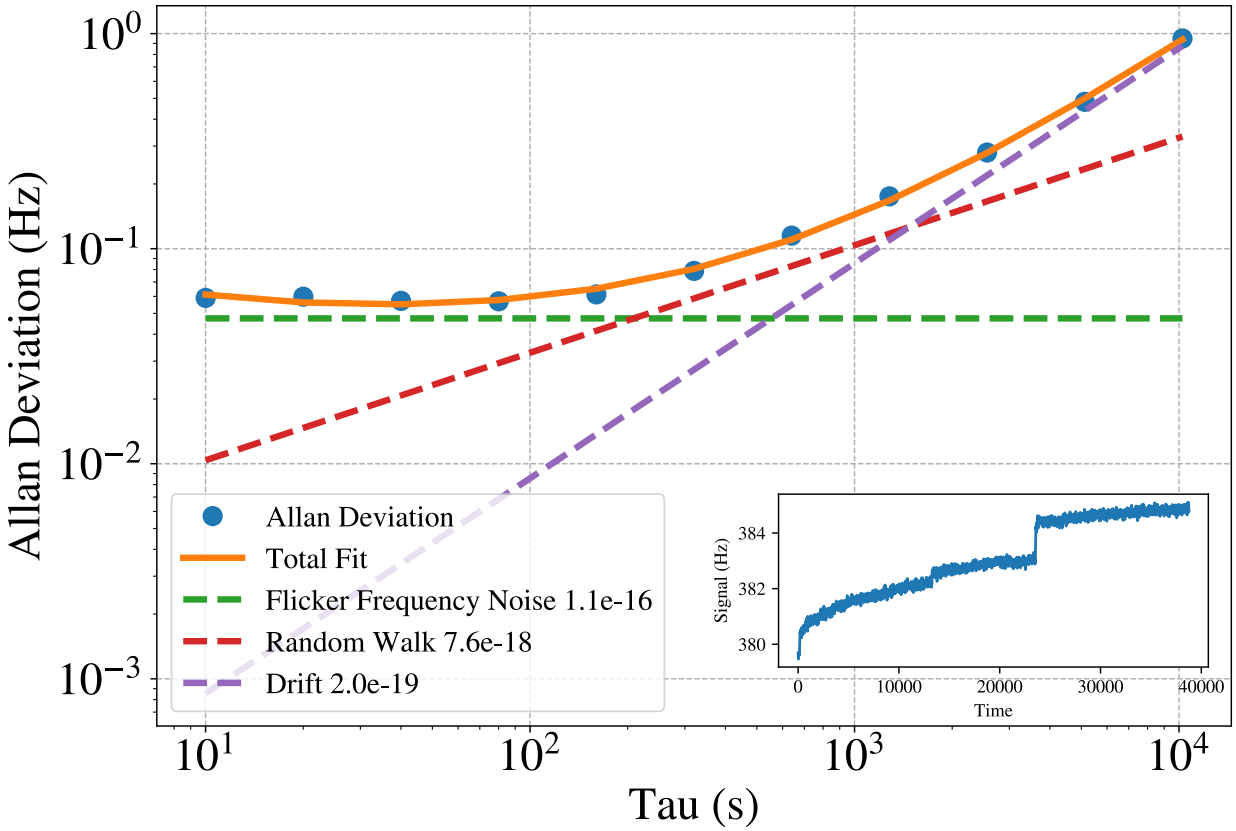

Figure 5.5: **Stability of Zeeman splitting in Sr2.** Allan deviation of the difference between the centres of the two servos in Sr2, logged during synchronous operation with Sr1, with power law fits. Inset: timeseries of the difference from which the Allan deviation was obtained.

The linear Zeeman shift sensitivities for all possible transitions between clock states $|^1S_0, m_F\rangle$ and $|^3P_0, m_{F'}\rangle$ including π transitions with $\Delta m_F = 0$ and $\sigma^{\pm}$ transitions with $\Delta m_F = \pm 1$ have been tabulated in Figure 5.6. Because the ground state hyperfine mixing is small, only the nuclear g factor was used to calculate the shifts for those sublevels, whereas for the excited state the differential g factor from the hyperfine interaction was also added. The transitions involving the $m_F = \pm 5/2$ and $m_{F'} = \pm 3/2$ sublevels have a sensitivity that is 22.3(6) times smaller than that of the $m_F = \pm 9/2$ to $m_{F'} = \pm 9/2$ transitions, thus having the potential to reduce the instability from linear Zeeman shifts to the 1×10^{-17} level.

To verify this, we ran a scan of the clock probe frequency over the clock resonance in Sr1, revealing 28 lines corresponding to 10 π-transitions and 18 σ-transitions. For this measurement, 200 ms Rabi interrogations were used giving a Fourier-limited linewidth of 4.3 Hz. The polarisation of the clock has been rotated away from the normal orientation, which is parallel to the quantisation axis, such that there will be both linear and circular polarisation components. Looking at the resulting atomic response shown in Figure 5.7 observe a good match with the model which confirms the expected sensitivities and is consistent with a magnetic field of 0.67 G. This provides a good motivation for using the

$^1S_0 \setminus {}^3P_0$	-9/2	-7/2	-5/2	-3/2	-1/2	+1/2	+3/2	+5/2	+7/2	+9/2
-9/2	-488(2)	-195(1)								
-7/2	-672(2)	-379(1)	-86(1)							
-5/2		-564(1)	-271(1)	21.9(6)						
-3/2			-456(1)	-162.6(6)	130.3(2)					
-1/2				-347.1(6)	-54.2(2)	238.7(2)				
+1/2					-238.7(2)	54.2(2)	347.1(6)			
+3/2						-130.3(2)	162.6(6)	456(1)		
+5/2							-21.9(6)	271(1)	564(1)	
+7/2								86(1)	379(1)	672(2)
+9/2									195(1)	488(2)

Figure 5.6: **Linear Zeeman shift sensitivities in ^{87}Sr**. Sensitivities for all clock transitions expressed in units of Hz/G.

σ transition instead of the normal operation on the stretched states.

5.2.1 Accommodating lattice tensor shifts

An important implication of addressing different hyperfine sublevels is the tensor polarisability for the light shift due to the optical lattice trap. Ignoring hyperpolarisability effects which have been shown to not surpass the 10^{-18} level for relatively small intensities [102], the total light shift is composed of three contributions from the scalar, vector, and tensor polarisabilities respectively, and for π transitions can be written as [60]

$$\Delta\nu = (\Delta k^s + \Delta k^v m_F \xi \hat{e}_k \cdot \hat{e}_B + \Delta k^t \beta) U_0. \tag{5.1}$$

A good magic wavelength for the lattice is that at which the scalar term cancels the combined vector and tensor terms. The vector shift is strongly suppressed because the opposite m_F numbers of the two lines lead to cancellation of the shift which is already small since the linearly polarised lattice light makes the ξ term zero. Moreover, if the lattice polarisation is aligned with the quantisation axis, the $\hat{e}_k \cdot \hat{e}_B$ product is also 0. The tensor component, on the other hand, is not zero and moreover it depends on the hyperfine sublevel through the factor $\beta = (3\cos^2\theta - 1)\,[3m_F^2 - F(F+1)]$. Thus, the magic wavelength for the magnetic field insensitive transition will be different to the magic wavelength for the stretched states. The angle θ represents the angle between the polarisation of the lattice light and the quantisation axis set by the bias magnetic field. There are two configurations that minimise tensor shift variations due to fluctuations in this angle, namely the orthogonal ($\theta = 90°$) and the parallel ($\theta = 0°$) orientations. This offers a small degree of flexibility in choosing the magic wavelength.

In order to balance the scalar and tensor shifts we need to know the scalar and tensor polarisability coefficients. The differential scalar coefficient has been estimated in [103] at

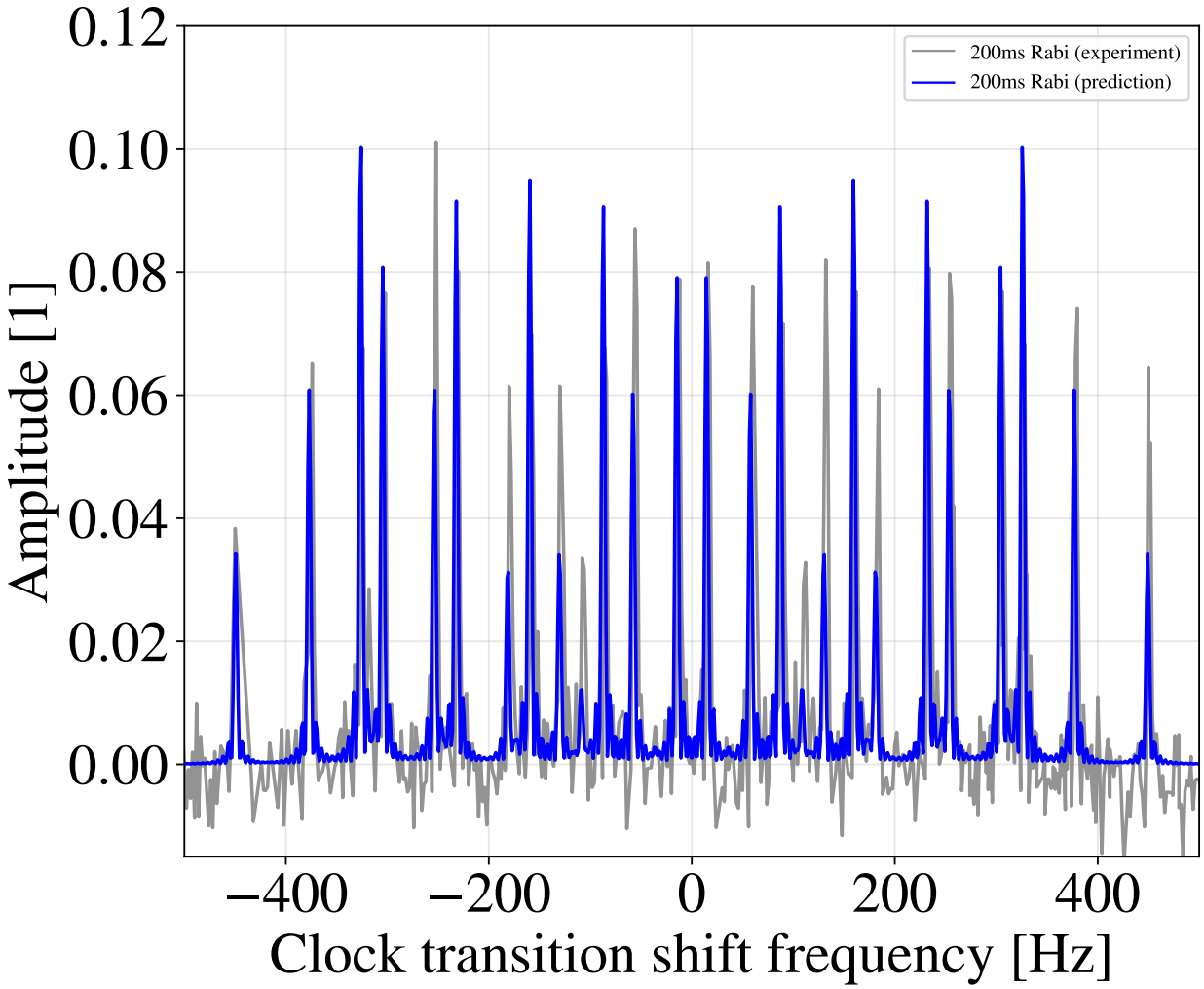

Figure 5.7: **Clock transitions from hyperfine sublevels in ^{87}Sr**. A scan of the clock probe frequency over during repeated π-pulses shows a series of peaks in the atomic excitation amplitude, which match the predicted transition frequencies for π and σ transitions.

$\Delta k^s = -4.73(2)\times10^{-17}\ (\delta/\mathrm{GHz})^{-1}\,\mathrm{E}_{rec}^{-1}$, where δ is a small detuning of the lattice frequency from the scalar magic value and E_{rec} is the recoil energy from a lattice photon. The tensor coefficient has been estimated in [104] at $\Delta k^t = -0.0134(5) \times 10^{-17}\,\mathrm{E}_{\mathrm{rec}}^{-1}$ for transitions between states with the same m_F number. However, to generalise to other transitions, we require knowledge of the ground state tensor polarisability and of the excited state tensor polarisability individually. These were recently estimated at $-6.4(2.7)\,\mu\mathrm{Hz}\,\mathrm{E}_{\mathrm{rec}}^{-1}$ for the ground state and$-61.5(2.4)\,\mu\mathrm{Hz}\,\mathrm{E}_{\mathrm{rec}}^{-1}$ for the excited state [105]. Using these, we can estimate the magic detuning δ for transitions between any m_F sublevels. The values are shown in Table 5.1 for both the orthogonal and the parallel orientations of the lattice relative to the quantisation axis. The differential tensor shift for π transitions on the stretched states in the configuration where the lattice polarisation is parallel to the quantisation axis is $-3967(26)\,\mu\mathrm{Hz}\,\mathrm{E}_{\mathrm{rec}}^{-1}$ which requires a $-195(2)$ MHz correction to the scalar magic wavelength in order to balance the scalar and tensor shifts. For the $5/2 \rightarrow 3/2$ transition,

with the parallel lattice polarisation, the differential tensor shift is $2137(8)\,\mu\text{Hz}\,\text{E}_{\text{rec}}^{-1}$ which requires a correction of 105(1) MHz to the magic wavelength. Alternatively, if the orthogonal lattice polarisation is used, the magic wavelength correction would be $-49(1)$ MHz. Therefore, in order to switch to operation on the sigma transitions, the wavelength needs to be adjusted by 300(2) MHz or 146(2) MHz depending on the orientation of the lattice polarisation.

m_F	$\theta = 0$ **configuration**			$\theta = 90°$ **configuration**		
	β	$\|\mathbf{g}\rangle$	$\|\mathbf{e}\rangle$	β	$\|\mathbf{g}\rangle$	$\|\mathbf{e}\rangle$
9/2	72	-461(22)	-4428(14)	-36	230(11)	2214(7)
7/2	24	-154(7)	-1476(5)	-12	77(4)	738(2)
5/2	-12	77(4)	738(12)	6	-38(2)	-369(1)
3/2	-36	230(11)	2214(7)	18	-115(5)	-1107(4)
1/2	-48	307(14)	2952(10)	24	-154(7)	-1476(5)

Table 5.1: **Lattice tensor shifts**. β factors [dimensionless] and tensor shifts [μHz] for different sub-levels of the ground and excited clock states respectively. For brevity, only the values for positive m_F are shown, with the shifts being invariable under the sign of m_F.

The spectroscopy setups for the two clocks are shown in Figure 5.8a. In Sr1, atoms are trapped in a vertical lattice and interrogated by an upwards propagating clock beam aligned with the lattice. The quantisation axis is set by a bias field constrained to the MOT axis direction which is horizontal. Thus, the relative angle between the quantisation axis and the polarisation vectors of the clock beam and lattice beam respectively can be tuned simply by rotating the respective polarisations with half wave plates. We can thus select any mixture of π and σ components in the clock probe although we cannot independently control the right-handed and left-handed circular polarisation. However, because all the transitions can be resolved we can frequency select specific σ transitions. Because the lattice cavity has a polarisation-dependent finesse, we maintain the $\theta = 0$ configuration. In Sr2, the lattice has a diagonal orientation and the clock probe is overlapped with it propagating downwards. Thanks to the three pairs of compensation coils, the bias field can be rotated in any direction, allowing the possibility of selecting between right-handed and left-handed polarisations through a flip in the sign of the bias field.

Figure 5.8b shows the setup for tuning the lattice frequency. To bridge the 306 MHz tensor shift difference in Sr1, we plan to add a double passed AOM with a range of 55 to 165 MHz for the first order frequency shift. This setup retains the ability to return to the stretched states by turning off the AOM and unblocking the undeflected order. In Sr2, the tuning range is larger thanks to the use of an EOM-generated sideband, so all tensor shifts can be compensated for by tuning the drive frequency of the EOM.

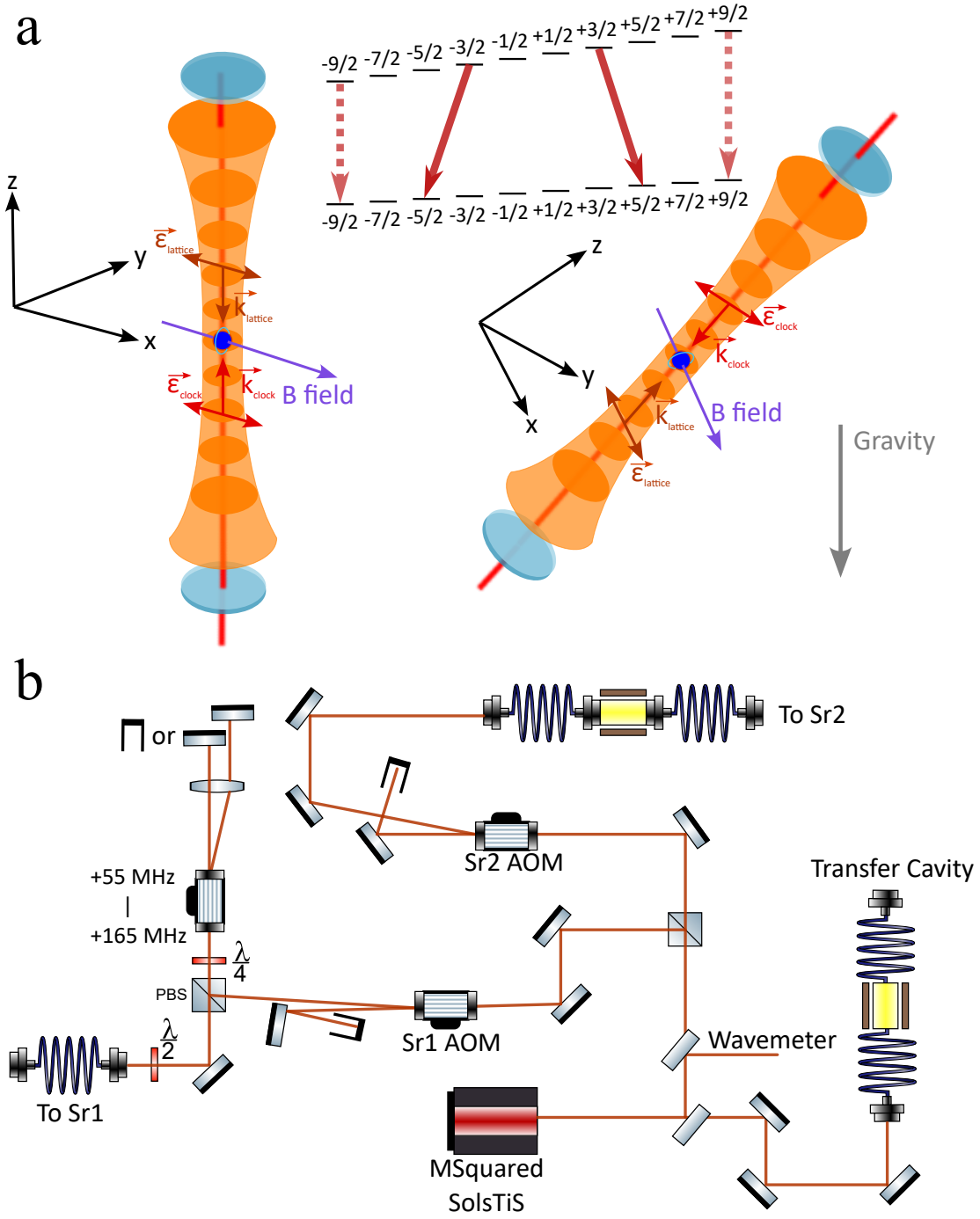

Figure 5.8: **Magic wavelength configuration setup**. a: The Sr1 vertical lattice trap on the left and the Sr2 diagonal lattice trap on the right. Polarisation and k vectors are shown for the clock and lattice light. Sr2 is already set up for σ transitions, whereas in Sr1 this can be achieved by rotating the polarisation of the clock beam. b: The optical setup for tuning the lattice wavelength to compensate for different tensor shifts. In Sr1, a double passed AOM can bridge the 306 MHz difference in tensor shift, having a range of 0 (for the undeflected order) to 330 MHz (for the first diffraction order), while in Sr2 this is achieved by tuning the sideband of the waveguide EOM.

Chapter 6

Yb+/Sr frequency ratio stability with phase feedforward

The growing availability of multiple optical clocks opens the door for composite architectures with superior stability over individual clocks. We have already discussed the zero dead-time optical lattice clock and seen how the interleaved operation of two clocks in conjunction with extended probes eliminates dead-time. In this chapter we discuss a composite system using mixed species of neutral atoms and ions. Motivated by the ambition to measure the frequency ratio of the ion clock to the lattice clock, this discussion shows how improvements in stability can be enabled simply by sharing phase and frequency information from the lattice clock with the ion clock to enhance the local oscillator coherence [106].

6.1 Enhanced laser coherence through phase tracking

Clocks using single ions do not have the issue of dead-time thanks to the deep Paul trap potentials which keeps the ion in across many measurements eliminating the need to spend time preparing a new ion every cycle combined with a much simpler and shorter detection. Instead, ion clocks have large quantum projection noise due to the low rate of information that can be extracted from the single ion. Increasing the number of ions in the trap would require a new trap with a different design [107]. Alternatively, extending the interrogation time could help by narrowing the spectroscopic line and therefore reducing the frequency noise. As in optical lattice clocks, the interrogation time is limited by phase projection errors. Dynamical decoupling sequences cannot help in this case as they only extend the probe time without increasing the discriminator. In fact they would only have a detrimental effect as they would reduce the correction rate.

A possible solution is to use an optical lattice clock to increase the coherence of the LO probing the ion clock. The phase estimation errors in the ion can be prevented by phase corrections from the lattice clock which reduce the differential phase that accumulates during the interrogation of the ion helping to keep it within the invertible range of $[-\frac{\pi}{2}, \frac{\pi}{2}]$

for longer. Thanks to the large number of atoms in a lattice clock, a phase estimate can be obtained with a single measurement. If the two clocks share a local oscillator - or are phase stabilised to the same ultrastable cavity - and their interrogations are synchronised, their phase noise will be highly correlated and the estimates from the lattice clock can be applied to the ion clock. This is similar to the scheme implemented in [65], with the distinction that the phase information is not used in the atomic servo of the ion clock, but rather applied directly to reduce the phase noise of its local oscillator.

6.2 Hybrid clock experiment

The experimental setup illustrated in Figure 6.1 has been implemented to test this method. The Sr and Yb^+ clock lasers are locked to different branches of the optical frequency comb, which in turn is locked to the ultrastable cavity. This produces a high degree of correlation between the fractional frequency noise of the lasers and the cavity. In the Sr lab, the lattice clock performs Ramsey measurements on the Zeeman stretched states deriving estimates of the frequency offset every time the centre of a line is determined with two measurements. To estimate the phase, a single measurement on either side of the line is sufficient given that the linewidth is known. In the Yb^+ lab, the ion clock also performs Ramsey interrogations, probing on each side of a magnetically insensitive transition line with multiple consecutive measurements in order to build statistical estimates of the excitation amplitude. The frequency and phase estimates of the lattice clock, scaled to the wavelength of the ion clock, can be applied to the ion clock by modulating a feedforward AOM in the path of its clock laser. The atomic interrogations are synchronised at the start, but the ion clock takes slightly longer allowing time for atomic detection in the lattice clock to ensure that the phase information from the lattice clock reaches the AOM of the ion clock before the second Ramsey pulse.

The combined stability of the two clocks is characterised through the ratio of their frequencies which provides a measurement that is not limited by the SI uncertainty. We first measure the absolute frequency of each clock by measuring the beat note between the clock laser and different teeth of the same optical frequency comb accounting for all the frequency steps in the RF chain. These two measurements which are noisy due to the referencing of the comb to the hydrogen maser can then be turned into a frequency ratio measurement where the common mode noise is canceled. The ratio has been calculated during two measurements in the first of which only frequency corrections were used and in the second both frequency and phase corrections were used. The stability of the ratio is shown in Figure 6.2 for both situations. The ADEV for short averaging times is smaller than the laser ADEV because it is common to the two clocks and therefore suppressed in the comparison. In both cases, the deviation peaks for times on the order of a few tens of seconds, corresponding to the servo time in the ion clock, after which it starts to average down reaching a long-term white noise limit set by the combined noise from the lattice and ion clocks, normally with a dominant contribution from the ion. The reduced instability in the case when phase corrections are applied indicates that the ion clock stability is improved, since the lattice clock operation is unchanged between the measurements. At

the same time, an increased white noise can be observed for short averaging times.

6.3 Simulations

To make sense of the results in the previous section, simulations with realistic parameters are performed for the servos of the lattice and ion clocks. The lattice clock cycles consist of 650 ms dead time and Ramsey interrogations with 450 ms dark time and 20 ms π pulse calibration. The ion clock cycles consist of 561 ms dead time and Ramsey interrogations with 575 ms dark time and 84 ms π pulse calibration. The noise data generated for the lattice clock is based on the characteristics that were determined and used in Section 4.2, including the Zeeman shifts. To reproduce the correlated noise, the frequency data is scaled and also used for the ion clock.

An additional source of noise that needs to be accounted for is the inter-branch noise of the comb, which arises due to the non-linear fibres and fibre amplifiers used in different branches of the fibre comb [108] to shift the spectrum to the wavelengths of the two clock lasers. However, by using the small leaking signal from the original spectrum, the noise can be detected and compensated in each branch [109]. To verify this, a measurement was carried out to estimate the noise by implementing the setup in a second frequency comb. The two combs were locked to an ultra stable cavity and both had compensated branches for measuring the 698 nm Sr1 clock laser. With the laser locked to the first comb, the measurement of the laser by the second comb would pick up any differential noise originating from the generation of the 698 nm branches.

The stability of the measurement is shown in Figure 6.3, revealing a noise level below $3 \times 10^{-17}/\sqrt{\tau}$ on time scales larger than a few 100 ms corresponding to an order of magnitude noise suppression compared to an uncompensated comb branch. To account for this, independent white frequency noise data sets are added to the two clock lasers in the simulation with a level of $3/\sqrt{2} \times 10^{-17}/\sqrt{\tau}$.

Figure 6.4, shows the stability of the ion clock laser in three different scenarios. When no corrections from the lattice cock are applied, it has the stability of the optical cavity, with a negligible contribution from the comb inter-branch noise. Frequency corrections from the lattice clock suppress the flicker noise, which is replaced by the long-term instability of the lattice clock, mainly set by the Dick effect. The instability is slightly increased for averaging times on the order of the servo time of the lattice clock. The phase corrections add further suppression of noise at intermediate time scales, although at short time scales there is increased white noise. As shown in the inset of Figure 6.4, the phase steps are represented as short spikes in frequency which over long enough time intervals serve to keep the frequency offset small, but on short time intervals just add additional noise.

The stability of the ion clock operating with a stabilised laser can also be estimated through the simulations and is shown in Figure 6.5. The Ramsey time that was used in the experiment is longer than the optimal probe time in the lattice clock, which considering the higher nominal frequency of the ion clock puts the clock in a high CTL condition. Indeed, if the laser is only stabilised to the optical cavity, it is severely limited by CTL. The frequency

corrections which improve the stability of the laser reduce the phase variance resulting in a lower long-term instability, although CTL remains the dominant factor. With the phase corrections included, the CTL becomes negligible and the clock reaches its QPN limit.

To connect the simulations to the experimental results, the frequency ratio of the two clocks is computed for all three cases with the stability shown in Figure 6.6. It can be observed that the frequency corrections alone provide significant improvement at all time scales. The short term stability reflects the improved LO, whereas the servo bump and long-term stability are a consequence of the reduced CTL noise. The additional white noise creeping up at the 1 s interval is due to the comb inter-branch noise. With phase corrections, the long-term stability is further improved, as expected, while the additional white noise can be attributed to the frequency spikes caused by the phase steps in the LO. This feature also appears in our original experimental data, although with a smaller magnitude, a detail which can be reproduced if the phase corrections are scaled by a factor smaller than 1.

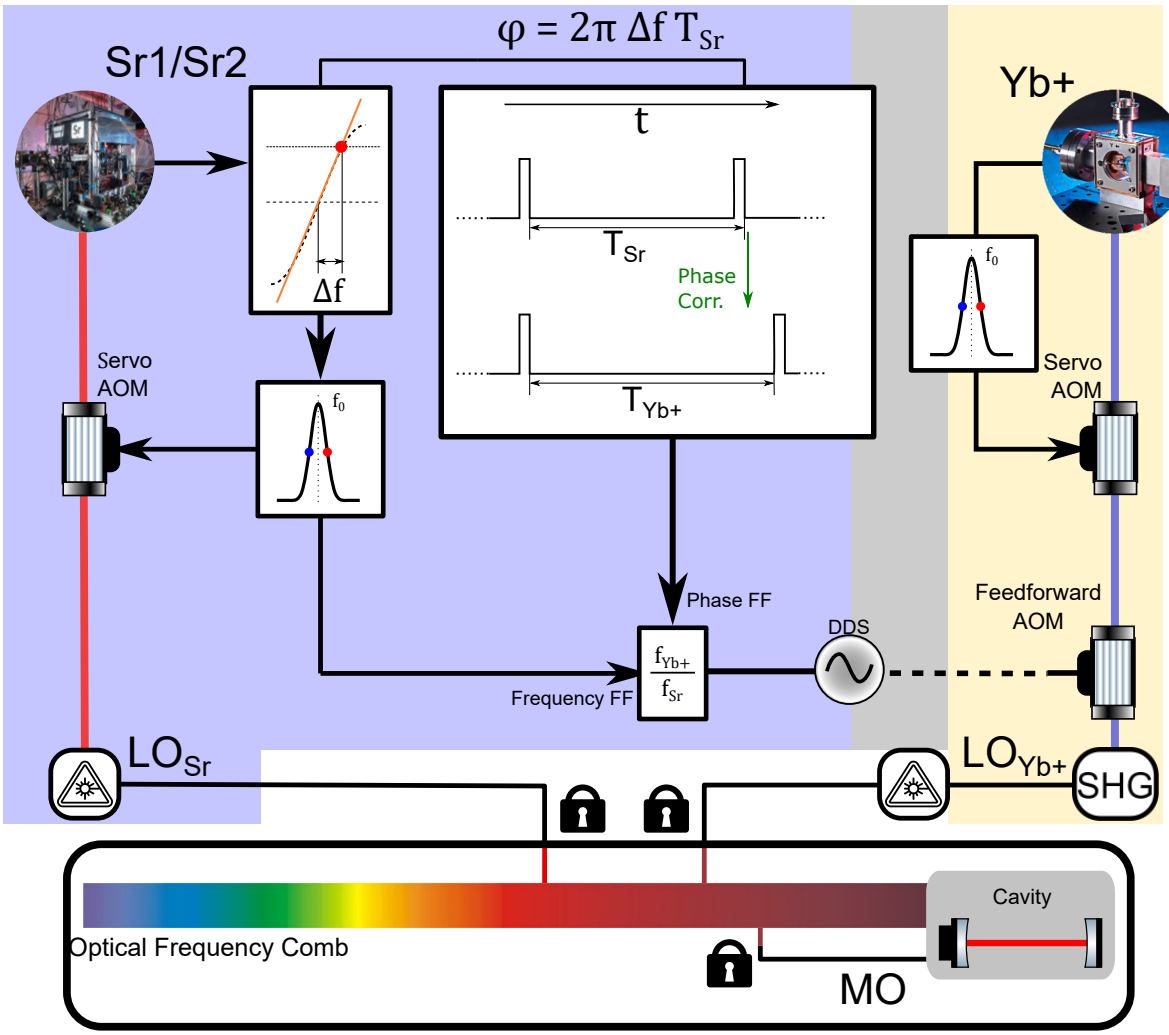

Figure 6.1: **Hybrid clock with phase feedforward**. The Strontium lattice clock (*top left* and Yb^+ ion clock (*top right*) atomic servos steer the two clock lasers which share the stability of an ultrastable optical cavity via an optical frequency comb (*bottom*). Frequency and phase corrections from the lattice clock improve the coherence of the ion clock laser. Probes in the two clocks are synchronised so that the lattice clock samples the same phase noise as the ion (*centre*).

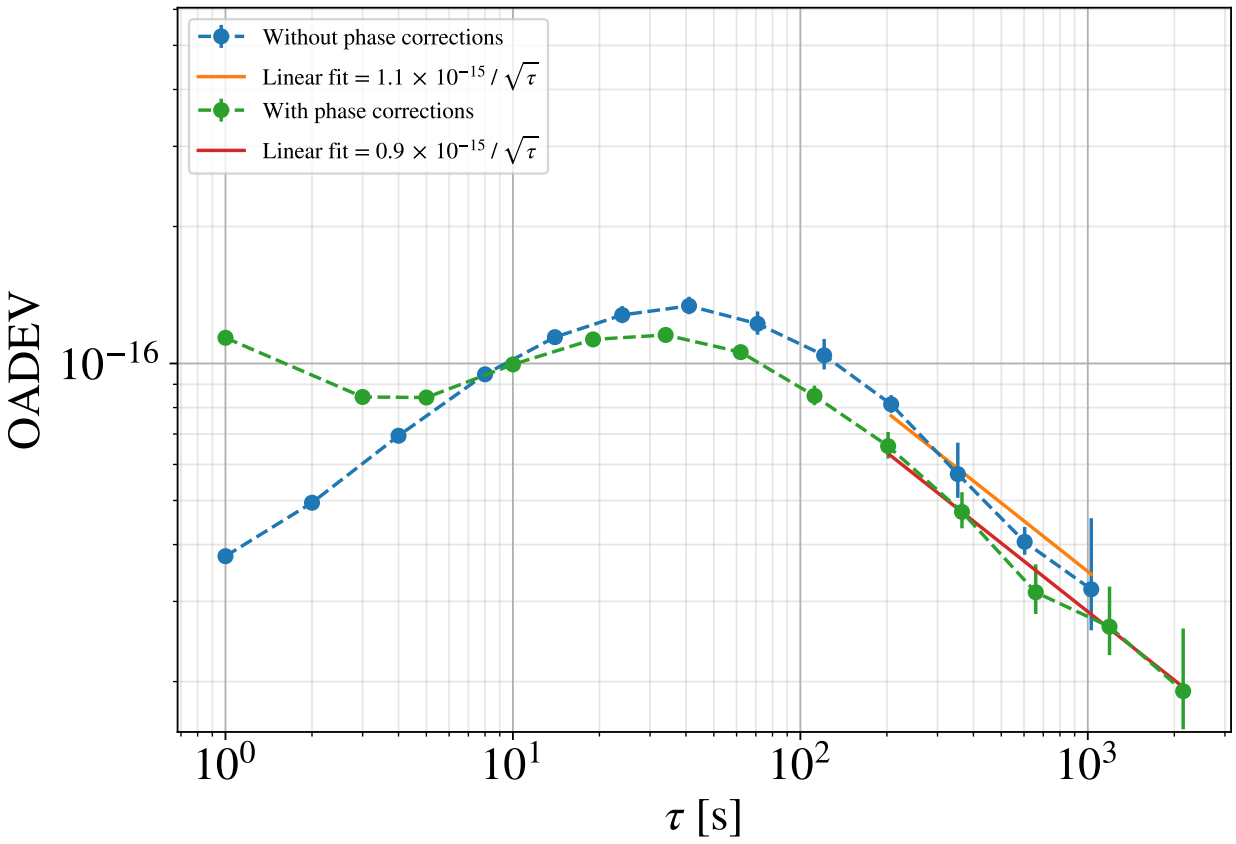

Figure 6.2: **Yb^+/Sr ratio**. Stability of the Yb^+/Sr frequency ratio measured using the frequency comb for the measurement for which only frequency corrections from the lattice clock were applied and for another measurement in which both frequency and phase corrections were applied.

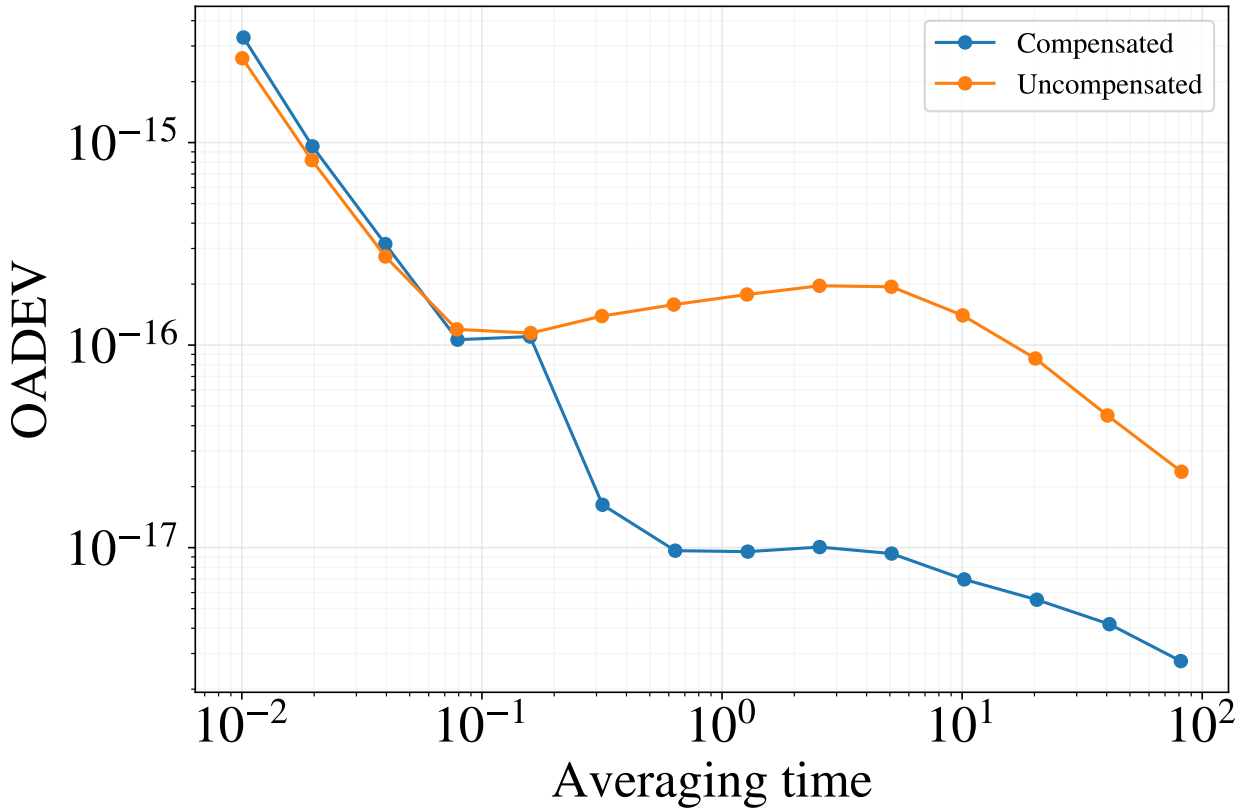

Figure 6.3: **Inter-branch comb noise**. Overlapping Allan deviation of the beat note between the comb-locked Sr1 clock laser and a second comb which shares the stability of the first comb through common locking to the same ultra-stable optical cavity. Measurements are taken with and without the branch noise compensation applied in the second comb.

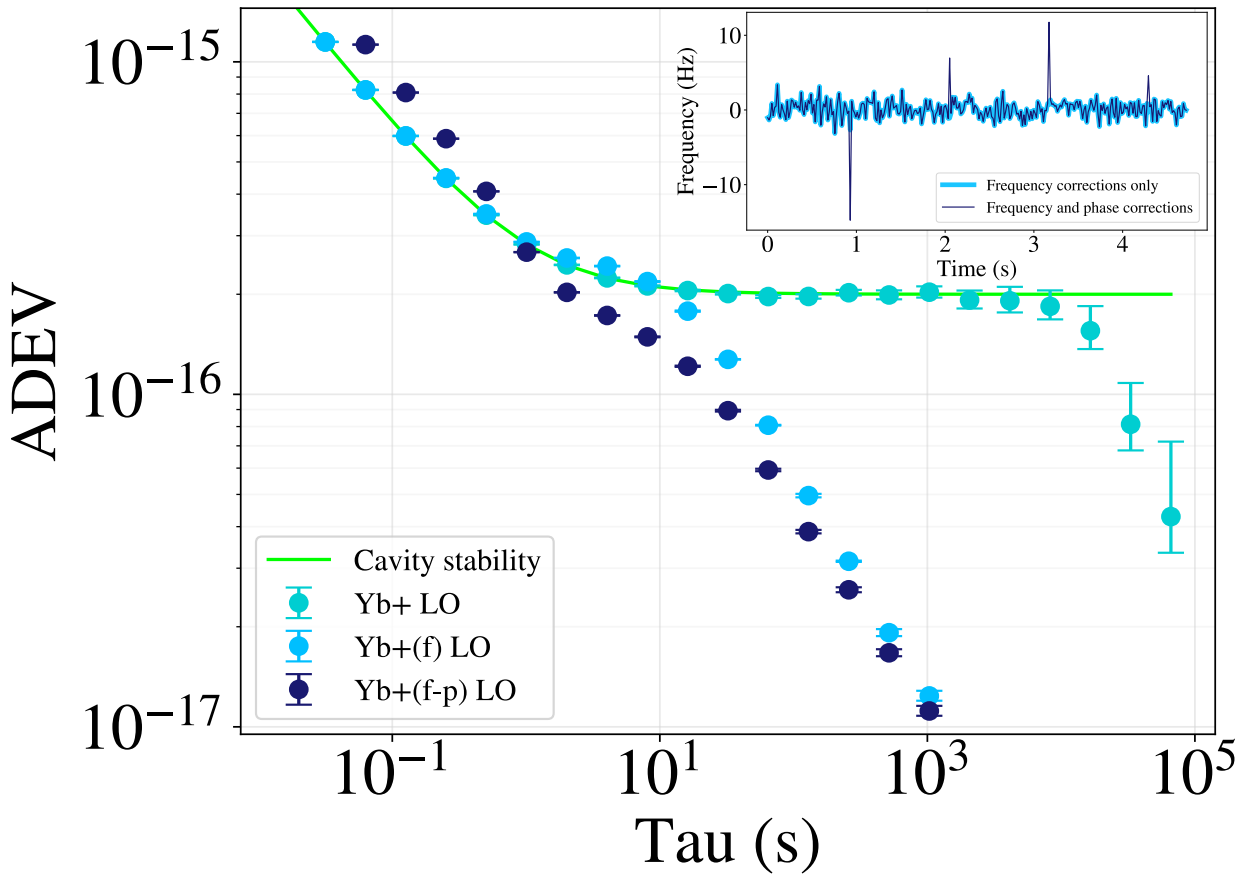

Figure 6.4: **Simulated ion clock laser with frequency and phase corrections**. The overlapping Allan deviation for the noise of the ion clock laser with no corrections, frequency corrections only, and both frequency and phase corrections respectively. Inset: time series sample of the frequency noise for the cases with frequency corrections and frequency + phase corrections.

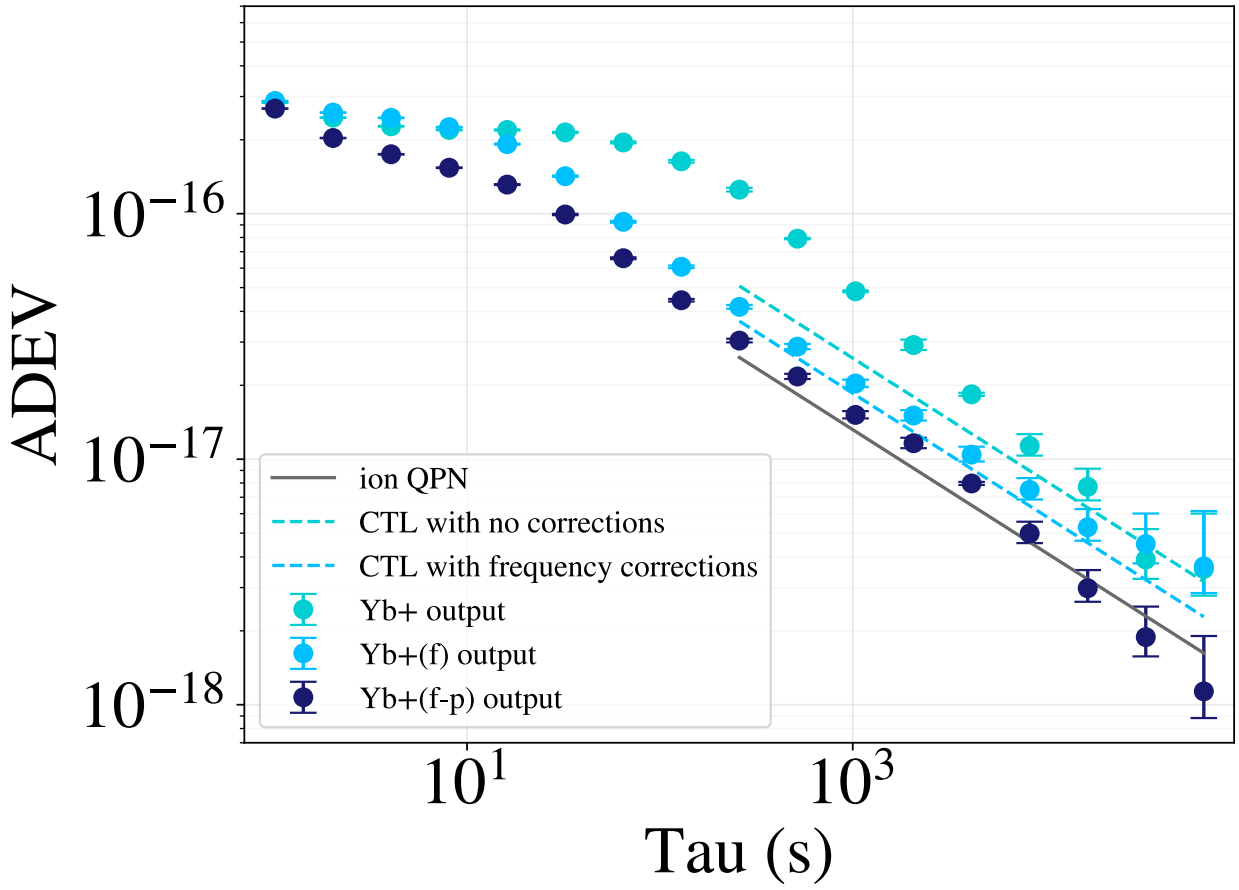

Figure 6.5: **Ion clock stability with phase stabilised lasers**. Overlapping Allan deviation is calculated for the ion clock frequency when it uses a cavity stabilised laser which can have frequency and phase corrections from a lattice clock. Lines show the estimated contribution from QPN, which is the same in all cases, and CTL.

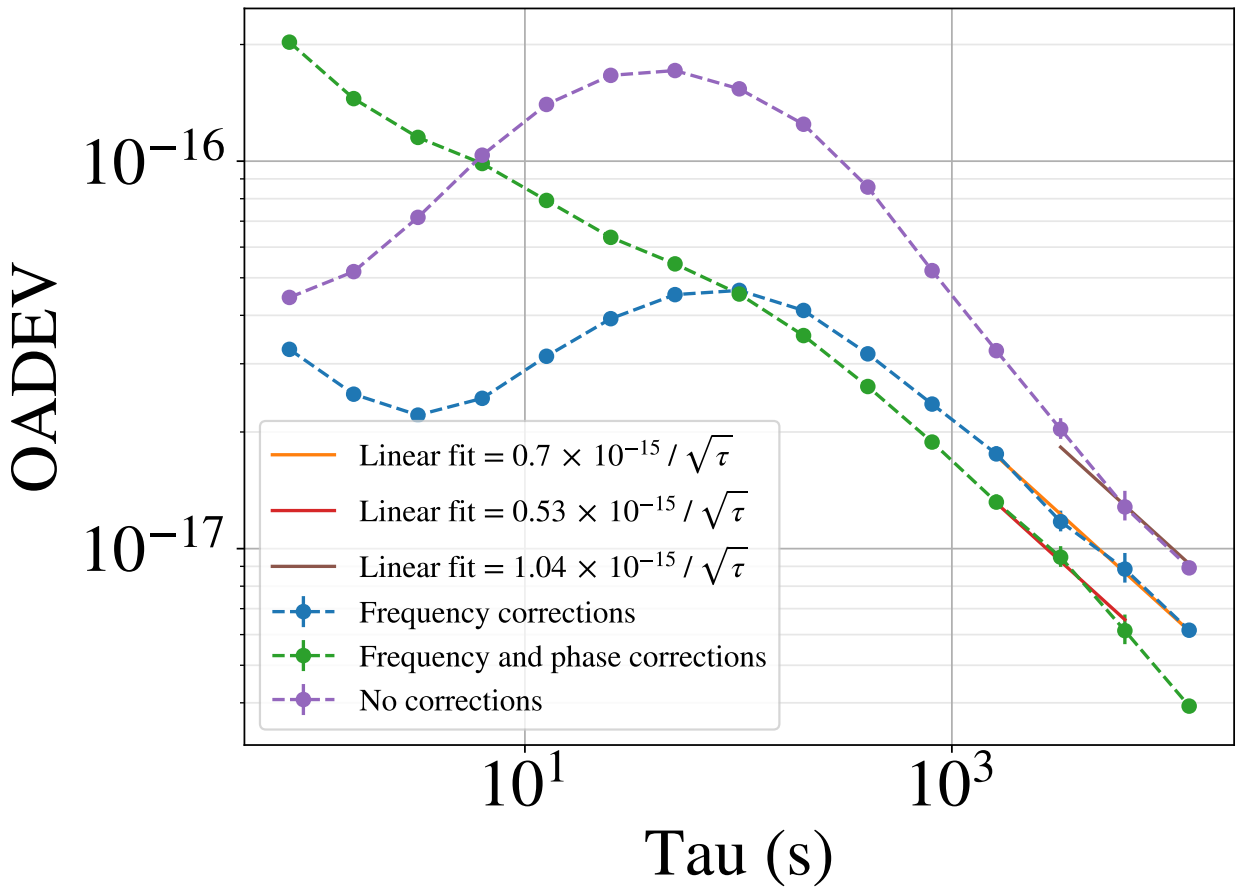

Figure 6.6: **Simulated Yb^+/Sr ratio**. The overlapping Allan deviation for the frequency ratio in the three scenarios discussed in the main text. Linear fits to the long-term asymptotic stability are also shown with their corresponding white noise levels in the legend.

Chapter 7

Dual-tone spectroscopy for rejection of linear Zeeman shifts and continuous interrogation

As argued in previous chapters, the ability to interleave measurements of two atomic ensembles is of great value in reducing the Dick effect. There are, however, two main problems with the zero dead time configuration. The first one is that resources are wasted by having two separate albeit linked laser systems for the two clocks since there is no overlap in their uptimes by virtue of the interleaved nature of the servo. To avoid this, one might consider loading multiple atomic ensembles in the same chamber and probing them at separate times. This would indeed remove the need for separate laser systems and would increase the duty cycle to some degree but would not completely remove dead time.

The second problem is that once we reduce the Dick effect, the magnetic field noise can become a limitation. This is especially true if the $3/2 \rightarrow 5/3$ transition cannot be used, which may be the case if dynamical decoupling probes are employed to get 50% duty cycle. The solution to both of these problems is a conveyor belt clock using dual-tone spectroscopy. Continuous loading of atoms in a moving lattice which transports them to a shielded region allows uninterrupted interrogation of atoms by the clock laser while the dual-tone spectroscopy, which measures both Zeeman transitions at the same time, rejects linear Zeeman shift errors completely. The dual-tone spectroscopy will be discussed first, as a solution to linear Zeeman shifts for clocks operating with normal sequential measurements.

7.1 Dual-tone spectroscopy

The idea of dual-tone spectroscopy is to use two clock beams simultaneously which are spatially overlapped and have different frequencies corresponding to the transitions on the Zeeman stretched states. Atoms prepared with half the sample in each stretched state are then resonant and interact with only one of the two tones provided there is sufficient

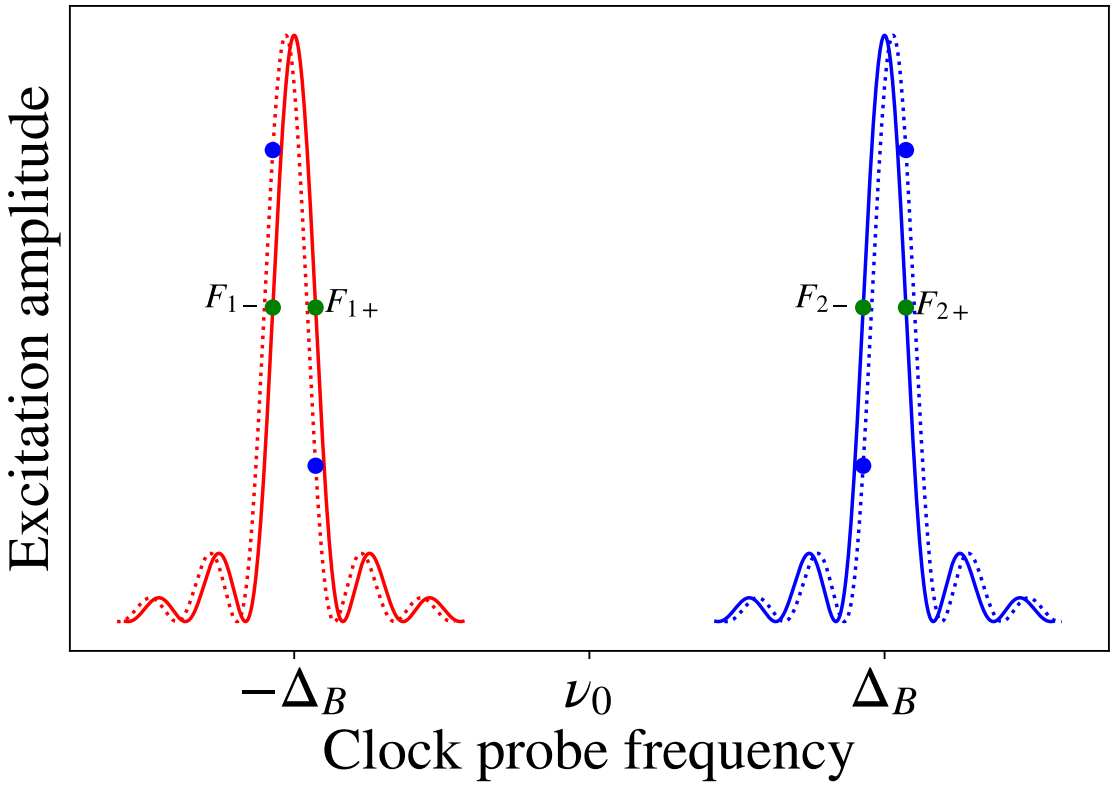

Figure 7.1: **Measurements for servos using two Zeeman lines**. Atomic excitation lines for Rabi interrogations are shown for transitions with opposite linear Zeeman shifts (solid lines). The four measurements required for frequency corrections are shown when resonant (green) and when the magnetic field is slightly larger (blue) shifting the lines outward (dashed lines).

spectral resolution in the clock probe. The increase in the decay rate of atoms due to dual spin populations has been determined experimentally to have only a marginal value [110]. By probing both lines simultaneously instead of in different cycles, the linear Zeeman shift aliasing errors can be eliminated.

7.1.1 Servo structure

To understand how we can lock the dual-tone probe to the centre frequency, we compare it to the standard servo. With the single tone spectroscopy, we need 4 measurements to determine the laser offset from the unperturbed frequency of the clock transition. For each $m_F = \pm 9/2$ to $m_{F'} = \pm 9/2$ line, we implement a servo that finds the line centre by measuring the excitation fractions on the low side of the line, F_-, and on the high side of the line, F_+, as illustrated in Figure 7.1. Each servo tracks the centre of its corresponding line by determining frequency offsets from the imbalance in the excitation fractions for measurements on either side of the line.

$$\delta\nu_l = \frac{F_- - F_+}{2D} \tag{7.1}$$

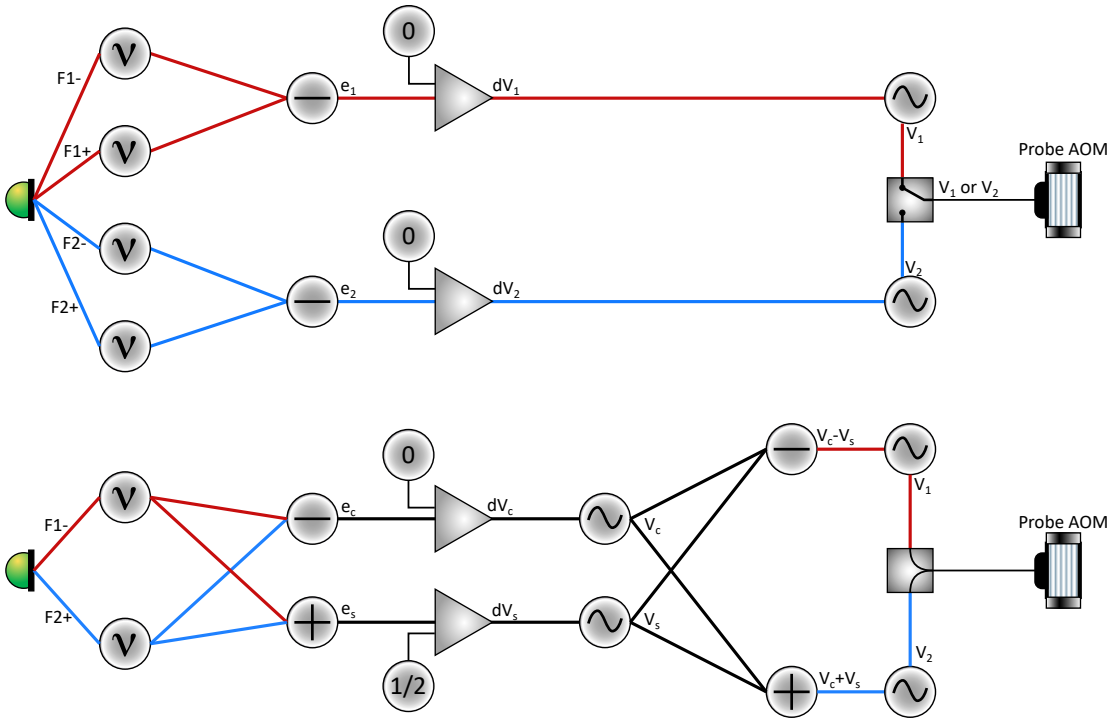

Figure 7.2: **Frequency servo logic**. The structure of the clock frequency servo for standard spectroscopy (top) and for dual-tone spectroscopy (bottom).

This does not distinguish between frequency offsets due to the laser and frequency offsets due to the line being shifted. However, the averaging of the two servos corrects the line shifts, at least to the extent that they are not subject to aliasing errors, giving the unperturbed centre frequency.

$$\delta\nu_c = \frac{\delta\nu_{l1} + \delta\nu_{l2}}{2} \tag{7.2}$$

In the dual-tone method, a single servo is used to find the centre frequency by placing the two tones on the outside of the lines, in other words on the low side of the line that has a negative shift and on the high side of the line that has a positive shift. The centre frequency then is simply

$$\delta\nu_c = \frac{F_{1-} - F_{2-}}{2D} \tag{7.3}$$

This estimate of the offset is completely free of linear Zeeman shifts since they are symmetric in the two lines so will change the excitation fractions by the same amounts. However, the equation is valid only as long as the detuning is close to the half point of the line where the gradient is constant. To ensure this is the case, we need to keep track of the stretched states splitting adjusting the probe detuning accordingly. To do this, we implement another servo whose error signal is not the imbalance of the excitation fractions but the average, adjusting the probe detuning to keep this at 0.5. The offset in our estimate of the splitting frequency is then

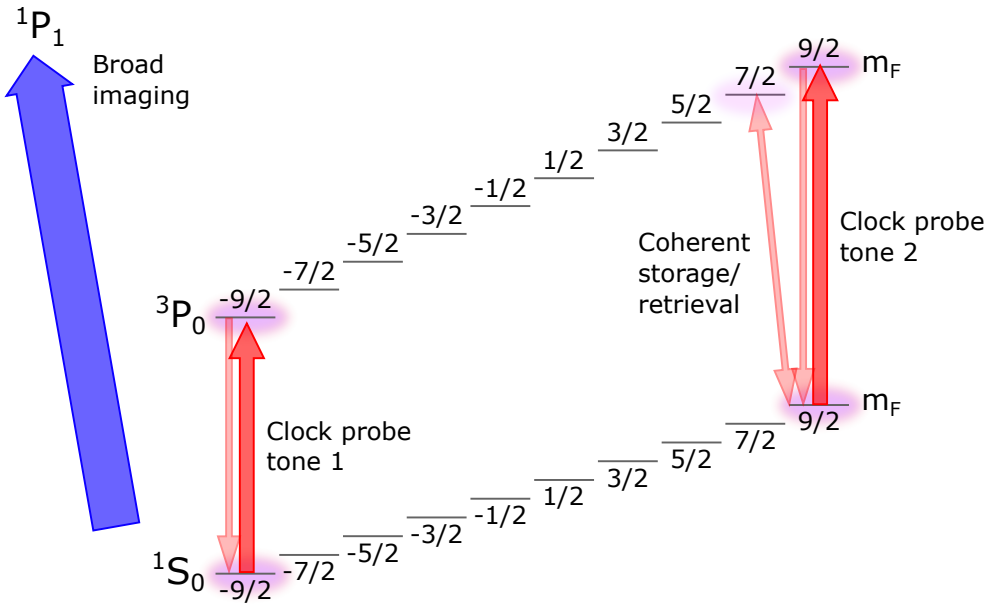

Figure 7.3: **Dual tone spectroscopy and detection**. The relevant clock states and transitions for spectroscopy and readout stage in a dual tone setup.

$$\delta\nu_s = \frac{F_{1-} + F_{2+} - 1}{2D}. \tag{7.4}$$

In both methods, we use two servos, but the single tone method servos each line independently, coupling laser noise and Zeeman shifts, whereas the dual-tone method couples the two lines while independently servoing the centre frequency and the splitting frequency. This is illustrated in Figure 7.2.

7.1.2 Readout stage

The two atomic excitation fractions needed for the dual-tone servo are calculated from the ground state and excited state populations for the two transitions. This requires four images in total, which can be taken using fluorescence on the 461 nm transition. Because of the broad linewidth of the imaging transition, we cannot distinguish between atoms in the $m_F = -9/2$ ground state and atoms in the $m_F = +9/2$ ground state, so only one groud state sublevel can be occupied during each image.

To achieve this, every time an image is taken, all but one of the atomic populations need to be shelved in the excited state, as shown in Figure 7.3. By coherently driving the $m_F = 9/2$ ground state atoms into the $m_{F'} = 7/2$ for storage, the -9/2 ground state atoms can be imaged. This requires a mixed polarisation of the clock probe to be able to address the σ transition for storage as well as the π transitions during spectroscopy. After imaging the -9/2 ground state, the -9/2 excited state can be pumped to the ground state and imaged to get F_{1-}. For F_{2+}, the "9/2 ground state" atoms stored in the 7/2 excited

state need to be retrieved with another σ pulse and then imaged, and similarly for the 9/2 excited state atoms.

7.1.3 Immunity to external magnetic fields

The stability advantage of the dual-tone spectroscopy is estimated here through a series of simulations. We consider four cases: a single lattice clock with dead time using standard spectroscopy, a lattice clock with dead time using dual-tone spectroscopy, a zero dead time composite clock using standard spectroscopy and a zero dead time clock using dual tone spectroscopy. We use a laser noise model based on state-of-the-art cryogenic cavities such as the one in [47] with 4.2×10^{-17} white noise and 4.9×10^{-17} flicker noise components of the fractional frequency instability. We consider linear Zeeman shifts with a flicker frequency noise profile with a range of amplitudes.

The results are plotted in Figure 7.4. Because the stability depends on the probe time, with the optimal value expected to depend on the magnetic field noise and type of spectroscopy, we simulate a range of probe times and select the lowest instability value for each case. For low field amplitudes we see the performance of the two spectroscopy types converge as the linear Zeeman shift errors are less significant. The single clocks asymptote to the Dick noise limit, while the ZDT clocks asymptote to the QPN limit. As the field amplitude increases, the instabilities of the clocks using standard spectroscopy increase, whereas the instabilities of the clocks using dual-tone spectroscopy is largely unaffected for amplitudes $< 3\times10^{-17}$. At larger amplitudes, the stability degrades even for the dual-tone spectroscopy. This coincides with the optimal probe time decreasing as shown in the inset of the figure. Although the coherence of the clock laser does not change, the unstable line contributes phase noise leading to a higher CTL. However, the instability increases at a lower rate in the dual-tone clocks such that at high enough field noise, the instability of the zero dead time clock using standard spectroscopy is almost higher than that of a single clock using dual-tone spectroscopy.

7.1.4 Servo feedback rate

As the number of optical clocks increases and the performance of optical cavities improves making zero dead time composite clocks achievable, the short to medium term stability where laser noise is suppressed as $1/\tau$ before reaching the long-term white noise limit becomes more significant [111]. Here, the simultaneous measurement of the two lines in the dual tone servo would provide an advantage. The four measurements required to determine the centre frequency in a normal clock increase the attack time of the servo. However, there are different ways to improve that.

Results from simulations of zero dead time clocks using different servo configurations are shown in Figure 7.5. The clocks using the slowest servo make a correction only after both lines have been measured thus having the worst stability at the relevant timescale. Clocks making a correction after the estimation of each line instead show a slight improvement in the attack time without compromising long-term stability, as discussed in Section 3.5.1. A

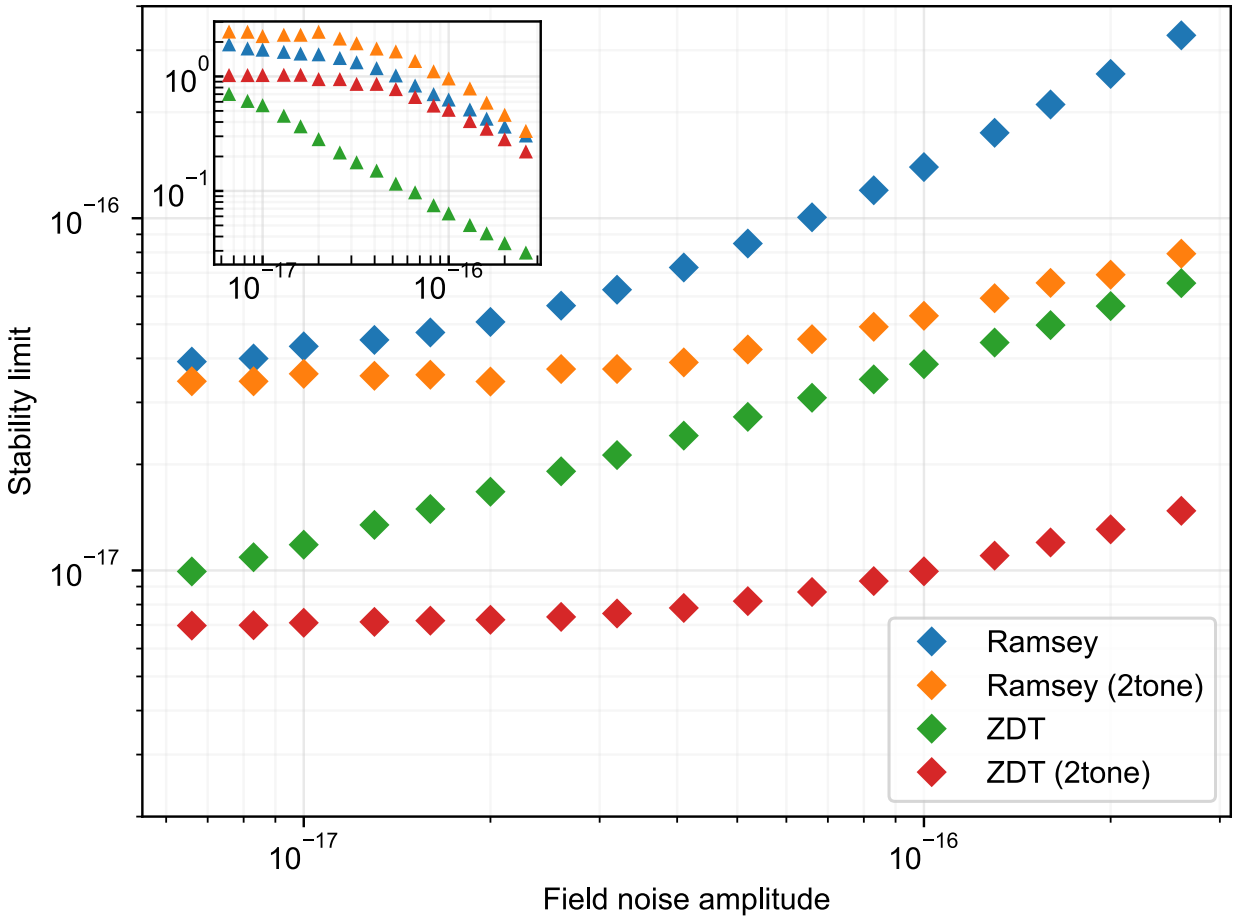

Figure 7.4: **Rejection of Zeeman shift errors with dual tone spectroscopy**. Simulations of limiting clock instability against amplitude of linear Zeeman shifts for a single clock using Ramsey spectroscopy, a single clock using dual tone Ramsey spectroscopy, a zero dead time clock using Ramsey spectroscopy, and a zero dead time clock using dual tone Ramsey spectroscopy respectively. The limiting cock stability for each field amplitude value is foud by repeating simulations with different probe times and selecting the lowest stability at the optimal probe time (shown in the inset).

further improvement can be made by applying both probes for a line in succession before switching to the other line to generate the correction even quicker, although this comes at the cost of increased linear Zeeman errors as discussed in Section 3.5.1. Finally, clocks using the dual tone servo show the best $1/\tau$ instability.

7.2 Continuous interrogation of atoms in a moving lattice trap

The conveyor belt lattice clock which uses a moving lattice to achieve continuous loading and interrogation of atoms has been first proposed in [112]. ^{88}Sr atoms are continuously

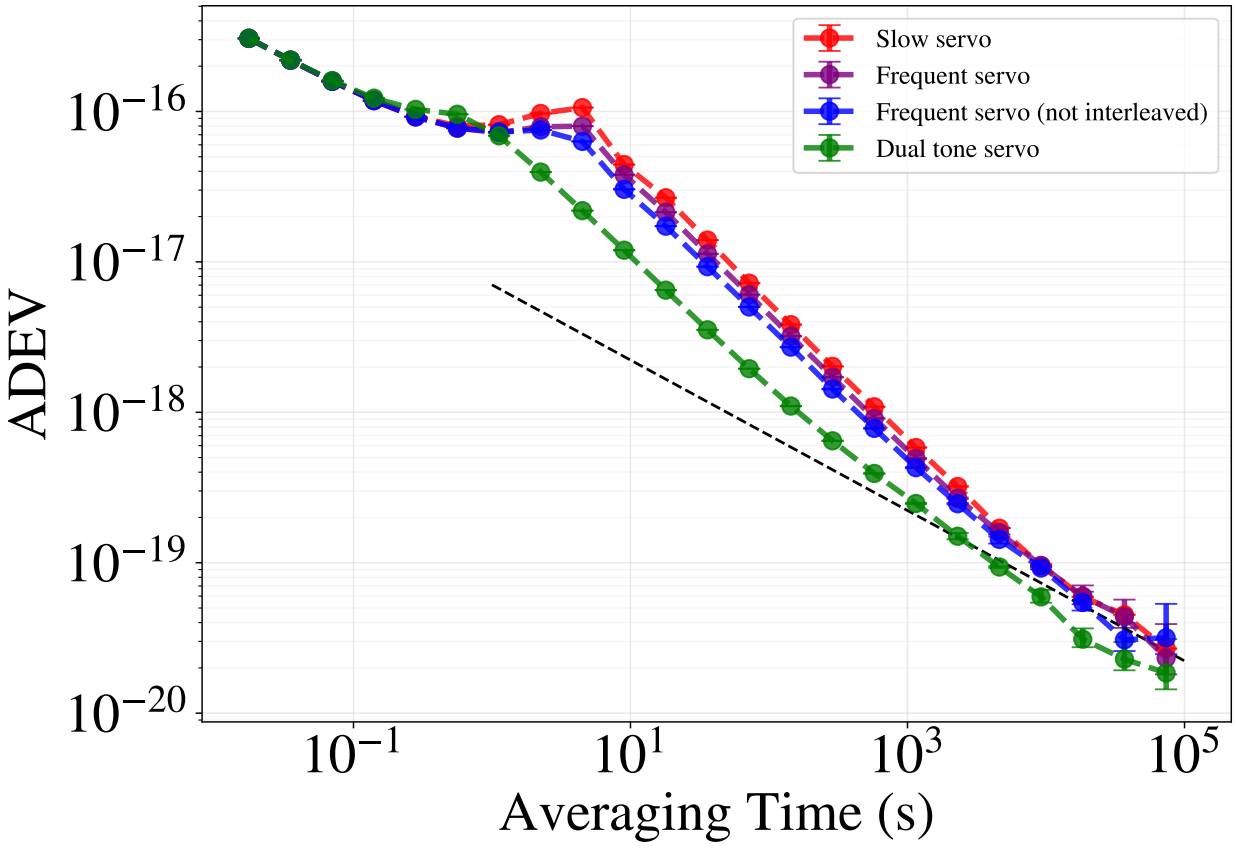

Figure 7.5: **Rate of servo corrections**. The Allan deviation is plotted for simulations of different servos described in the main text showing their different $1/\tau$ averaging lines. All simulations are for zero dead time clocks with Ramsey probes, are limited by the QPN instability for 5000 atoms, use a servo with a first integrator gain of 1, and have no magnetic field noise.

loaded in a moving lattice [113] producing an array of trapped cold atoms. To shield the atoms from the cooling laser light, a crossed lattice configuration has been proposed [114] to transport the atoms in an orthogonal direction to the initial moving lattice direction. This section covers the theoretical discussion of the spectroscopy stage in view of the stability advantage, considering the dual tone interrogation method.

7.2.1 Sensitivity function

The main advantage of the continuous clock stems from the uninterrupted flux of cold atoms to the interrogation region. A smooth sensitivity function can be achieved by constant interrogation of the atoms by the clock laser. A standard imaging technique based on fluorescence on the 461 nm transition results in a quasi-continuous feedback signal discretised by the period needed for imaging. Due to the movement of the lattice, neighbouring groups of atoms will sample overlapping segments of laser noise. In Figure 7.6, the combined sensitivity function that results from this is shown.

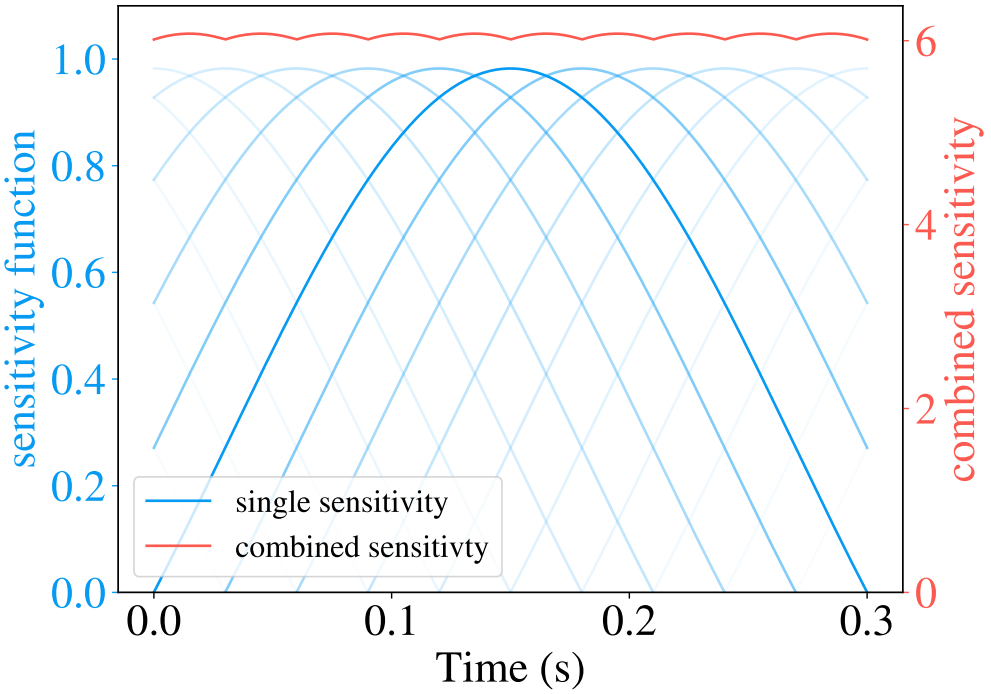

Figure 7.6: **Sensitivity function of the conveyor belt clock**. The combined sensitivity function (red) is the result of multiple Rabi sensitivity functions overlapped with different offsets.

In this example, Rabi interrogation has been chosen with an interaction time of 300 ms given by the combination of the interaction region length and the transport velocity. The resulting sensitivity is much smoother than that for a single 300 ms Rabi pulse. The imaging for the detection stage, occurring every 15 ms, determines the overlap, with shorter detection periods leading to smoother sensitivities. The integrated sensitivity has also a higher level due to the overlap which has the effect of increasing the servo gain, and needs to be accounted for to avoid oscillations in the servo. To account for it, one only needs to determine the number of detections that occur within the time interval for the atom-light interaction.

7.2.2 Zeeman-shift enabled spectroscopy

The continuous interrogation requires that the clock probe is always on and overlapped with the atoms. Moreover, it needs to be aligned with the lattice for good confinement. To be able to control the clock pulse area, the frequency is detuned so that it can only drive the transition in a spatial region where a static magnetic field shifts the clock transitions into resonance with the two tones. In current operation of the sequential clock, we use bias magnetic field corresponding to a stretched state splitting of 650 Hz. If the two tones are set to the frequencies of the stretched states, they become far off-resonant outside of the magnetic field region as the Zeeman spectrum shrinks to a single line at the centre frequency. This strongly suppresses the Rabi frequency outside the magnetic field region,

thus allowing the interaction time to be well defined by the size of the magnetic field region and the lattice transport velocity.

Ideally, the magnetic field would be zero outside the interaction region and uniform inside the interaction region. However, this does not correspond to realistic magnetic field shapes. The magnetic field from a pair of rectangular coils has been calculated and is shown in Figure 7.7. Within the bounds of the coils the field along the central axis is relatively uniform and aligned mostly with the x axis. However, there are imperfections in the field near the edges. To minimise edge effects, the pair of coils should have a tubular aspect ratio. In this example, the length of the tube is 20 cm, with a height and separation between coils of 2 cm each.

With a current of 2 A through the coils, fields of about 0.8 G are produced inside the tube, resulting in a spin stretched state splitting of around 180 Hz. Figure 7.8 shows the relative detuning between the blue detuned tone of the clock probe and the positive stretched state transition. Outside the area of the coils, the probe is off-resonant, so it cannot drive the clock transition, and the leaked field near the edges only pushes the detuning farther. Inside the tube, the transition becomes resonant with the probe driving atomic excitation. The resulting lineshape shows an asymmetry due to the combined varying magnetic field and varying sensitivity of the Rabi spectroscopy. This effect could be reduced by using a more extreme aspect ratio for the geometry of the coils or by using Ramsey spectroscopy with two small magnetic field regions.

The asymmetry is not, in fact, a critical issue since it does not cause a shift in the center frequency because the clock beam probing the negative stretched state will have the opposite detuning and thus the asymmetry will be reversed.

7.3 Clock instability simulations

To illustrate the performance of a continuous clock using dual tone spectroscopy, the atom servo is simulated for a cubic cavity design which has flicker noise at 8×10^{-16}, with the results shown in Figure 7.9. The instability profile is much simplified with only QPN and CTL terms remaining. The QPN is determined from the interaction time, which in this simulation is 100 ms, and the number of atoms measured per second, which in reality is limited by the loading rate into the moving lattice and the transport efficiency. The CTL has contributions both from the laser noise and the external magnetic field noise.

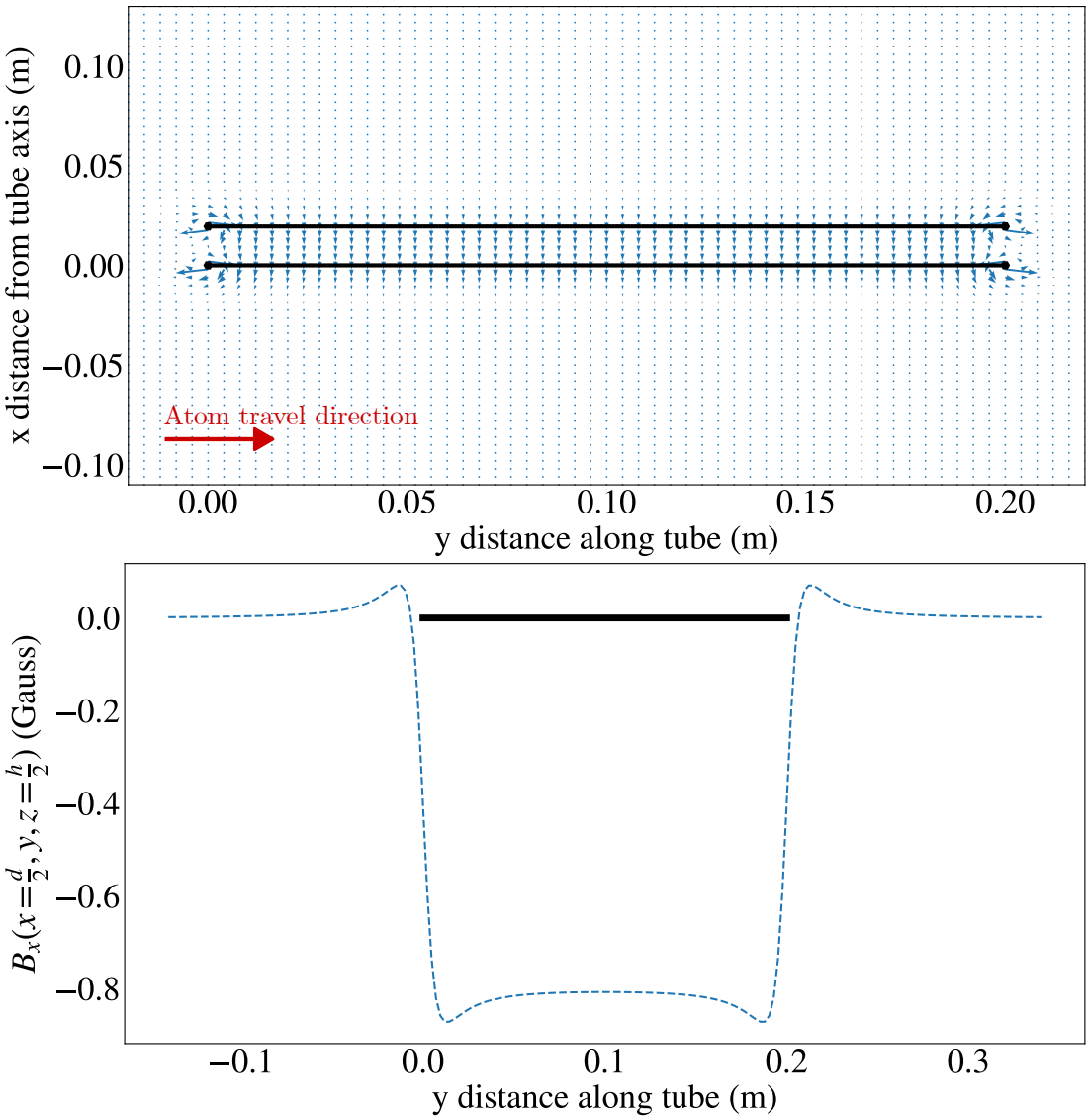

Figure 7.7: **Theoretical magnetic field from a pair of rectangular coils**. *Top*: Magnetic field vectors in the plane cutting through the middle of each rectangular coil. Each dark line represents one coil with only one side visible. *Bottom*: The magnetic field magnitude in the x direction along the path that the atoms take. The dark line indicates the location of the tube.

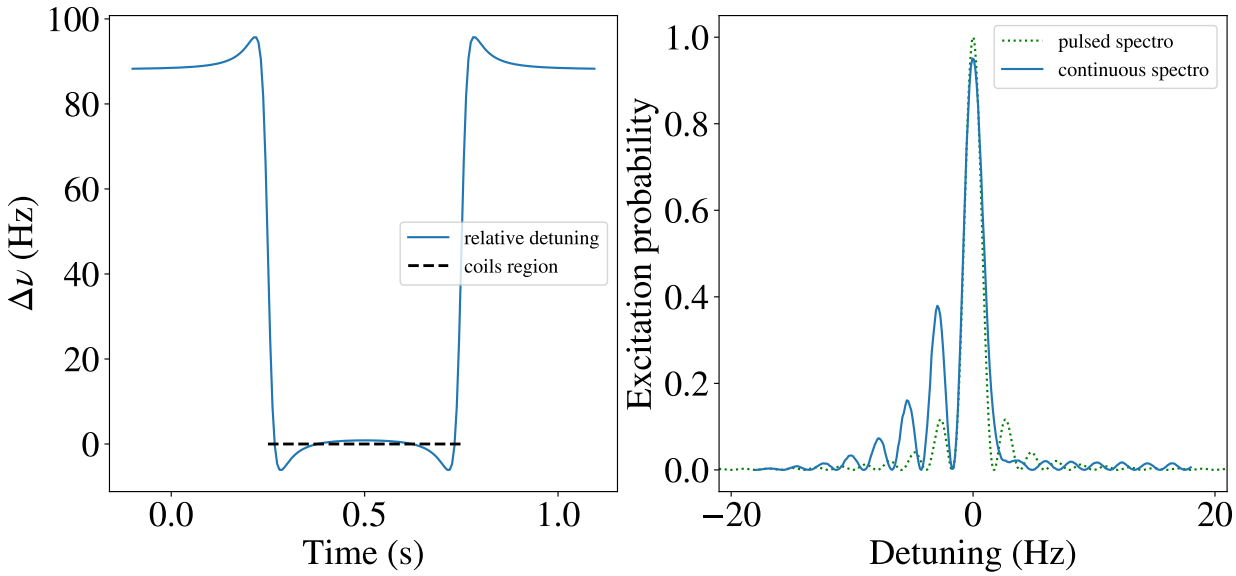

Figure 7.8: **Rabi spectroscopy in a non-uniform magnetic field**. Probe detuning relative to the shifted lines (*left*) and atomic excitation lineshape (*right*) for atoms traveling through the interaction region. The atomic excitation lineshape is overlapped for comparison with the lineshape of a pulsed clock with the same interaction time.

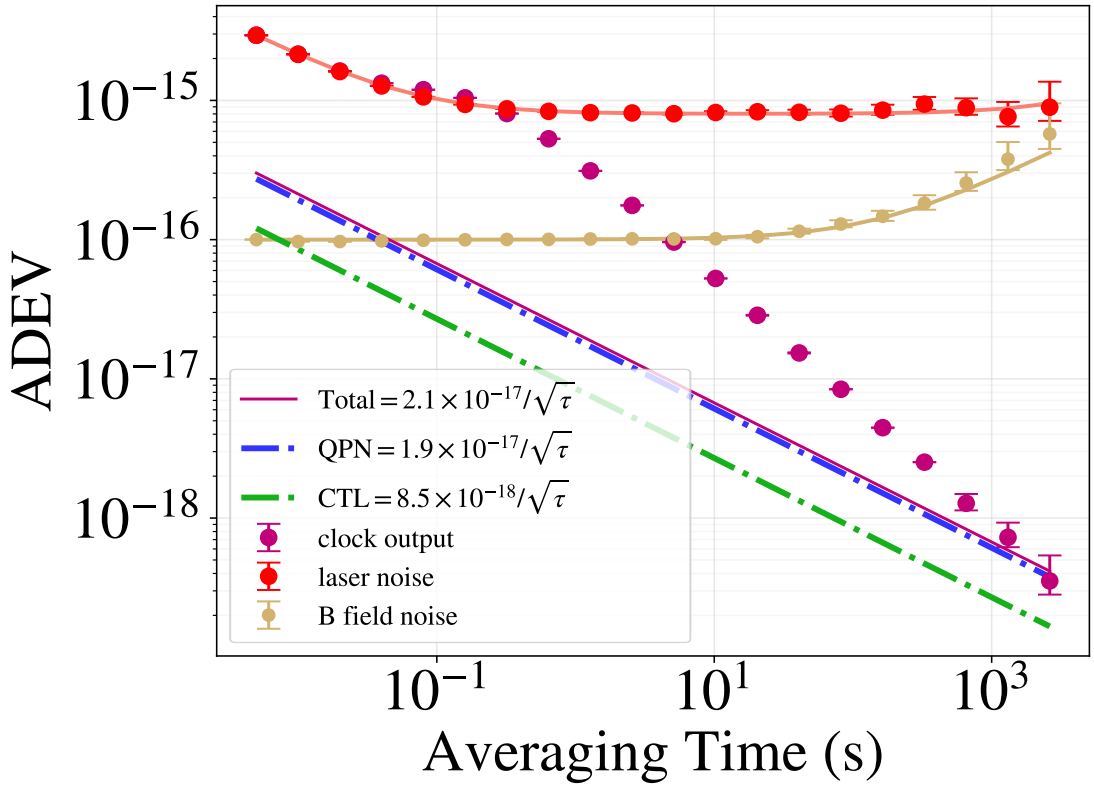

Figure 7.9: **Continuous clock stability**. The overlapping ADEV from the simulation of a clock using continuous dual-tone spectroscopy in a conveyor belt lattice.

Chapter 8

Conclusions

In this thesis, the status of the Strontium optical lattice clock experiment at NPL was presented, detailing measurements with Sr1 for TAI steering and international clock comparison campaigns. Regarding Sr2, upgrades to the experimental hardware including new lasers for the first stage MOT cooling have been reported.

A complex model of clock instability was developed and validated with the use of numerical simulations. In particular, a model of CTL based on phase projection errors was extended to include effects due to the use of multiple measurements for the calculation of frequency corrections and effects due to the quantum projection noise, showing how the limit to clock probe interrogation time is influenced by a multitude of factors different to the coherence time of the local oscillator. The modifications to phase variance in the CTL model associated with dead time could not be fully explained but data regarding the type of response expected was provided as a reference for future attempts to form a comprehensive model. Another novel contribution is the characterisation of the instability resulting from aliasing of linear Zeeman shifts. It was shown that errors arise due to the variations of the magnetic field between the non-simultaneous measurements of the transitions with opposite sensitivities. These can be determined from the PSD profile of the magnetic field noise and the clock operation parameters, namely the form of the sensitivity function and the order in which the lines are measured.

A proposal was made for achieving zero dead-time operation with Sr1 and Sr2 by overcoming the limitations imposed by CTL instability through engineering of the sensitivity function to extend the duty cycle. By making use of dynamical decoupling pulses in the interrogations of the two interleaved clocks, a composite system with nearly-uniform sensitivity function can be achieved, significantly reducing the main technical limitation of lattice clocks from the Dick effect. In the resulting scenario, it is likely that uncompensated errors from the linear Zeeman shifts will be limiting, as indicated by a synchronous comparison of Sr1 and Sr2, so details are provided on the implementation of a setup for performing spectroscopy on the $5/2 \rightarrow 3/2$ transition which yields an order of magnitude suppression. Simulations of the local oscillator phase coherence were used to explain the results from our differential spectroscopy measurements in a hybrid experiment where the Sr lattice clock was used to stabilise the local oscillator interrogating the Yb^+ ion with

improved optical coherence.

In the final chapter, a novel type of spectroscopy is introduced, which makes use of the stretched state splitting and narrowness of the laser to simultaneously drive transitions on both Zeeman lines, thus completely removing any aliasing errors. Simulations show the advantage over conventional methods by maintaining very good stability under high magnetic field noise with only a smaller effect present due to the increased phase variance. Although yet to be implemented in a lattice clock, the dual tone spectroscopy protocol has been shown to not pose major challenges and with its obvious superiority to protocols based on interleaving magnetic lines it has the potential to become a standard approach in the field. Perhaps even more revolutionary is the fact that this new technique provides a solution to the problem of continuous frequency corrections in a Zeeman-allowed interaction region of a conveyor belt lattice clock making the next generation of Dick-noise free lattice clocks possible. Asymmetries of the lineshapes caused by non-uniform magnetic fields are identified but shown to not cause biases in the clock. Finally, the excellent stability of the continuous clock concept is estimated through simulations, showcasing a pristine system free of technical noise.

The themes discussed in this thesis suggest two promising directions for future advancement. First, continuous-operation optical clocks offer a practical path toward deployable systems by relaxing the stringent requirements on optical cavities. These clocks could surpass the stability of current lab-based systems, enabling transformative applications in relativistic geodesy, gravitational anomaly detection, and space-based gravitational wave observation. Second, the emergence of composite systems points to a shift in the fundamental limitation of optical clocks, namely that from optical coherence to atomic coherence. This transition would allow significantly longer interrogation times, unlocking new regimes of precision, which could be further amplified by spin-squeezing. With atomic coherence as the limiting factor, clocks could probe subtle atomic effects, test variations in fundamental constants, and explore quantum many-body dynamics. These capabilities not only enhance timekeeping and navigation but also open up rich opportunities for fundamental physics research, including dark matter searches and Lorentz symmetry tests. Together, these accessible advances mark a new era in precision metrology and quantum science.

Appendix A

Bias functions

The bias functions were introduced by James Barnes [98] as an extension to the Allan variance for estimating the bias of variances from measurements with more than two samples and with dead time. Here they are used on different types of signals with power law spectra to determine statistical properties beyond their Allan variance.

The bias function B_2 is defined as the ratio of the two sample variance of samples taken with dead time in between to the normal two sample variance with adjacent samples. For a signal y, this is

$$B_2(r, \mu) = \frac{\sigma_y^2(T, \tau)}{\sigma_y^2(\tau, \tau)} \tag{8.1}$$

where $\sigma_y^2(T, \tau)$ is a two sample variance with averaging time τ and a time interval T between consecutive samples, and $r = T/\tau$. It is noteworthy that $r < 1$ is also a valid choice with the interpretation of overlapped samples.

The explicit equation for the bias function B_2 is

$$B_2(r \neq 1, \mu) = \frac{1 + \frac{1}{2}\left(2|r|^{\mu+2} - |r+1|^{\mu+2} - |r-1|^{\mu+2}\right)}{2\left(1 - 2^{\mu}\right)}, \tag{8.2}$$

where $r = 1$ was excluded since, by definition, $B_2(1, \mu) = 1$. A useful result is that for white frequency noise we have

$$B_2(r, \mu = -1) = \begin{cases} r & \text{if } 0 \leq r \leq 1 \\ 1 & \text{if } r > 1, \end{cases} \tag{8.3}$$

For flicker frequency noise, $\mu = 0$ and the expression is indeterminate of type $\frac{0}{0}$, so we have to use the L'Hopital rule and get the limit as

$$B_2(r, \mu = 0) = \frac{(r+1)^2 \ln(r+1) + (r-1)^2 \ln(r-1) - 2r^2 \ln r}{4 \ln 2} \tag{8.4}$$

We can see from equations 8.3 and 8.4 some properties of the two kinds of noise. For white noise, which is has no time correlation, comparing samples that are adjacent is no

different to comparing samples separated by dead time. Overlapping samples, however, leads to an over averaging which reduces the variance. For flicker noise, which has some degree of correlation from one sample to the next, the bias increases with dead time indefinitely, as can be more readily noted from the behaviour at large m

$$B_2(m \gg 1, \mu = 0) = \frac{\ln m + 1 - 1/m^2}{2 \ln 2} + \mathcal{O}(1/m^3) \tag{8.5}$$

Time correlations of variations

The time correlation of the variations of a signal y, defined here as

$$\sigma_{yy'}(\tau, m) = \frac{1}{2} \langle (\bar{y}_{n+1} - \bar{y}_n)(\bar{y}_{n+m+1} - \bar{y}_{n+m}) \rangle \tag{8.6}$$

with $\bar{y}$ being the average of y over time intervals τ, is needed in calculating long term clock stability. In this appendix, we derive an expression in terms of the Allan variance of the signal.

We start by writing the Allan variance as

$$\sigma_y^2(\tau) = \frac{1}{2} \left\langle (\bar{y}_{n+1} - \bar{y}_n)^2 \right\rangle = \left\langle \bar{y}_n^2 \right\rangle - \langle \bar{y}_n \bar{y}_{n+1} \rangle \tag{8.7}$$

Similarly, we express the Allan variance for samples with dead time as

$$\frac{1}{2} \left\langle (\bar{y}_{n+k} - \bar{y}_n)^2 \right\rangle = \left\langle \bar{y}_n^2 \right\rangle - \langle \bar{y}_n \bar{y}_{n+k} \rangle \tag{8.8}$$

which can be related to the Allan variance without dead time using the bias function B_2 from equation 8.2 for $r = |k|$. Then we can combine these and get an expression for the correlation function

$$\langle \bar{y}_n \bar{y}_{n+k} \rangle = \left\langle \bar{y}_n^2 \right\rangle - \sigma_y^2(\tau) B_2(|k|, \mu) \tag{8.9}$$

To calculate the time correlation of the variations of y we first write them as

$$\begin{aligned} \sigma_{yy'}(\tau, m) &= \frac{1}{2}(\langle \bar{y}_{n+1} \bar{y}_{n+m+1} \rangle - \langle \bar{y}_{n+1} \bar{y}_{n+m} \rangle - \langle \bar{y}_n \bar{y}_{n+m+1} \rangle + \langle \bar{y}_n \bar{y}_{n+m} \rangle) \\ &= \frac{1}{2}(2 \langle \bar{y}_n \bar{y}_{n+m} \rangle - \langle \bar{y}_n \bar{y}_{n+m-1} \rangle - \langle \bar{y}_n \bar{y}_{n+m+1} \rangle), \end{aligned} \tag{8.10}$$

where in the second line we used the ergodicity of the signal. And then we can use our result from equation 8.9 to arrive at the result

$$\sigma_{yy'}(\tau, m) = \frac{1}{2} \sigma_y^2(\tau) \left[B_2(|m-1|, \mu) + B_2(|m+1|, \mu) - 2B_2(|m|, \mu) \right] \tag{8.11}$$

As a sanity check we see that for $m = 0$ we retrieve the Allan variance

$$\sigma_{yy'}(\tau, 0) = \sigma_y^2(\tau) \tag{8.12}$$

For white noise we have that all the correlations with $m > 1$ are 0, and

$$\sigma_{yy'}(\tau, m = 1) = -\frac{1}{2}\sigma_y^2(\tau) \tag{8.13}$$

For flicker noise, the correlations for $m \geq 1$ evaluate to negative real numbers. They converge to zero for large m as can be determined by using the large m approximation 8.5 of the bias function and using it to calculate the correlation of variations, maintaining only terms of order $1/m^2$ or less

$$\sigma_{yy'}(\tau, m \gg 1) \simeq -\frac{1}{4\ln 2}\sigma_y^2(\tau)/m^2 \tag{8.14}$$

Appendix B

My contribution to the project

I worked in the Strontium optical lattice clock lab together with colleagues Matthew Johnson, Chen-Hao Feng, and Becky Allen at different times and our supervisor Ian Hill. Together, we operated Sr1 for the experiments involving measurements against primary Caesium standards locally and against other optical clocks either locally in the case of Yb^+ ion frequency ratio measurements or in international campaigns. My role in these campaigns has evolved throughout the years from simply assisting in my first years to being critically involved in maintaining the laser systems and stabilisation loops both during the preparation stages and the operation stages in my last year.

I have made significant contributions to the experimental efforts to bring Sr2 from its dormant state to an operational clock mainly focusing on the first stage MOT cooling. Firstly, I have integrated the new commercial light generation system for the 461 nm light by setting up a phase-locked loop to our master 922 ECDL and reconfigured part of the distribution to the slowing beam/MOT beam/probe beam with assistance from colleagues. At the same time, taking on a project started by Matthew, I worked together with Becky to assemble and test different laser designs for the 497 nm repumping light, as well as the EOM modulated 707 nm laser which we ended up using. Together with Ian and Chen-Hao, we have also made improvements to the Strontium source in two iterations, changing vacuum parts and the mounting structure for ease of alignment. Finally, working together with Chen-Hao and with frequent feedback from Ian, we have gradually optimised all the other stages in the Sr2 clock cycle moving from blue MOT with ^{88}Sr to spectroscopy with ^{87}Sr and a synchronous measurement with Sr1 in the span of 6 months.

All the numerical simulations presented in this thesis have been performed by me using code that I built from the ground up together with pre-existing code written by Richard Hobson for estimating spectroscopic lineshapes and sensitivity functions. For the clock instability models in Chapter 3, I have used the simulations as well as analytical derivations to identify extensions to the coherence time limit model as described in the chapter, and to produce the instability model for the linear Zeeman shift errors. I have also performed the analysis in the last chapter using the simulations and additional scripts for generating the magnetic field lines used as a test example.

References

[1] S. Weyers et al. "Distributed cavity phase frequency shifts of the caesium fountain PTB-CSF2". In: *Metrologia* 49 (1 Nov. 2011), p. 82. ISSN: 0026-1394. DOI: 10.1088/0026-1394/49/1/012. URL: https://iopscience.iop.org/article/10.1088/0026-1394/49/1/012.

[2] T. P. Heavner et al. "First accuracy evaluation of NIST-F2". In: *Metrologia* 51 (3 May 2014), p. 174. ISSN: 0026-1394. DOI: 10.1088/0026-1394/51/3/174. URL: https://iopscience.iop.org/article/10.1088/0026-1394/51/3/174.

[3] A. Bauch. "Caesium atomic clocks: function, performance and applications". In: *Meas. Sci. Technol.* 14 (8 July 2003), p. 1159. ISSN: 0957-0233. DOI: 10.1088/0957-0233/14/8/301. URL: https://iopscience.iop.org/article/10.1088/0957-0233/14/8/301.

[4] B. Jaduszliwer and J. Camparo. "Past, present and future of atomic clocks for GNSS". In: *GPS Solutions* 25 (1 Jan. 2021), pp. 1–13. ISSN: 15211886. DOI: 10.1007/S10291-020-01059-X/FIGURES/10. URL: https://link.springer.com/article/10.1007/s10291-020-01059-x.

[5] J. Nauta et al. "Evaluation of a caesium fountain frequency standard for antihydrogen spectroscopy". In: *Metrologia* 62 (4 Aug. 2025), p. 045008. ISSN: 0026-1394. DOI: 10.1088/1681-7575/ADF64A. URL: https://iopscience.iop.org/article/10.1088/1681-7575/adf64a.

[6] T. Udem et al. "Absolute Optical Frequency Measurement of the Cesium D1 Line with a Mode-Locked Laser". In: *Phys. Rev. Lett.* 82 (18 May 1999), p. 3568. ISSN: 10797114. DOI: 10.1103/PhysRevLett.82.3568. URL: https://journals.aps.org/prl/abstract/10.1103/PhysRevLett.82.3568.

[7] D J. Jones et al. "Carrier-envelope phase control of femtosecond mode-locked lasers and direct optical frequency synthesis". In: *Science* 288 (5466 Apr. 2000), pp. 635–639. ISSN: 00368075. DOI: 10.1126/science.288.5466.635.

[8] J. M Robinson et al. "Crystalline optical cavity at 4 K with thermal-noise-limited instability and ultralow drift". In: *Optica* 6 (2 Feb. 2019), pp. 240–243. DOI: 10.1364/OPTICA.6.000240. URL: https://doi.org/10.1364/OPTICA.6.000240.

[9] H. Katori et al. "Ultrastable optical clock with neutral atoms in an engineered light shift trap". In: *Phys. Rev. Lett.* 91 (17 Oct. 2003), p. 173005. ISSN: 10797114. DOI: 10.1103/PHYSREVLETT.91.173005/FIGURES/2/MEDIUM. URL: https://journals.aps.org/prl/abstract/10.1103/PhysRevLett.91.173005.

[10] T. Lindvall et al. "Coordinated international comparisons between optical clocks connected via fiber and satellite links". In: *Optica* 12 (6 June 2025), pp. 843–852. ISSN: 2334-2536. DOI: 10.1364/OPTICA.561754.

[11] M. C. Marshall et al. "High-Stability Single-Ion Clock with 5.5×10^{-19} Systematic Uncertainty". In: *Phys. Rev. Lett.* 135 (3 July 2025), p. 033201. ISSN: 10797114. DOI: 10.1103/hb3c-dk28. URL: https://journals.aps.org/prl/abstract/10.1103/hb3c-dk28.

[12] Bao-lin Zhang et al. "Liquid-Nitrogen-Cooled $^{40}Ca^{+}$ Ion Optical Clock with a Systematic Uncertainty of 4.4×10^{-19}". In: *Phys. Rev. Lett.* 136 (5 Feb. 2026), p. 053202. ISSN: 0031-9007. DOI: 10.1103/vngc-c1xv. URL: https://journals.aps.org/prl/abstract/10.1103/vngc-c1xv.

[13] A. Aeppli et al. "Clock with 8×10^{-9} Systematic Uncertainty". In: *Phys. Rev. Lett.* 133 (2 July 2024), p. 023401. ISSN: 10797114. DOI: 10.1103/PhysRevLett.133.023401. URL: https://journals.aps.org/prl/abstract/10.1103/PhysRevLett.133.023401.

[14] W. F. McGrew et al. "Atomic clock performance enabling geodesy below the centimetre level". In: *Nature* 564 (7734 Nov. 2018), pp. 87–90. ISSN: 1476-4687. DOI: 10.1038/s41586-018-0738-2. URL: https://www.nature.com/articles/s41586-018-0738-2.

[15] M. Takamoto et al. "Test of general relativity by a pair of transportable optical lattice clocks". In: *Nature Photon* 14 (July 2020), pp. 411–415. DOI: 10.1038/s41566-020-0619-8. URL: https://doi.org/10.1038/s41566-020-0619-8.

[16] Noriaki Ohmae et al. "Transportable Strontium Optical Lattice Clocks Operated Outside Laboratory at the Level of 10^{-18} Uncertainty". In: *Adv. Quantum Technol.* 4 (8 Aug. 2021), p. 2100015. ISSN: 25119044. DOI: 10.1002/qute.202100015. URL: https://onlinelibrary.wiley.com/doi/abs/10.1002/qute.202100015.

[17] I Nosske et al. "Transportable strontium lattice clock with 4×10^{-19} blackbody radiation shift uncertainty". In: *Quantum Sci. Technol.* 10 (4 Oct. 2025), p. 045076. ISSN: 20589565. DOI: 10.1088/2058-9565/ae1161. URL: https://iopscience.iop.org/article/10.1088/2058-9565/ae1161.

[18] K. Beloy et al. "Frequency ratio measurements at 18-digit accuracy using an optical clock network Boulder Atomic Clock Optical Network (BACON) Collaboration". In: *Nature* 591 (Mar. 2021), pp. 564–569. DOI: 10.1038/s41586-021-03253-4. URL: https://doi.org/10.1038/s41586-021-03253-4.

[19] H S Margolis et al. "Robust Optical Clocks for International Timescales (ROCIT)". In: *J. Phys.: Conf. Ser.* 2889 (2024), p. 12022. DOI: 10.1088/1742-6596/2889/1/012022.

[20] ICON Collaboration. "International comparison of optical frequencies with transportable optical lattice clocks". In: *arXiv* (Oct. 2024). DOI: arXiv:2410.22973. URL: https://arxiv.org/pdf/2410.22973.

[21] N. Dimarcq et al. "Roadmap towards the redefinition of the second". In: *Metrologia* 61 (1 Jan. 2024), p. 012001. ISSN: 0026-1394. DOI: 10.1088/1681-7575/AD17D2. URL: https://iopscience.iop.org/article/10.1088/1681-7575/ad17d2.

[22] M. Abgrall et al. "Optically steered time scale generation at OP and NPL and remote comparisons". In: *Journal of Physics: Conference Series* 2889 (1 Nov. 2024), p. 012024. ISSN: 1742-6596. DOI: 10.1088/1742-6596/2889/1/012024. URL: https://iopscience.iop.org/article/10.1088/1742-6596/2889/1/012024.

[23] M. S. Safronova. "The Search for Variation of Fundamental Constants with Clocks". In: *Annalen der Physik* 531 (5 May 2019), p. 1800364. ISSN: 15213889. DOI: 10.1002/andp.201800364.

[24] G. Barontini et al. "Measuring the stability of fundamental constants with a network of clocks". In: *EPJ Quantum Technol.* 9 (1 May 2022), pp. 1–52. ISSN: 2196-0763. DOI: 10.1140/EPJQT/S40507-022-00130-5. URL: https://epjquantumtechnology.springeropen.com/articles/10.1140/epjqt/s40507-022-00130-5.

[25] M. G. Kozlov et al. "Highly charged ions: Optical clocks and applications in fundamental physics". In: *Rev. Mod. Phys.* 90 (4 Dec. 2018), p. 045005. ISSN: 15390756. DOI: 10.1103/RevModPhys.90.045005. URL: https://journals.aps.org/rmp/abstract/10.1103/RevModPhys.90.045005.

[26] V. V. Flambaum and V. A. Dzuba. "Search for variation of the fundamental constants in atomic, molecular, and nuclear spectra". In: *Canadian Journal of Physics* 87 (1 Jan. 2011), pp. 25–33. ISSN: 00084204. DOI: 10.1139/P08-072.

[27] Nathaniel Sherrill et al. "Analysis of atomic-clock data to constrain variations of fundamental constants". In: *New J. Phys.* 25 (9 Sept. 2023), p. 093012. ISSN: 1367-2630. DOI: 10.1088/1367-2630/aceff6. URL: https://iopscience.iop.org/article/10.1088/1367-2630/aceff6.

[28] T. Takano et al. "Geopotential measurements with synchronously linked optical lattice clocks". In: *Nature Photon* 10 (10 Aug. 2016), pp. 662–666. ISSN: 1749-4893. DOI: 10.1038/nphoton.2016.159. URL: https://www.nature.com/articles/nphoton.2016.159.

[29] Y. Yuan et al. "Demonstration of chronometric leveling using transportable optical clocks beyond laser coherence limit". In: *Phys. Rev. Appl.* 21 (4 Apr. 2024), p. 044052. DOI: 10.1103/PhysRevApplied.21.044052.

[30] H. Shinkai, M. Takamoto, and H. Katori. "Transportable optical lattice clocks and general relativity". In: *arXiv* 11 (Feb. 2025).

[31] S Kolkowitz et al. "Gravitational wave detection with optical lattice atomic clocks". In: *Phys. Rev. D* 94 (12 Dec. 2016), p. 124043. DOI: 10.1103/PhysRevD.94.124043.

[32] A. Derevianko and M. Pospelov. "Hunting for topological dark matter with atomic clocks". In: *Nature Phys* 10 (12 Nov. 2014), pp. 933–936. ISSN: 17452481. DOI: 10.1038/nphys3137. URL: https://www.nature.com/articles/nphys3137.

[33] T. L. Nicholson et al. "Systematic evaluation of an atomic clock at 2×10^{-18} total uncertainty". In: *Nature Commun* 6 (1 Apr. 2015), pp. 1–8. ISSN: 2041-1723. DOI: 10.1038/ncomms7896. URL: https://www.nature.com/articles/ncomms7896.

[34] T. Bothwell et al. "JILA SrI optical lattice clock with uncertainty of 2.0×10^{-18}". In: *Metrologia* 56 (6 Oct. 2019), p. 065004. ISSN: 0026-1394. DOI: 10.1088/1681-7575/AB4089. URL: https://iopscience.iop.org/article/10.1088/1681-7575/ab4089.

[35] P. Lemonde and P. Wolf. "Optical lattice clock with atoms confined in a shallow trap". In: *Phys. Rev. A* 72 (Sept. 2005), p. 033409. DOI: 10.1103/PhysRevA.72.033409. URL: https://journals.aps.org/pra/pdf/10.1103/PhysRevA.72.033409.

[36] K. Kim et al. "Evaluation of lattice light shift at low 10^{-19} uncertainty for a shallow lattice Sr optical clock". In: *Phys. Rev. Lett.* 130 (11 Mar. 2023), p. 113203. DOI: 10.1103/PhysRevLett.130.113203. URL: https://link.aps.org/accepted/10.1103/PhysRevLett.130.113203.

[37] S. Dörscher et al. "Experimental determination of the E2-M1 polarizability of the strontium clock transition". In: *Phys. Rev. Research* 5 (1 Jan. 2023), p. L012013. ISSN: 26431564. DOI: 10.1103/PHYSREVRESEARCH.5.L012013/SIDEBAND_HOT.CSV. URL: https://journals.aps.org/prresearch/abstract/10.1103/PhysRevResearch.5.L012013.

[38] I. Ushijima, M. Takamoto, and H. Katori. "Operational Magic Intensity for Sr Optical Lattice Clocks". In: *Phys. Rev. Lett.* 121 (26 Dec. 2018), p. 263202. ISSN: 10797114. DOI: 10.1103/PhysRevLett.121.263202.

[39] A. Al-Masoudi et al. "Noise and instability of an optical lattice clock". In: *Phys. Rev. A* 92 (6 Dec. 2015), p. 063814. ISSN: 10941622. DOI: 10.1103/PHYSREVA.92.063814/FIGURES/7/MEDIUM. URL: https://journals.aps.org/pra/abstract/10.1103/PhysRevA.92.063814.

[40] S. L. Campbell et al. "A Fermi-degenerate three-dimensional optical lattice clock". In: *Science* 358 (6359 Oct. 2017), pp. 90–94. ISSN: 10959203. DOI: 10.1126/SCIENCE.AAM5538/SUPPL_FILE/AAM5538_CAMPBELL_SM.PDF.

[41] J L Siegel et al. "Excited-Band Coherent Delocalization for Improved Optical Lattice Clock Performance". In: *Phys. Rev. Lett* 132 (13 Mar. 2024), p. 133201. DOI: 10.1103/PhysRevLett.132.133201.

[42] A. André, A. S. Sørensen, and M. D. Lukin. "Stability of atomic clocks based on entangled atoms". In: *Phys. Rev. Lett.* 92 (23 June 2004), p. 230801. ISSN: 00319007. DOI: 10.1103/PHYSREVLETT.92.230801/FIGURES/2/MEDIUM. URL: https://journals.aps.org/prl/abstract/10.1103/PhysRevLett.92.230801.

[43] M. Schulte et al. "Prospects and challenges for squeezing-enhanced optical atomic clocks". In: *Nature Commun* 11 (1 Nov. 2020), pp. 1–10. ISSN: 2041-1723. DOI: 10.1038/s41467-020-19403-7. URL: https://www.nature.com/articles/s41467-020-19403-7.

[44] M. M. Boyd et al. "Nuclear spin effects in optical lattice clocks". In: *Phys. Rev. A* 76 (2 Aug. 2007), p. 022510. ISSN: 10502947. DOI: 10.1103/PHYSREVA.76.022510/FIGURES/12/MEDIUM. URL: https://journals.aps.org/pra/abstract/10.1103/PhysRevA.76.022510.

[45] K. Numata, A. Kemery, and J. Camp. "Thermal-noise limit in the frequency stabilization of lasers with rigid cavities". In: *Phys. Rev. Lett.* 93 (25 Dec. 2004), p. 250602. ISSN: 00319007. DOI: 10.1103/PHYSREVLETT.93.250602/FIGURES/2/MEDIUM. URL: https://journals.aps.org/prl/abstract/10.1103/PhysRevLett.93.250602.

[46] T. Legero, U. Sterr, and T. Kessler. "Thermal noise in optical cavities revisited". In: *J. Opt. Soc. Am. B* 29 (1 Jan. 2012), pp. 178–184. ISSN: 1520-8540. DOI: 10.1364/JOSAB.29.000178.

[47] D G Matei et al. "1.5 μm Lasers with Sub-10 mHz Linewidth". In: *Phys. Rev. Lett.* 118 (26 June 2017), p. 263202. DOI: 10.1103/PhysRevLett.118.263202.

[48] D. Kedar et al. "Frequency stability of cryogenic silicon cavities with semiconductor crystalline coatings". In: *Optica* 10 (4 Apr. 2023), pp. 464–470. ISSN: 2334-2536. DOI: 10.1364/OPTICA.479462.

[49] D. Lee et al. "Frequency stability of 2.5×10^{-17} in a Si cavity with AlGaAs crystalline mirrors". In: *Phys. Rev. Lett.* 136 (3 Jan. 2026), p. 033801. DOI: https://doi.org/10.1103/zgrm-cjbb.

[50] S. Falke et al. "10^{-17} fractional laser frequency instability with a long room-temperature cavity". In: *Opt. Lett.* 40 (9 May 2015), pp. 2112–2115. ISSN: 1539-4794. DOI: 10.1364/OL.40.002112.

[51] A. L. Parke and M. Schioppo. "Three hundred microsecond optical cavity storage time and 10^{-7} active RAM cancellation for 10^{-19} laser frequency stabilization". In: *Opt. Lett.* 50 (10 May 2025), pp. 3405–3408. ISSN: 1539-4794. DOI: 10.1364/OL.560815.

[52] N. Hinkley et al. "An atomic clock with 10-18 instability". In: *Science* 341 (6151 Sept. 2013), pp. 1215–1218. ISSN: 10959203. DOI: 10.1126/SCIENCE.1240420/SUPPL_FILE/HINKLEY.SM.PDF. URL: https://www.science.org/doi/10.1126/science.1240420.

[53] I. Ushijima et al. "Cryogenic optical lattice clocks". In: *Nature Photonics* 9 (3 Feb. 2015), pp. 185–189. ISSN: 17494893. DOI: 10.1038/nphoton.2015.5. URL: https://www.nature.com/articles/nphoton.2015.5.

[54] E. Oelker et al. "Demonstration of 4.8×1017 stability at 1 s for two independent optical clocks". In: *Nature Photonics 2019 13:10* 13 (10 July 2019), pp. 714–719. ISSN: 1749-4893. DOI: 10.1038/s41566-019-0493-4. URL: https://www.nature.com/articles/s41566-019-0493-4.

[55] S M Brewer et al. "Al+27 Quantum-Logic Clock with a Systematic Uncertainty below 10-18". In: *Phys. Rev. Lett.* 123 (3 July 2019), p. 033201. DOI: 10.1103/PhysRevLett.123.033201.

[56] N. Huntemann et al. "Single-Ion Atomic Clock with 3×10^{-18} Systematic Uncertainty". In: *Phys. Rev. Lett.* 116 (6 Feb. 2016), p. 063001. DOI: 10.1103/PhysRevLett.116.063001.

[57] W. M. Itano et al. "Quantum Projection Noise: Population Fluctuations in 2-Level Systems". In: *Phys. Rev. A* 47 (5 May 1993), p. 3554. DOI: 10.1103/PhysRevA.47.3554. URL: https://www.nist.gov/publications/quantum-projection-noise-population-fluctuations-2-level-systems.

[58] A. D. Ludlow et al. "Optical atomic clocks". In: *Rev. Mod. Phys.* 87 (2 June 2015), p. 637. ISSN: 15390756. DOI: 10.1103/RevModPhys.87.637. URL: https://journals.aps.org/rmp/abstract/10.1103/RevModPhys.87.637.

[59] M. Schioppo et al. "Ultrastable optical clock with two cold-atom ensembles". In: *Nature Photon* 11 (1 Nov. 2017), pp. 48–52. ISSN: 1749-4893. DOI: 10.1038/nphoton.2016.231. URL: https://www.nature.com/articles/nphoton.2016.231.

[60] P. G. Westergaard. "Strontium Optical Lattice Clock: In Quest of the Ultimate Performance". PhD thesis. Ecole nationale supérieure des telecommunications- ENST, 2010. URL: https://pastel.hal.science/pastel-00560080v1.

[61] P. G. Westergaard, J. Lodewyck, and P. Lemonde. "Minimizing the dick effect in an optical lattice clock". In: *IEEE Transactions on Ultrasonics, Ferroelectrics, and Frequency Control* 57 (3 Mar. 2010), pp. 623–628. ISSN: 08853010. DOI: 10.1109/TUFFC.2010.1457.

[62] D. B Hume and D. R Leibrandt. "Probing beyond the laser coherence time in optical clock comparisons". In: *Phys. Rev. A* 93 (3 Mar. 2016), p. 32138. DOI: 10.1103/PhysRevA.93.032138.

[63] R. Kohlhaas et al. "Phase locking a clock oscillator to a coherent atomic ensemble". In: *Phys. Rev. X* 5 (2 Apr. 2015), p. 021011. ISSN: 21603308. DOI: 10.1103/PHYSREVX.5.021011/FIGURES/7/MEDIUM. URL: https://journals.aps.org/prx/abstract/10.1103/PhysRevX.5.021011.

[64] W. Bowden et al. "Improving the Q Factor of an Optical Atomic Clock Using Quantum Nondemolition Measurement". In: *Phys. Rev. X* 10 (4 Dec. 2020), p. 041052. ISSN: 21603308. DOI: 10.1103/PHYSREVX.10.041052/FIGURES/4/MEDIUM. URL: https://journals.aps.org/prx/abstract/10.1103/PhysRevX.10.041052.

[65] S. Dörscher et al. "Dynamical decoupling of laser phase noise in compound atomic clocks". In: *Commun. Phys.* 3 (1 Oct. 2020), pp. 1–9. ISSN: 2399-3650. DOI: 10.1038/s42005-020-00452-9. URL: https://www.nature.com/articles/s42005-020-00452-9.

[66] M. Chwalla et al. "Precision spectroscopy with two correlated atoms". In: *Appl. Phys. B* 89 (4 Dec. 2007), pp. 483–488. ISSN: 09462171. DOI: 10.1007/S00340-007-2867-4.

[67] E. R Clements et al. "Lifetime-Limited Interrogation of Two Independent $^{27}Al^{+}$ Clocks Using Correlation Spectroscopy". In: *Phys. Rev. Lett.* 125 (24 Dec. 2020), p. 243602. DOI: 10.1103/PhysRevLett.125.243602.

[68] E. M Bridge. "Towards a Strontium Optical Lattice Clock". PhD thesis. University of Oxford, 2012. URL: https://ora.ox.ac.uk/objects/uuid:a96e73fe-f17b-4738-be1d-34429b5b4a05/download_file?safe_filename=Thesis_E%2BM%2BBridge.pdf.pdf&file_format=application%2Fpdf&type_of_work=Thesis.

[69] Ian R Hill. "Development of an Apparatus for a Strontium Optical Lattice Optical Frequency Standard". PhD thesis. Imperial College London, 2012.

[70] I. R. Hill et al. "A low maintenance Sr optical lattice clock". In: *J. Phys.: Conf. Ser.* 723 (1 June 2016), p. 012019. ISSN: 1742-6596. DOI: 10.1088/1742-6596/723/1/012019. URL: https://iopscience.iop.org/article/10.1088/1742-6596/723/1/012019.

[71] R. Hobson. "An Optical Lattice Clock with Neutral Strontium". PhD thesis. University of Oxford, 2016.

[72] W. Bowden. "Precision Frequency Metrology with Optical Lattice Clocks". PhD thesis. University of Oxford, 2019.

[73] R. Hobson et al. "A strontium optical lattice clock with 1×10^{-17} uncertainty and measurement of its absolute frequency". In: *Metrologia* 57 (6 2020), p. 065026. DOI: 10.1088/1681-7575/abb530. URL: https://doi.org/10.1088/1681-7575/abb530.

[74] A. M Vianello. "Quantum Engineering in a Strontium Optical Lattice Clock". PhD thesis. Imperial College London, 2022.

[75] H. Schnatz et al. "Phase-coherent frequency comparison of optical clocks using a telecommunication fiber link". In: *IEEE Transactions on Ultrasonics, Ferroelectrics, and Frequency Control* 57 (1 Jan. 2010), pp. 175–181. ISSN: 08853010. DOI: 10.1109/TUFFC.2010.1395.

[76] K. Predehl et al. "A 920-kilometer optical fiber link for frequency metrology at the 19th decimal place". In: *Science* 336 (6080 Apr. 2012), pp. 441–444. ISSN: 10959203. DOI: 10.1126/SCIENCE.1218442/SUPPL_FILE/441.MP3.

[77] O. Lopez et al. "Ultra-stable long distance optical frequency distribution using the Internet fiber network". In: *Opt. Express* 20 (21 Oct. 2012), pp. 23518–23526. ISSN: 1094-4087. DOI: 10.1364/OE.20.023518.

[78] N. Chiodo et al. "Cascaded optical fiber link using the internet network for remote clocks comparison". In: *Opt. Express* 23 (26 Dec. 2015), pp. 33927–33937. ISSN: 1094-4087. DOI: 10.1364/OE.23.033927.

[79] S. M F Raupach, A. Koczwara, and G. Grosche. "Brillouin amplification supports 1×10^{-20} uncertainty in optical frequency transfer over 1400 km of underground fiber". In: *Phys. Rev. A* 92 (2 Aug. 2015), p. 21801. DOI: 10.1103/PhysRevA.92.021801.

[80] C. Lisdat et al. "A clock network for geodesy and fundamental science". In: *Nature Communications* 7 (1 Aug. 2016), pp. 1–7. ISSN: 20411723. DOI: 10.1038/NCOMMS12443;TECHMETA. URL: https://www.nature.com/articles/ncomms12443.

[81] J. Xu et al. "A review of tidal triggering of global earthquakes". In: *Geodesy and Geodynamics* 14 (1 Jan. 2023). DOI: 10.1016/j.geog.2022.06.005.

[82] M. Schioppo et al. "Comparing ultrastable lasers at 7×10^{-17} fractional frequency instability through a 2220 km optical fibre network". In: *Nat. Commun.* 13 (1 Jan. 2022), pp. 1–11. ISSN: 2041-1723. DOI: 10.1038/s41467-021-27884-3. URL: https://www.nature.com/articles/s41467-021-27884-3.

[83] F. Butuc-Mayer et al. "Duty cycle engineering for improved optical lattice clock stability". In: *J. Phys.: Conf. Ser.* 2889 (1 Nov. 2024), p. 012049. ISSN: 1742-6596. DOI: 10.1088/1742-6596/2889/1/012049. URL: https://iopscience.iop.org/article/10.1088/1742-6596/2889/1/012049.

[84] E. D Black. "An introduction to Pound-Drever-Hall laser frequency stabilization". In: *Am. J. Phys.* 69 (Jan. 2001). DOI: 10.1119/1.1286663.

[85] J. Samland et al. "Optical pumping of $5s4d\,^1D_2$ strontium atoms for laser cooling and imaging". In: *Phys. Rev. Research* 6 (1 Mar. 2024), p. 0133319. DOI: 10.1103/PhysRevResearch.6.013319.

[86] V. Schkolnik, O. Fartmann, and M. Krutzik. "An extended-cavity diode laser at 497 nm for laser cooling and trapping of neutral strontium". In: *Laser Phys.* 29 (3 Feb. 2019), p. 035802. ISSN: 1555-6611. DOI: 10.1088/1555-6611/AAFFC8. URL: https://iopscience.iop.org/article/10.1088/1555-6611/aaffc8.

[87] S B Nagel et al. "Magnetic trapping of metastable $^3P_2$ atomic strontium". In: *Phys. Rev. A* 67 (1 2003). DOI: 10.1103/PhysRevA.67.011401.

[88] S. B Nagel. "Ultracold Collisions in Atomic Strontium". PhD thesis. Rice University, Feb. 2008.

[89] M. Yasuda and H. Katori. "Lifetime Measurement of the $^3P_2$ Metastable State of Strontium Atoms". In: *Phys. Rev. Lett.* 92 (15 Apr. 2004), p. 153004. DOI: 10.1103/PhysRevLett.92.153004.

[90] A. Tofful et al. "$^{171}Yb^+$ optical clock with 2.2×10^{-18} systematic uncertainty and absolute frequency measurements". In: *Metrologia* 61 (4 June 2024). DOI: 10.1088/1681-7575/ad53cd.

[91] E. Rubiola and F. Vernotte. "The Companion of Enrico's Chart for Phase Noise and Two-Sample Variances". In: *IEEE Transactions on microwave theory and techniques* 71 (7 July 2003), pp. 2996–3025. DOI: 10.1109/TMTT.2023.3238267. URL: https://ieeexplore.ieee.org/document/10050257.

[92] C.J. Foot. "Atomic Physics". In: *Oxford University Press* (2004). URL: https://global.oup.com/academic/product/atomic-physics-9780198506966.

[93] I. Leroux et al. "On-line estimation of local oscillator noise and optimisation of servo parameters in atomic clocks". In: *Metrologia* 54 (3 2017), p. 307. DOI: 10.1088/1681-7575/aa66e9.

[94] G J. Dick. "Local oscillator induced instabilities in trapped ion frequency standards". In: *Proceedings of the 19th Annual Precise Time and Time Interval Systems and Applications Meeting*. Dec. 1987, pp. 137–147.

[95] G. J. Dick et al. "Local oscillator induced degradation of medium-term stability in passive atomic frequency standards". In: *The 22nd Annual Precise Time and Time Interval (PTTI) Applications and Planning Meeting*. Dec. 1990, pp. 487–508. URL: https://ntrs.nasa.gov/citations/19910016484.

[96] P. Lemonde et al. "Sensitivity function: a new tool for the evaluation of frequency shifts in atomic spectroscopy". In: *Proceedings of the Annual IEEE International Frequency Control Symposium*. IEEE, 1998, pp. 110–115. DOI: 10.1109/FREQ.1998.717890. URL: https://ieeexplore.ieee.org/stamp/stamp.jsp?tp=&arnumber=717890.

[97] T KIelinski and K Hammerer. "Bayesian frequency metrology with optimal Ramsey interferometry in optical atomic clocks". In: *Rep. Prog. Phys.* 88 (12 Dec. 2025), p. 124001. ISSN: 13616633. DOI: 10.1088/1361-6633/ae213d. URL: https://iopscience.iop.org/article/10.1088/1361-6633/ae213d.

[98] J. A. Barnes. *Tables of Bias Functions, B1 and B2, for Variances Based on Finite Samples of Processes with Power Law Spectral Densities*. Tech. rep. National Bureau of Standards, Jan. 1969. URL: https://tf.nist.gov/general/pdf/11.pdf.

[99] J. A. Barnes and D. W Allan. *Variances based on data with dead time between the measurements*. Tech. rep. National Bureau of Standards, 1990.

[100] T. Bothwell et al. "Deployment of a Transportable Yb Optical Lattice Clock". In: *Opt. Lett.* 50 (2 2024), pp. 646–649. DOI: https://doi.org/10.48550/arXiv.2409.16264. URL: https://arxiv.org/abs/2409.16264.

[101] P. Gaynor et al. "Dual-axis cubic cavity for drift-compensated multi-wavelength laser stabilisation". In: *Opt. Express* 29 (22 Oct. 2021), pp. 36758–36768. ISSN: 1094-4087. DOI: 10.1364/OE.436019.

[102] A. Brusch et al. "Hyperpolarizability Effects in a Sr Optical Lattice Clock". In: *Phys. Rev. Lett.* 96 (10 Mar. 2006), p. 103003. DOI: 10.1103/PhysRevLett.96.103003.

[103] T. L Nicholson. "A new record in atomic clock performance". PhD thesis. University of Colorado, 2015.

[104] P. G. Westergaard et al. "Lattice-induced frequency shifts in Sr optical lattice clocks at the 10^{-17} level". In: *Phys. Rev. Lett.* 106 (21 May 2011), p. 210801. ISSN: 00319007. DOI: 10.1103/PHYSREVLETT.106.210801/FIGURES/5/MEDIUM. URL: https://journals.aps.org/prl/abstract/10.1103/PhysRevLett.106.210801.

[105] Z.-P. Jia et al. "Improved systematic evaluation of a strontium optical clock with uncertainty below 1×10^{-18}". In: *Metrologia* 63 (2 Mar. 2026), p. 025002. DOI: 10.1088/1681-7575/ae449e.

[106] M. E. Kim et al. "Improved interspecies optical clock comparisons through differential spectroscopy". In: *Nature Phys* 19 (1 Nov. 2022), pp. 25–29. ISSN: 1745-2481. DOI: 10.1038/s41567-022-01794-7. URL: https://www.nature.com/articles/s41567-022-01794-7.

[107] N. Herschbach et al. "Linear Paul trap design for an optical clock with Coulomb crystals". In: *Appl. Phys. B* 107 (4 June 2012), pp. 891–906. ISSN: 09462171. DOI: 10.1007/S00340-011-4790-Y/METRICS. URL: https://link.springer.com/article/10.1007/s00340-011-4790-y.

[108] C. Hagemann et al. "Providing 10^{-16} short-term stability of a 1.5 μm laser to optical clocks". In: *IEEE Transactions on Instrumentation and Measurement* 62 (6 2013), pp. 1556–1562. ISSN: 00189456. DOI: 10.1109/TIM.2013.2242597.

[109] M. Giunta et al. "Real-time phase tracking for wide-band optical frequency measurements at the 20th decimal place". In: *Nature Photon* 14 (1 Jan. 2020), pp. 44–49. ISSN: 17494893. DOI: 10.1038/S41566-019-0520-5;TECHMETA. URL: https://www.nature.com/articles/s41566-019-0520-5.

[110] M Bishof et al. "Inelastic collisions and density-dependent excitation suppression in a ^{87}Sr optical lattice clock". In: *Phys. Rev. A* 84 (5 Nov. 2011), p. 052716. DOI: 10.1103/PhysRevA.84.052716.

[111] X.-Y. Liu et al. "A zero-dead-time strontium lattice clock with a stability at 10^{-19} level". In: *Phys. Rev. Lett.* 135 (26 Dec. 2025), p. 263402. DOI: 10.1103/zbpb-6qxb.

[112] H. Katori. "Longitudinal Ramsey spectroscopy of atoms for continuous operation of optical clocks". In: *Appl. Phys. Express* 14 (7 July 2021), p. 072006. ISSN: 1882-0786. DOI: 10.35848/1882-0786/AC0E16. URL: https://iopscience.iop.org/article/10.35848/1882-0786/ac0e16.

[113] R. Takeuchi et al. "Continuous outcoupling of ultracold strontium atoms combining three different traps". In: *Appl. Phys. Express* 16 (4 Apr. 2023), p. 042003. ISSN: 18820786. DOI: 10.35848/1882-0786/accb3c.

[114] S. Okaba et al. "Continuous generation of an ultracold atomic beam using crossed moving optical lattices". In: *Phys. Rev. Appl.* 21 (3 Mar. 2024), p. 034006. ISSN: 23317019. DOI: 10.1103/PhysRevApplied.21.034006.